

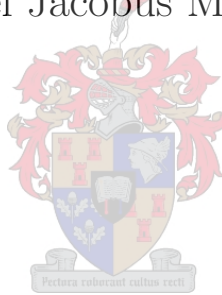


UNIVERSITEIT•STELLENBOSCH•UNIVERSITY
jou kennisvennoot • your knowledge partner

The Quadrifilar Helix Antenna and its Application to Wide Angle Phase-Steered Arrays

by

Sarel Jacobus Marais



*Thesis presented in partial fulfilment of the degree
Master of Science in Engineering (Electronic Engineering
with Computer Science) in the Department of Electrical and
Electronic Engineering at the University of Stellenbosch*

Supervisor: Prof. K.D. Palmer

March 2007

Declaration

I, the undersigned, hereby declare that the work contained in this thesis is my own original work and that I have not previously in its entirety or in part submitted it at any university for a degree.

Signature:

S.J. Marais

Date:

Abstract

The quadrifilar helix antenna has frequently been employed to provide the wide angle, circularly polarized radiation pattern which is preferable for mobile satellite communications. A detailed study of this antenna and its varieties is presented. When used as an element in wide angle scanning arrays for aeronautical satellite tracking applications, the additional requirement of a low profile with light weight applies. This further complicates the realization of good circular polarization close to the horizon.

A top disk is incorporated into various antenna structures in an effort to improve the radiation performance when used within a closely spaced array while reducing the height of the radiating element. The array performance of these elements are investigated which hints at a supported traveling mode aiding the ability to accomplish the wide angle beam steering. Subsequent study of leaky-wave antennas initiated the study and implementation of leaky-wave structures in phased arrays of quadrifilar helix elements.

Samevatting

Die vierledige heliksantenna word dikwels gebruik vir toepassings wat 'n wye, sirkulêr gepolariseerde stralingspatroon benodig. 'n Verskeidenheid van hierdie antennes is noukeurig bestudeer en hul toepaslikheid vir mobiele sattelietkommunikasie ondersoek. Wanneer hierdie antennes in fase gestuurde skikkings gebruik word, word dit ook vereis dat die eenhede liggewig is met 'n lae profiel. Dit bemoedlik die verkryging van goeie sirkulêre polarisasie naby die horison aansienlik.

In 'n poging om die wyehoek straling met kort antennes te verbeter, is 'n oorhoofse skyf tot verskillende heliksstrukture toegevoeg. In nou gespasiëerde skikkings maak hierdie skyf 'n positiewe bydrae to wyehoekstralingeienskappe. Die invloed van lekmodusse wat binne die struktuur voortplant is ondersoek en gebruik in skikkings waarvan die bundel naby aan die horison gestuur word.

Acknowledgements

To Professor Keith Palmer for his expert guidance and tireless patience.

To Wessel Croukamp and his team for excellent workmanship.

To my family and friends for their loving support - in particular Hybré Marais and Aletsia Muller.

Contents

Declaration	i
Abstract	ii
Samevatting	iii
Acknowledgements	iv
Contents	v
List of Figures	ix
List of Tables	xv
List of Abbreviations	xvi
1 Introduction	1
2 The Quadrifilar Helix Antenna	3
2.1 Introduction	3
2.2 Quadrature Fed QHA	4
2.2.1 Physical Configuration	4
2.2.2 Resonant Half-Wavelength QHA	5
2.2.3 Resonant Three Quarter-Wavelength QHA	10
2.2.4 Resonant Quarter-Wavelength QHA	13
2.3 Self-Phased QHA	15
2.3.1 Physical Configuration	15
2.3.2 Current Distribution and Input Impedance	15
2.3.3 Radiation Pattern	17
2.4 Other QHA Configurations	18
2.4.1 Multi-turn QHAs with Shaped-Conical Radiation Patterns	18
2.4.2 Printed Quadrifilar Helix Antenna	20

<i>CONTENTS</i>	vi
2.4.3 Tapered QHAs	21
2.5 Summary	24
3 The QHA as Array Element	25
3.1 Introduction	25
3.2 Half-Wavelength QHA	26
3.2.1 Physical Configuration	26
3.2.2 Impedance	27
3.2.3 Radiation	28
3.3 Quarter-Wavelength QHA	30
3.3.1 Physical Configuration	30
3.3.2 Input Impedance and Feed Point Adjustment	31
3.3.3 Radiation	34
3.4 Chosen Element for Prototype	34
3.5 Feed Network	35
3.5.1 Obtaining the Active Antenna Input Impedance from Ex- ported S-Parameters.	35
3.5.2 Impedance Bandwidth Improvement	37
3.5.3 Design of the Feed Network	37
3.5.4 Verification with FEKO	41
3.6 Measured Results	43
3.7 Summary	45
4 Array Performance of the QHA Elements	46
4.1 Introduction	46
4.2 Introducing Array Theory and Stating the Necessary Conditions for Low Elevation Angle Scanning	47
4.2.1 Classic Array Pattern Multiplication without Mutual Cou- pling	47
4.2.2 Pattern Multiplication Examples	48
4.2.3 Practical Arrays with Mutual Coupling	51
4.3 Description of Array Geometries Used	54
4.3.1 Linear Array	54
4.3.2 Rectangular Array	54
4.3.3 Hexagonal Array	55
4.4 Combining the Antenna and Feed Network	56
4.5 Comparing Array Characteristics of Different QHA Elements	59
4.5.1 Linear Array	60

<i>CONTENTS</i>	vii
4.5.2 Rectangular Array	62
4.5.3 Hexagonal Array	65
4.6 Summary	70
5 Leaky Wave Antennas	72
5.1 Introduction	72
5.2 Properties and Characteristics	72
5.2.1 The Non-Modal Nature of Leaky Waves.	74
5.2.2 Leaky Waves vs. Surface Waves	76
5.2.3 Radiation Characteristics	77
5.3 Determination of the Complex Propagation Constant	78
5.3.1 Transverse Resonance Procedure	78
5.3.2 FDTD	79
5.4 Single QHA Element Exciting a Leaky-Wave Structure	80
5.4.1 Physical Construction	80
5.4.2 Design Simulations	81
5.4.3 Measured Results	85
6 Further Analysis of Steered Leaky Wave Arrays	89
6.1 Introduction	89
6.2 Dimensional Parameters	90
6.3 Beam Steering	91
6.4 Finite Ground Plane	91
6.5 Summary	94
7 Conclusions and Recommended Future Work	95
7.1 Conclusions	95
7.2 Future Work	97
Bibliography	99
A Parameter Study Automating Software	A-1
A.1 The GUI	A-1
A.1.1 Simulation Setup	A-1
A.1.2 Data Management	A-2
A.1.3 Result Visualization	A-3
B Array Simulation Project Software	B-1
B.1 The Graphical User Interface	B-1

CONTENTS

viii

B.1.1	Project Options	B-2
B.1.2	Geometry	B-3
B.1.3	Excitation	B-3
B.1.4	Far-field Solutions and Beam Steering	B-4
B.1.5	Output Files and Data Storage	B-4
B.1.6	Other Options and Information	B-4
B.2	Data Management and Control Flow	B-5
C	Hexagonal Array Coordinates	C-1

List of Figures

2.1	Physical parameters and geometry of the fractional turn $\lambda/2$ QHA.	4
2.2	Illustrating the position of the current null at frequencies (a) below, (b) at and (c) above resonance.	5
2.3	Normalized enclosed volume vs. axial length/radius of a half-wavelength QHA with different number of turns.	6
2.4	Real and imaginary components of the simulated input impedance of $\lambda/2$ QHAs with different number of turns and varying axial length/radius ratio (R).	8
2.5	Elevation plane far-field radiation properties of $\lambda/2$ QHAs with different number of turns and varying axial length/radius ratio (R).	9
2.6	Real and imaginary components of the simulated input impedance of $3\lambda/4$ QHAs with different number of turns and varying axial length/radius ratio (R).	11
2.7	Elevation plane far-field radiation properties of $3\lambda/4$ QHAs with different number of turns and varying axial length/radius ratio (R).	12
2.8	Real and imaginary components of the simulated input impedance of $\lambda/4$ QHAs with different number of turns and varying axial length/radius ratio (R).	13
2.9	Elevation plane far-field radiation properties of $\lambda/4$ QHAs with different number of turns and varying axial length/radius ratio (R).	14
2.10	A FEKO simulation model of a self-phased QHA with detail of the parallel feed.	15
2.11	Current distribution along the helical elements at the center frequency (1.6 GHz) and at frequencies above and below the center frequency.	16
2.12	Simulated input impedances of the individually fed bifilar helices of the self-phased QHA.	16
2.13	(a) Simulated input impedance of a parallel fed self-phased QHA. (b) Magnitude of the reflection coefficient (referenced to a 50Ω system).	17

2.14	Illustrating the asymmetry in the radiation pattern of the self-phased QHA at frequencies away from resonance.	17
2.15	Showing the far-field gain components at frequencies (a) below resonance, (b) at resonance and (c) above resonance. Orthogonal elevation plane cuts at $\phi = 0^\circ$ and $\phi = 90^\circ$ are plotted to illustrate the asymmetrical pattern. In (d) the axial ratio at all three frequencies are plotted ($\phi = 0^\circ$).	18
2.16	(a) Illustrating the varying distance between the satellite and the ground station. (b) A typical shaped-conical radiation pattern from a multi-turn QHA.	19
2.17	(a) Simulation model of the ZA-002 ground station antenna. (b) Co- and cross-polarized components of the far-field gain at 403 MHz.	20
2.18	(a) Input impedance of a single helical element of the multi-turn ground station antenna. (b) Magnitude of the input reflection coefficient referenced to a 50Ω system.	20
2.19	Example of a printed quadrifilar helix FEKO model.	21
2.20	(a) Exponentially tapered QHA. (b) Top view. (c) Side View.	22
2.21	(a) Co- and cross-polarization components of the far-field radiation pattern. (b) Axial ratio in the elevation plane. $\phi = 0^\circ$	23
2.22	(a) Input impedance of the exponentially tapered QHA. (b) Magnitude of the input reflection coefficient referenced to a 30Ω system.	23
3.1	(a) Simulation model of the $\lambda/2$ QHA with top patch connected to the helical elements. (b) Side-on view of the $\lambda/2$ QHA showing the position of the shorting disc and other dimensional features.	26
3.2	(a) Real and imaginary components of the simulated input impedance of the $\lambda/2$ QHA with shorting disc. (b) Smith chart plot of the input impedance (normalized to 50Ω).	28
3.3	Example of a simulation model for the $\lambda/2$ QHA without the shorting disc.	28
3.4	Elevation plane far-field radiation properties of a $\lambda/2$ QHA with an infinite ground plane and and no shorting-disc for a varying axial length/radius ratio (R). $n = 0.425$	29
3.5	Far-field radiation characteristics of the $\lambda/2$ QHA with top shorting disk.	29
3.6	(a) Simulation model of the $\lambda/4$ QHA with parasitic top patch floating above the helical elements. (b) Side on view of the $\lambda/4$ QHA showing the position of the disc above the helices.	30

<i>LIST OF FIGURES</i>	xi	
3.7	Current distribution on the helical conductors.	31
3.8	(a) Illustrating the currents on the coaxial cable. (b) FEKO simulation model of the helical elements with expanded feed point detail. (The ground plane and top patch are not shown).	32
3.9	(a) Real and Imaginary components and (b) a Smith chart plot of the input impedance at the simulated feed point and at the ground plane of the $\lambda/4$ QHA. The Smith chart is normalized to 50Ω	33
3.10	Far-field radiation characteristics of the $\lambda/4$ QHA with parasitic disc.	34
3.11	4-port representation of the QHA for which the feed network is designed.	35
3.12	Illustrating the improvement in impedance bandwidth when to quadrature phased elements are fed in parallel.	37
3.13	(a) Simplified diagram of the hybrid feed network. Normalized schematic circuits of the (b) 90° and (c) 180° hybrid networks.	39
3.14	Layout of the microstrip feed network.	40
3.15	(a) Power delivered at the output ports of the feed network with a 0 dBm signal applied at the input. (b) Relative phase of the signals at the output ports.	40
3.16	(a) Reflection coefficient at the input of the feed network when the FEKO S-parameter model of the antenna is connected to the output ports. (b) Smith chart plot of the reflection coefficient at the input port.	41
3.17	(a) FEKO simulation model with the QHA connected to the microstrip feed network imported from Microwave Office. The infinite dielectric layer and ground plane are omitted. (b) Co-polarized gain component illustrating the directive radiation pattern of the single element $\lambda/2$ QHA in isolation.	41
3.18	(a) Magnitude and (b) Smith chart plot of the input impedance reflection coefficient of the feed network with antenna connected (FEKO simulation).	42
3.19	(a) Magnitude and (b) phase of the current in the segments that connect the microstrip tracks to the helices.	43
3.20	Simulated (a) gain and (b) axial ratio of the $\lambda/2$ QHA prototype fed by the microstrip feed network. $\phi = 0^\circ$	43
3.21	(a) Microstrip feed network. (b) $\lambda/2$ QHA with top shorting disc prototype connected to the feed network.	44

3.22	(a) Magnitude and (b) Smith chart plot of the input impedance reflection coefficient of the constructed antenna with microstrip feed network.	44
3.23	Measured and simulated (a) gain and (b) axial ratio of the $\lambda/2$ QHA prototype fed by the microstrip feed network ($f = 1.6\text{ GHz}$).	45
4.1	Array of N arbitrary radiating elements.	48
4.2	Theoretically calculated elevation plane array radiation pattern for a linear array of varying number of elements. The disk-shortened $\lambda/2$ QHA of Section 3.2.3 is used as radiating element.	50
4.3	Equivalent circuit of radiating element number m with its feed within an N element array ([17]).	51
4.4	Linear array arrangement.	54
4.5	Rectangular array arrangement.	55
4.6	Hexagonal array arrangement.	56
4.7	A diagram representing the parallel connection between the 4-port antenna and 5-port feed network.	57
4.8	RHC polarized component of the far-field radiation pattern with only the center element fed.	60
4.9	Comparison of the middle element active element pattern of a 25 element linear array comprised of different radiating elements. $\phi = 0^\circ$	60
4.10	Coupling coefficients between the elements of the linear arrays.	61
4.11	(a) Co-polarized component of the far-field radiation pattern, and (b) Axial ratio on the linear arrays at the specified angles to which beam steering is attempted.	62
4.12	Resulting radiation pattern of the linear arrays with the element phasing calculated to have an array factor maximum at θ_0 and ϕ_0 . The values of θ_0 are indicated in the figures, and $\phi_0 = 0^\circ$	62
4.13	RHC polarized component of the far-field radiation pattern of the rectangular arrays with only the center element fed.	63
4.14	Comparison of the middle element active element pattern of a 49 element rectangular arrays comprised of different QHA elements. $\phi = 0^\circ$	63
4.15	Coupling coefficients between the diagonal elements of the rectangular arrays.	64
4.16	(a) Co-polarized component of the far-field radiation pattern, and (b) Axial ratio of the rectangular arrays at the specified angles to which beam steering is attempted.	64

4.17	Resulting radiation pattern of the rectangular arrays with the element phasing calculated to have an array factor maximum at θ_0 and ϕ_0 . The values of θ_0 are indicated in the figures, and $\phi_0 = 0^\circ$	65
4.18	Comparison of the middle element active element pattern of 37, 61 and 91 element hexagonal arrays comprised of different QHA elements. $\phi = 0^\circ$	66
4.19	RHC polarized component of the far-field radiation pattern of the various hexagonal arrays with only the center element fed.	67
4.20	Average of the coupling coefficient magnitude between the center element and concentric layers of elements of 91 element hexagonal arrays.	68
4.21	(a) Co-polarized component of the far-field radiation pattern, and (b) Axial ratio of the 61 element hexagonal at the specified angles to which beam steering is attempted.	69
4.22	Resulting radiation pattern of the 61 element hexagonal arrays with the element phasing calculated to have an array factor maximum at θ_0 and ϕ_0 . The values of θ_0 are indicated in the figures, and $\phi_0 = 0^\circ$	69
4.23	(a) Co-polarized component of the far-field radiation pattern, and (b) Axial ratio of the 91 element hexagonal at the specified angles to which beam steering is attempted.	70
4.24	Resulting radiation pattern of the 91 element hexagonal arrays with the element phasing calculated to have an array factor maximum at θ_0 and ϕ_0 . The values of θ_0 are indicated in the figures, and $\phi_0 = 0^\circ$	70
5.1	A general periodic LWA consisting of a PRS mounted on a grounded dielectric substrate.	73
5.2	Radiation from a semi-infinite leaky waveguide [25].	75
5.3	(a) Leaky wave antenna consisting of a PRS mounted on a grounded dielectric slab with a hertzian dipole excitation. (b) Transverse equivalent network representation of the structure [29].	79
5.4	CAD construction model of the leaky-wave antenna.	81
5.5	Selected simulation results with circular patch elements used. Parameters dimensions given are in <i>mm</i> , and $\phi = 0$	82
5.6	Selected simulation results with hexagonal patch elements used. Parameters dimensions given are in <i>mm</i> , and $\phi = 0$	83
5.7	Co-polarized gain component of the final simulation model illustrating the characteristic conical radiation pattern from a two-dimensional leaky-wave antenna.	84

5.8	Simulated instantaneous E-field just above the patches at (a) 0° , (b) 90° , (c) 180° and (d) 270° . Linear Scale [$0 V/m \dots 50 V/m$].	84
5.9	Simulated and measured (a) gain and (b) axial ratio in the elevation plane with $\phi = 0^\circ$	87
5.10	(a) Assembled LWA. (b) Hexagonal patch PRS. (c) $\lambda/4$ QHA excitation element.	88
6.1	Co- and cross-polarized gain components of the steered beam with an infinite ground plane. The values for which the phasing was calculated are indicated.	91
6.2	Co- and cross-polarized gain components of the steered beam with a finite ground plane. The values for which the phasing was calculated are indicated.	92
6.3	(a) Unit element for the creation of the finite ground plane array. (b) Electric field magnitude just above the PRS with the array scanned to $\theta = 85^\circ$. (c) Hemispherical plane E-field magnitude with the array scanned to $\theta = 85^\circ$. (d) RHCP gain component with the beam scanned to $\theta = 85^\circ$	93
A.1	(a) Screenshot of the graphical user interface. (b) Example of an automatically created plot of the results of a parametrical study. . .	A-2
B.1	Screenshot of the CAP user interface.	B-2

List of Tables

1.1	Basic requirements for aeronautical Inmarsat Antennas.	2
2.1	Geometrical parameters of the ground station antenna for the ZA-002 satellite programme.	19
3.1	Geometrical parameters of the disc-shortened $\lambda/2$ QHA considered for prototyping.	27
3.2	Geometrical parameters of the $\lambda/4$ QHA with parasitic patch considered for prototyping.	31
5.1	Summarizing the differences between Leaky Waves and Surface Waves.	76
5.2	Chosen values of the parameters for the construction of the LWA prototype.	83
6.1	Physical parameters array with preferred performance	90

List of Abbreviations

AR	Axial Ratio
CP	Circular Polarization
dB	Decibel
FDTD	Finite-Difference Time-Domain
LHCP	Left-hand Circular Polarization
LWA	Leaky Wave Antenna
LWS	Leaky Wave Structure
PQHA	Printed Quadrifilar Helix Antenna
PRS	Partially Reflective Surface
QHA	Quadrifilar Helix Antenna
RHCP	Right-hand Circular Polarization
RX	Receive
TX	Transmit

Chapter 1

Introduction

The ever increasing demand for mobile connectivity necessitates the continuous development and improvement of satellite communications systems. Inmarsat is an international telecommunications company founded in 1979, originally as an intergovernmental organization. It operates a fleet of geosynchronous satellites which provides telephony and data services to users world-wide. These include a range of governments, aid agencies, media outlets and businesses needing to communicate in remote regions or in regions where there is no reliable terrestrial network. The Inmarsat-Aero network provides voice, fax and data services for aircraft. There are three levels of terminals namely Aero-L (Low Gain Antenna) primarily for packet data, Aero-I (Intermediate Gain Antenna) for low quality voice/data up to 2400 *bit/s*, and Aero-H (High Gain Antenna) for medium quality voice/data up to 9600 *bit/s*.

The basic requirements of antennas for high gain aeronautical Inmarsat applications are summarized in Table 1.1. Additional requirements include restrictions on intermodulation products and a range of operating temperatures. It is also necessary for the antenna gain to drop off rapidly below the horizon to reduce multipath interference. Achieving these specifications - especially the wide angle, circularly polarized beam - with a light weight, low profile antennas that will be suitable for use on aircraft is a daunting task. The superior low elevation radiation performance and compact size of a recently developed high gain aeronautical Inmarsat antenna [1] set a new standard for antenna designers in this field and there is a lot of interest in developing antennas with similar or improved performance and reduced size.

As a potential candidate for the use as an element within wide angle scanning arrays, the quadrifilar helix antenna (QHA) is investigated. Owing to its wide angle radiation, good circular polarization and compact size, the QHA has been

Table 1.1: Basic requirements for aeronautical Inmarsat Antennas.

Receive Frequency	1530.0 – 1559.0 <i>MHz</i>
Transmit Frequency	1626.5 – 1660.0 <i>MHz</i>
Gain	12 <i>dB_i</i> (RHCP)
Side Lobe Levels	< 13 <i>dB</i> at 45° from pointing direction
Axial Ratio	< 6 <i>dB</i>
Coverage	Hemispherical coverage above 5° from the horizon

used extensively in mobile satellite communication systems. Different QHA variations are compared and their viability for use in array applications considered. A low profile is of particular importance for aeronautical applications and this requirement is a key consideration throughout the study.

During the development of the above mentioned product [1], it was found experimentally that the inclusion of a parasitic disk above a cavity-backed crossed slot radiating element within a closely spaced array improved the ability to scan to low elevation angles to a great extent. This phenomenon is investigated further by incorporating a similar structure to various QHA elements and investigating the effect on the isolated and arrayed radiation characteristics. Emphasis is placed on radiation performance and the mechanism of radiation - in particular the ability to scan to low elevation angles with good circular polarization. The detailed design of an array antenna which conforms to the requirements of Table 1.1 and is impedance matched at all scan angles over the entire frequency band is beyond the scope of this study.

Conforming to the Inmarsat specifications, all of the investigations is done at the specified L-band frequencies. Throughout the text (if not mentioned otherwise), the frequency used in calculations, simulations and measurements is 1.6 *GHz*.

Extensive use is made of software simulation tools, in particular FEKO. This is a full-wave, method of moments (MoM) based computer code for the analysis of electromagnetic problems [2]. Other software which was developed specifically for the analysis and design of the quadrifilar helix antennas and large phased arrays is presented in Appendices A and B.

Chapter 2

The Quadrifilar Helix Antenna

2.1 Introduction

Circularly polarized (CP) antennas find wide application in mobile satellite communications and direct broadcasting satellite systems due to their insensitivity to ionospheric polarization rotation. In mobile satellite communications systems, an omnidirectional beam of a CP antenna is preferable because no satellite tracking in the azimuthal direction is needed.

The concept of multi-element, fractional turn helix antennas was first introduced by Kilgus in 1968 [3]. It was shown that with the proper choice of geometric parameters, a resonant half-turn, anti-phase fed, bifilar helix radiates a sine-shaped, circularly polarized beam. Two such bifilar helices, concentric with orthogonal radials, radiates a circularly polarized, cardioid-shaped (heart-shaped) pattern when fed in phase quadrature. Comparison with other antennas indicates that this quadrifilar helix antenna (QHA) offers excellent performance for narrow band applications requiring a broad beam width, cardioid-shaped, circularly polarized radiation pattern and a compact configuration. Another important consideration – especially in spacecraft applications – is that the radiation characteristics of the QHA are relatively insensitive to the presence of metal structures behind the antenna [4].

The initial sections of this chapter discuss the physical configuration and principle of operation, and present parametrical studies of some of the most common variations of the QHA. The antennas are grouped into two main categories according to the method of excitation. These include the quadrature-fed QHA where each helical element is fed individually with the correct phasing and amplitude, and the self-phased QHA where two bifilar loops are fed in parallel and the required phasing is achieved by adjusting the resonant lengths of the helices.

Section 2.4.1 focuses on multi-turn QHAs which produce shaped-conical radiation patterns and an example of a design for a satellite communication ground station terminal is shown. The printed quadrifilar helix antenna is mentioned briefly, and an example of a QHA design with an exponentially tapered profile is presented.

Throughout this parametrical study of the QHA elements, extensive use is made of Matlab software developed specifically for this task. A graphical user interface allows the user to specify the one or more parameters of which the values will be swept in the ensuing FEKO simulations. The results of these runs are stored and made available for interactive comparison and visualization afterward. More detail of this software is given in Appendix A.

2.2 Quadrature Fed QHA

2.2.1 Physical Configuration

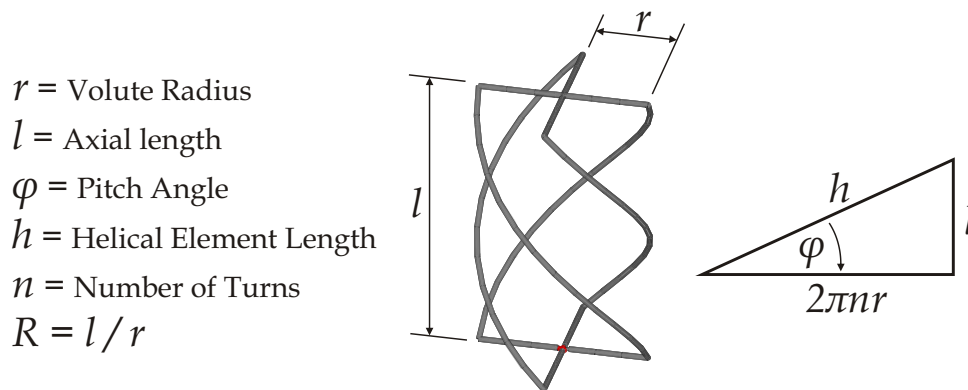


Figure 2.1: Physical parameters and geometry of the fractional turn $\lambda/2$ QHA.

The traditional quadrifilar helix antenna shown in Figure 2.1 consists of four helical conductors (two bifilar loops) that are excited in phase quadrature at the feed point located in the center of the top radials – thus operating in the backfire mode. By reversing the phasing of the excitation, the antenna can also be fed at the bottom while still covering the top hemisphere with a circularly polarized beam. The radials at the opposite end of the antenna are usually open-circuited for radiating elements with a resonant length which is an odd multiple of a quarter-wavelength, and short-circuited for even multiples of a quarter-wavelength. This is done to produce a current maximum at the feed and so ensure that the input impedance is small enough to obtain a good match between the antenna and the feed network. As discussed in Section 3.3.2 the input impedance

can be adjusted by moving the feed up the helical element to a point of higher or lower current magnitude.

The beam shape, polarization purity and input impedance of the antenna are determined by the diameter and axial length of the helix, the number of turns, diameter of radiating elements and other properties [5]. Optimum performance occurs at resonance where the two bifilar helices are excited in phase quadrature with equal amplitude signals, and the current distribution in the helical loops is symmetrical [6].

2.2.2 Resonant Half-Wavelength QHA

Current Distribution

At resonance, a driven half-wavelength bifilar loop has a current maximum at the center of the top and bottom radial sections and a current null at the center of the helical section. At frequencies below resonance, the current null is shifted off center in the direction of the excitation location. Conversely, the null moves away from the feed point at frequencies above resonance. This is illustrated in Figure 2.2. It is also observed that the overall current magnitude is greater at resonance.

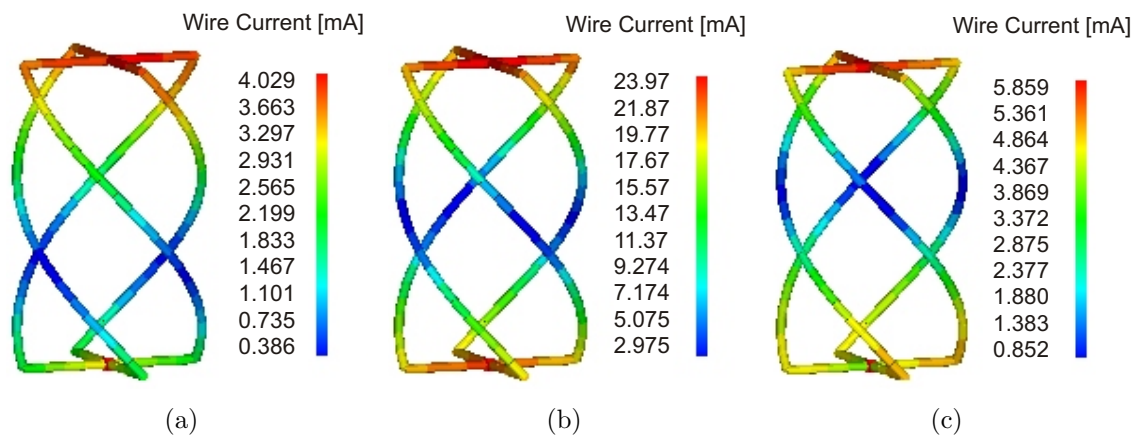


Figure 2.2: Illustrating the position of the current null at frequencies (a) below, (b) at and (c) above resonance.

Because a wide band feed network (such as a combination of 90° and 180° hybrids) is normally used to excite the QHA, the performance degradation off resonance can largely be attributed to the asymmetric current distribution in the four helical conductors.

Input Impedance

Kilgus suggested that the resonant input resistance as well as the impedance bandwidth increase in proportion to the cylindrical volume enclosed by the volute [7]. The total length of one bifilar loop of the $\lambda/2$ QHA of Figure 2.1 is given by

$$L_{tot} = 2 \left(\sqrt{(2\pi nr)^2 + l^2} + 2r \right) \quad (2.1)$$

and the enclosed volume is

$$V(r, l) = \pi r^2 l \quad (2.2)$$

Solving (2.1) for l and substituting into (2.2) gives

$$V(r) = \pi r^2 \sqrt{\left(\frac{L_{tot} - 4r}{2} \right)^2 - (2\pi nr)^2} \quad (2.3)$$

For a constant resonant length (L_{tot}), the volume enclosed by a half-wavelength volute is plotted against the ratio of the axial length to the volute radius for a different number of turns – see Figure(2.3).

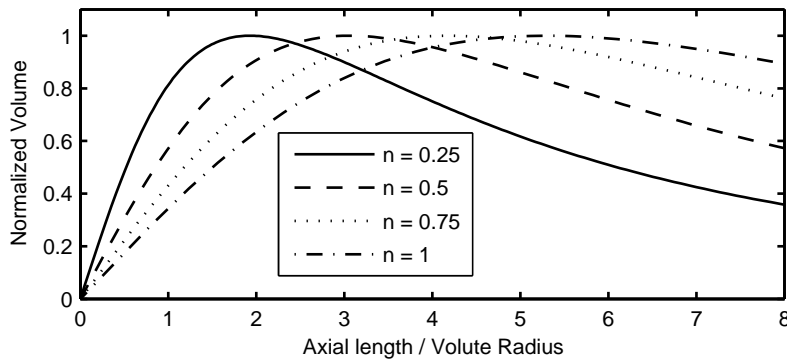


Figure 2.3: Normalized enclosed volume vs. axial length/radius of a half-wavelength QHA with different number of turns.

Figure 2.4 shows the simulated input impedance of $\lambda/2$ QHAs with varying axial length/radius ratio (R) and a different number of turns (n) while the resonant length of the helices is kept constant. This confirms the increasing resonant input resistance proportional to the enclosed volume. The impedance bandwidth, which largely depends on the gradient of the real and imaginary impedance curves, is shown to be less sensitive to variations in volute radius. In a practical antenna system both the impedance and radiation bandwidth are strongly dependent on the feed network. This will be illustrated in 3.5 where the design of a feed net-

work for a prototype QHA is outlined. It is also observed that the input resistance increases for a smaller number of turns (larger pitch angles).

For a given resonant length, a reduced number of turns requires an increased axial length, and for applications requiring a low profile radiating element, a trade-off has to be made between physical size limitations and the input resistance necessary to match the antenna to the feed network.

Radiation Pattern

The quadrifilar helix is used for applications that require a cardioid-shaped, circularly polarized beam with a high front to back ratio and low cross-polarization. For mobile satellite communication applications it is desirable to produce a circularly polarized beam that covers the entire upper hemisphere. Figure 2.5 shows the FEKO simulation results of QHAs with varying radii (r) and different number of turns for a constant resonant length. The co- and cross-polarization components of the radiation pattern in the elevation plane, as well as the axial ratio, are plotted at the resonant frequency (1.6 GHz).

A larger number of turns results in a smaller cross-polarization component and better axial ratio over a wider beam angle. Also, for a given number of turns and resonant length, longer volutes with smaller radii produce wider beams. These longer QHAs have a small resonant input resistance and can be impractical when a low profile is essential.

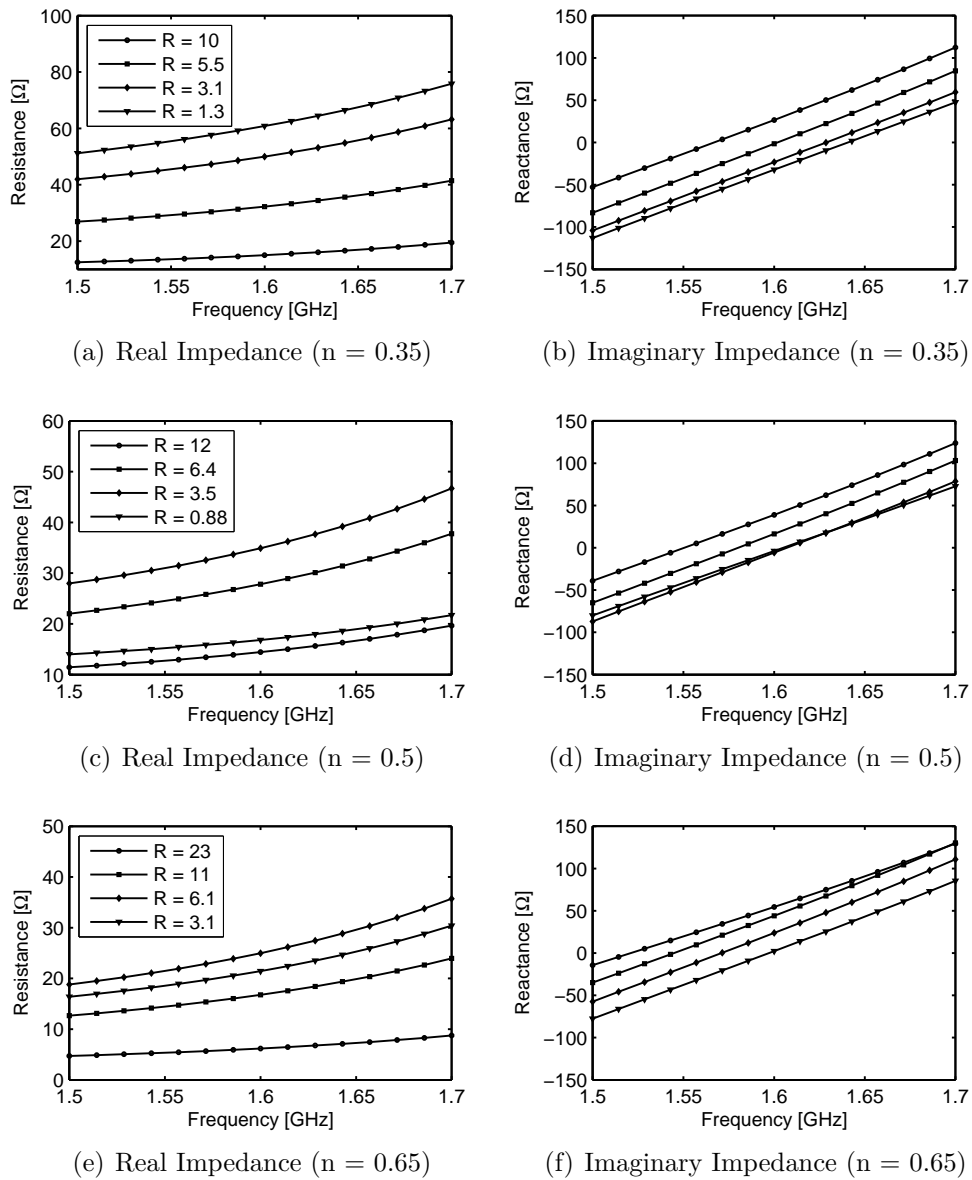


Figure 2.4: Real and imaginary components of the simulated input impedance of $\lambda/2$ QHAs with different number of turns and varying axial length/radius ratio (R).

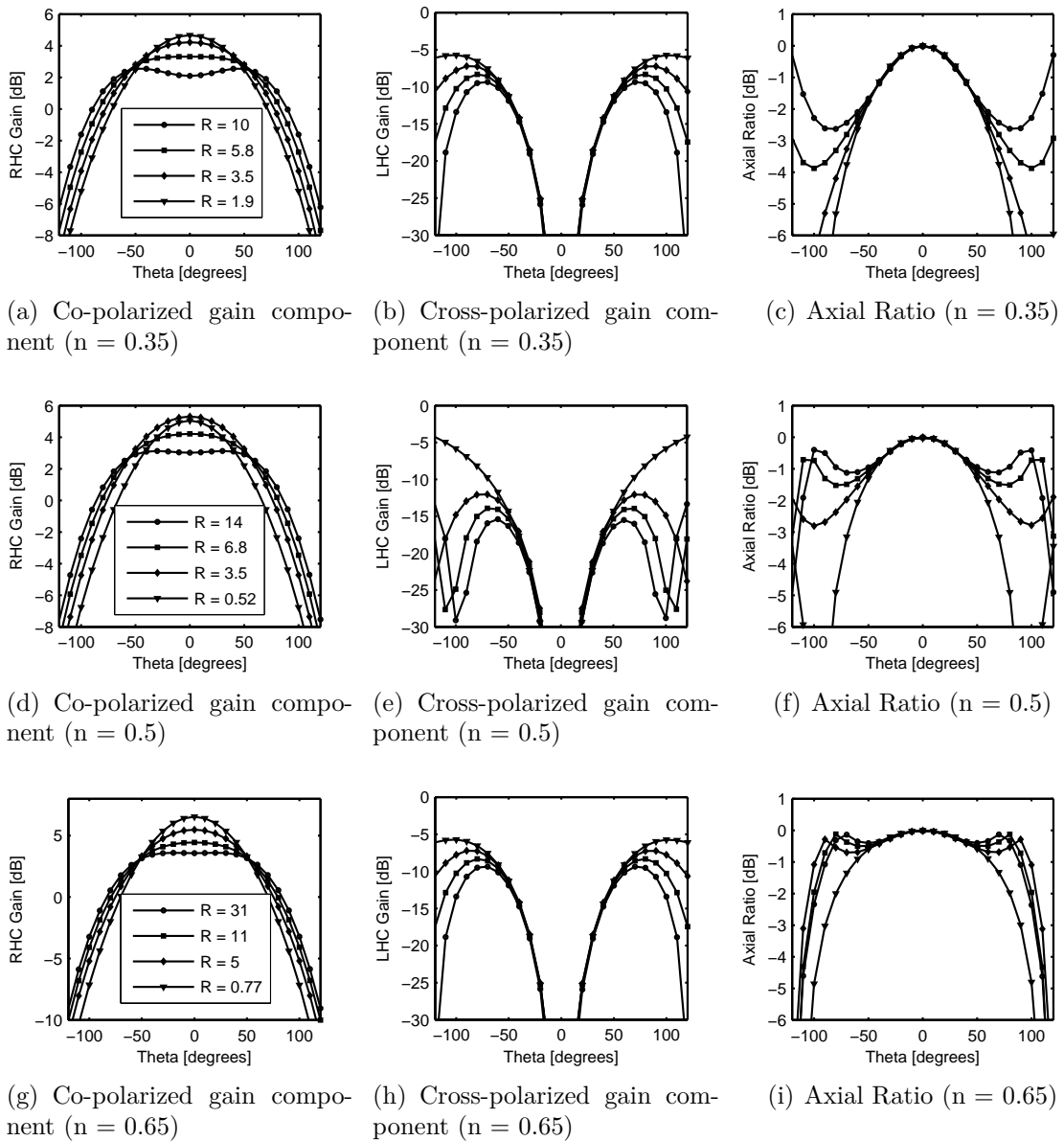


Figure 2.5: Elevation plane far-field radiation properties of $\lambda/2$ QHAs with different number of turns and varying axial length/radius ratio (R).

2.2.3 Resonant Three Quarter-Wavelength QHA

Current Distribution

To ensure a current maximum at the feed point, the opposite ends of the helical elements of a three quarter-wavelength QHA are open circuited (creating a minimum at that end). Without the need for a short circuit at the ends, the construction of the antenna is simplified.

Input Impedance

The input impedance for $3\lambda/4$ QHAs with 0.75, 1 and 1.25 turns, which were simulated in FEKO, are shown in Figure 2.6. The total length of the radiating elements is kept constant during the simulations. From these graphs it can be seen that neither the bandwidth nor the resonant input resistance is necessarily dependent on the enclosed volume of the volute. Similar to the $\lambda/2$ QHA, the real part of the input impedance for the volutes with 1 and 1.25 turns increases with the pitch angle (increasing axial length/radius ratio). For volutes with less than a full turn, the resistance decreases for larger axial length/radius ratios. Also, the gradient of the impedance curves is slightly smaller for volutes with larger radii (smaller axial length/radius ratio), which implies a wider bandwidth.

Radiation Pattern

The $3\lambda/4$ QHA has the same radiation characteristics, and displays the same trends in radiation pattern with variations in geometrical parameters as the half-wavelength QHA. The cross-polarization component decreases with increasing number of turns while a broader beam is achieved for longer volutes with smaller radii. These variations in beam width are more pronounced for a larger number of turns, as the axial length varies more for different radii if the total resonant element length is kept constant. Once again, these longer elements which produce a wider beam can become impractical if a low profile is required.

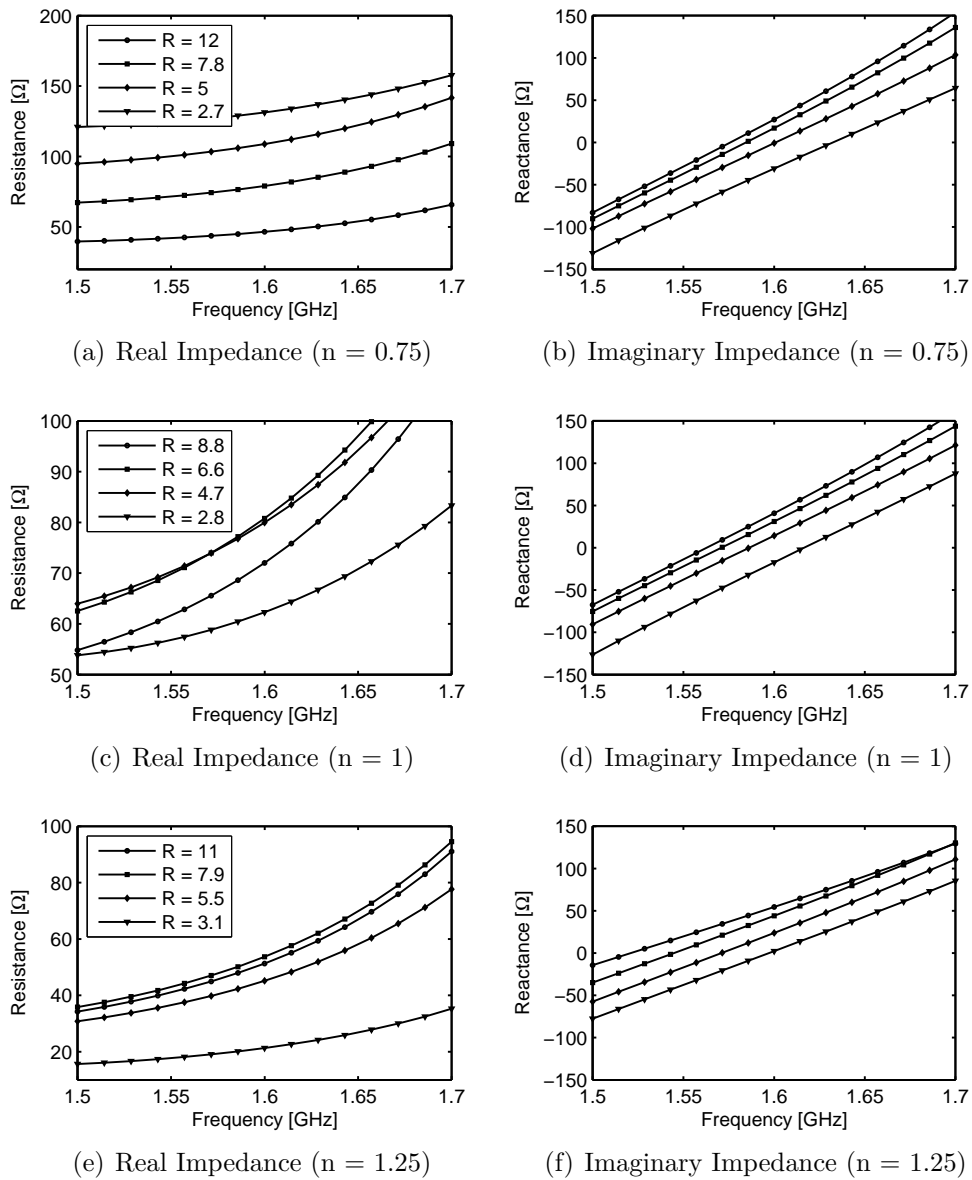
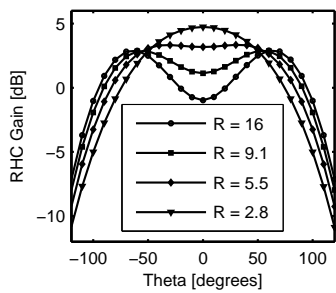
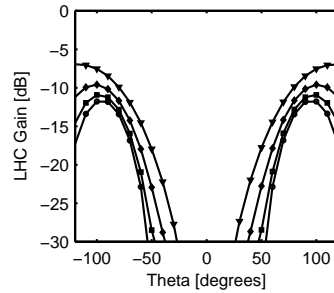


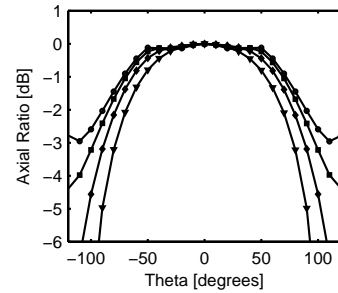
Figure 2.6: Real and imaginary components of the simulated input impedance of $3\lambda/4$ QHAs with different number of turns and varying axial length/radius ratio (R).



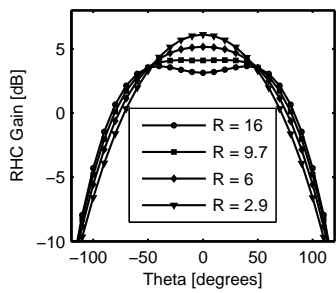
(a) Co-polarized gain component ($n = 0.75$)



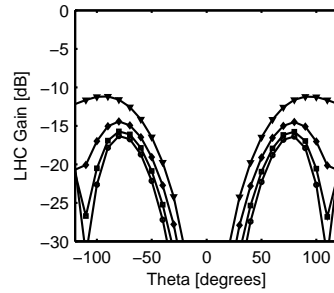
(b) Cross-polarized gain component ($n = 0.75$)



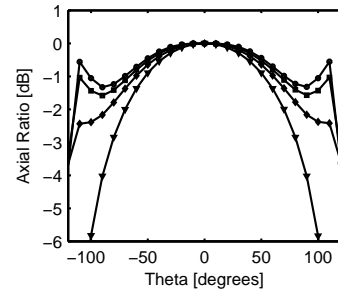
(c) Axial Ratio ($n = 0.75$)



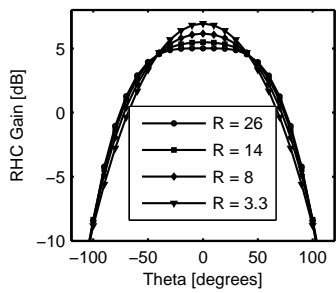
(d) Co-polarized gain component ($n = 1$)



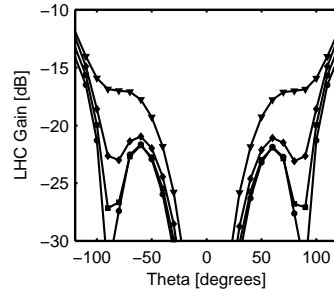
(e) Cross-polarized gain component ($n = 1$)



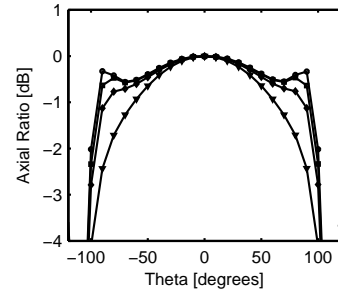
(f) Axial Ratio ($n = 1$)



(g) Co-polarized gain component ($n = 1.25$)



(h) Cross-polarized gain component ($n = 1.25$)



(i) Axial Ratio ($n = 1.25$)

Figure 2.7: Elevation plane far-field radiation properties of $3\lambda/4$ QHAs with different number of turns and varying axial length/radius ratio (R).

2.2.4 Resonant Quarter-Wavelength QHA

Current Distribution and Input Impedance

The $\lambda/4$ volute is also open-circuited at the end to ensure a current maximum at the feed point. The resonant input resistance when fed right at the bottom (end opposite the open-circuited end) is very small though – no more than a couple of ohms. This makes it difficult to match the antenna to the feed network. By feeding the antenna at a point of lower current (i.e. higher up the helical element), the input impedance can be adjusted to the desired level. This is discussed further in Section 3.3.2. The input resistance decreases with the pitch angle, and becomes extremely small for more than half a turn. Figure 2.8 summarizes the impedance characteristics of the simulated $\frac{1}{4}$ and $\frac{1}{2}$ turn QHAs when fed at the end.

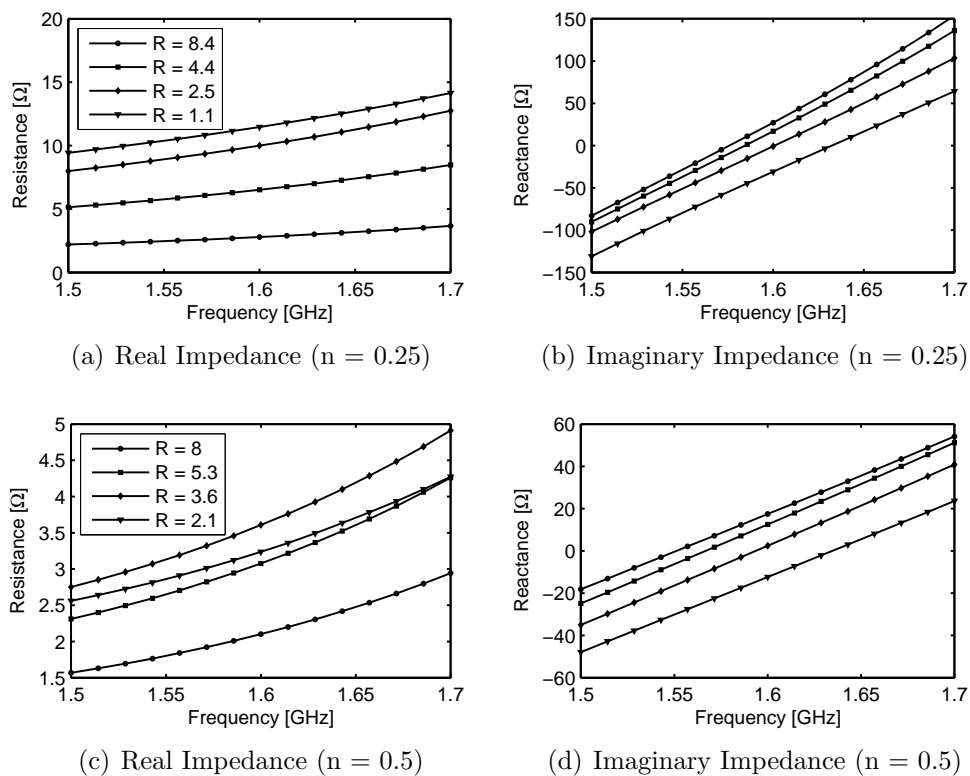


Figure 2.8: Real and imaginary components of the simulated input impedance of $\lambda/4$ QHAs with different number of turns and varying axial length/radius ratio (R).

Radiation Pattern

As can be seen from Figure 2.9, the radiation pattern for the $\lambda/4$ QHA exhibits very little change with varying geometrical parameters. It is difficult to

achieve the wide beam and good axial ratio over the entire hemisphere that can be achieved with certain $\lambda/2$ and $3\lambda/4$ geometries. The cross-polarization component at low elevation angles becomes problematic and the front to back ratio is much worse than for the $\lambda/2$ and $3\lambda/4$ QHAs. However, for applications in which compact size is essential, the $\lambda/4$ QHA could provide acceptable radiation properties.

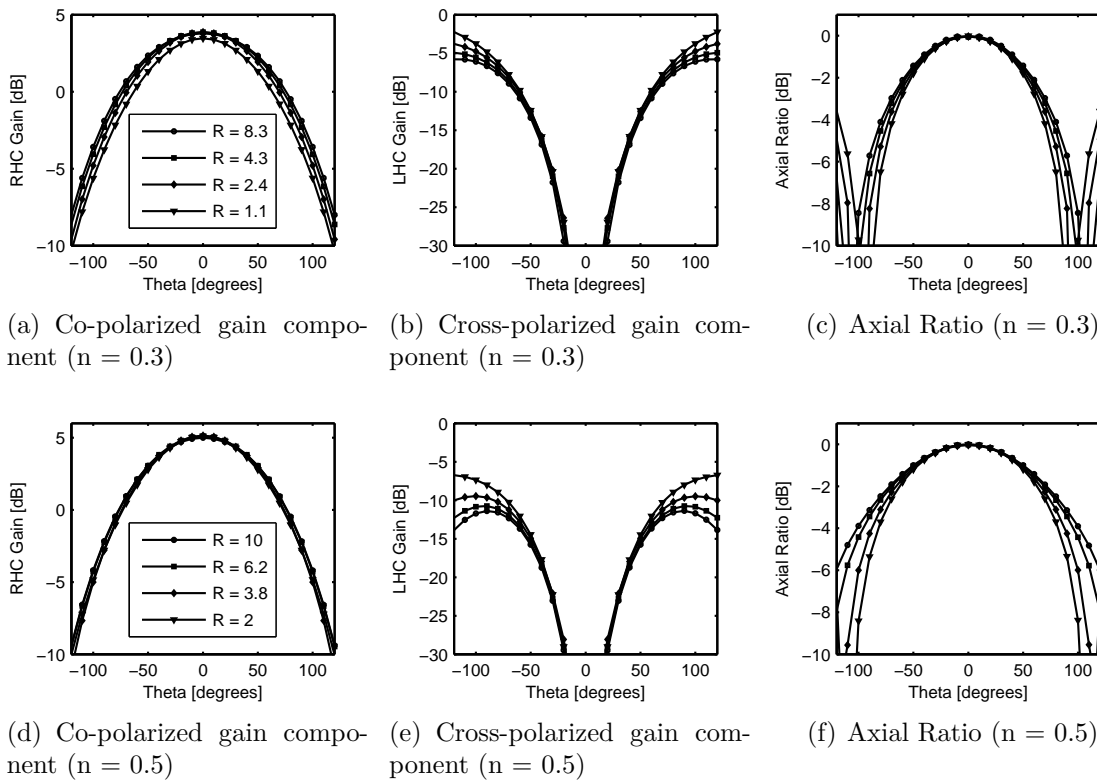


Figure 2.9: Elevation plane far-field radiation properties of $\lambda/4$ QHAs with different number of turns and varying axial length/radius ratio (R).

2.3 Self-Phased QHA

2.3.1 Physical Configuration

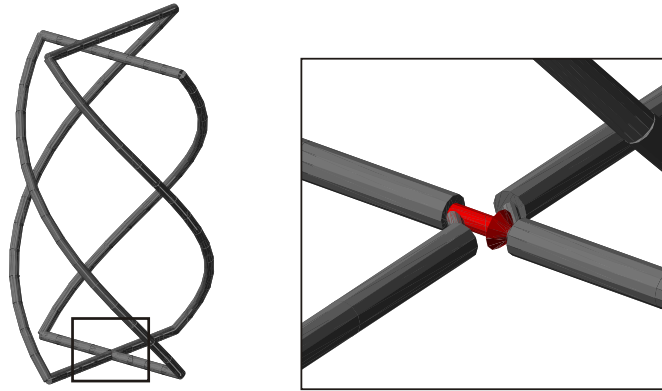


Figure 2.10: A FEKO simulation model of a self-phased QHA with detail of the parallel feed.

The self-phased QHA consists of two bifilar loops with different resonant lengths, fed in parallel. Figure 2.10 shows a FEKO simulation model of such an antenna with a detailed view of the parallel feeding arrangement.

2.3.2 Current Distribution and Input Impedance

To obtain the 90° current phase shift, the elements of one bifilar helix is adjusted to be longer than the resonant length so that the current has a phase lead of 45° ($Z_1 = R + jR$), and the other is adjusted to be shorter to obtain a phase lag of 45° ($Z_2 = R - jR$). When the two elements are excited by a single source at a common feed point in the parallel arrangement shown in Figure 2.10, the input impedance is R . This is only valid in the ideal case when the effect of coupling between the two elements is ignored, but serves as a good starting point for optimizing the design for both impedance match and the necessary quadrature phasing. The two impedances Z_1 and Z_2 generally have unequal amplitudes and a phase difference close to 90° only at resonance. This causes the degradation of radiation performance, particularly off resonance, as the two bifilars radiate unequal power with incorrect phasing. Figure 2.11 illustrates the asymmetrical current distribution in adjacent helical elements at frequencies above and below the center frequency (1.6 GHz). The two bifilar loops are close to resonance at frequencies of 1.55 GHz and 1.65 GHz respectively.

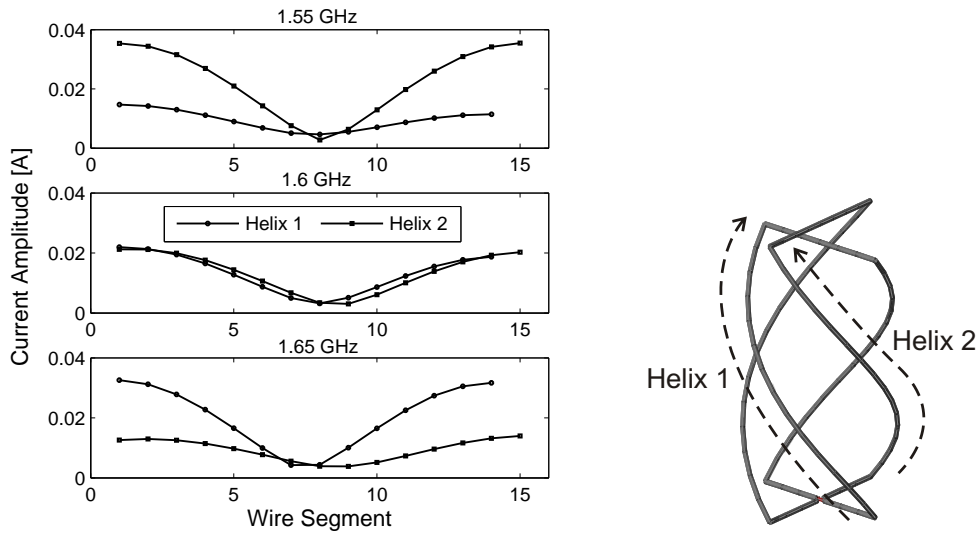


Figure 2.11: Current distribution along the helical elements at the center frequency (1.6 GHz) and at frequencies above and below the center frequency.

In Figures 2.4 and 2.5 the FEKO simulation results for a $\lambda/2$ QHA with 0.5 turns are shown. The axial length to radius ratio is kept constant for both bifilar loops to ensure similar radiation properties, while being adjusted together with the loop length to obtain the required real and imaginary input impedances. Figure 2.12 shows the resulting input impedances of the individual bifilar loops when the parallel combination was optimized for good impedance match at over both the Inmarsat receive and transmit bands (1.54 GHz and 1.64 GHz). The real and imaginary parts of the input impedance of the parallel-fed structure as well as the magnitude of the reflection coefficient (referenced to a 50 Ω system) is shown in Figure 2.13. Because of the double resonance of the structure, a wide impedance bandwidth is achieved.

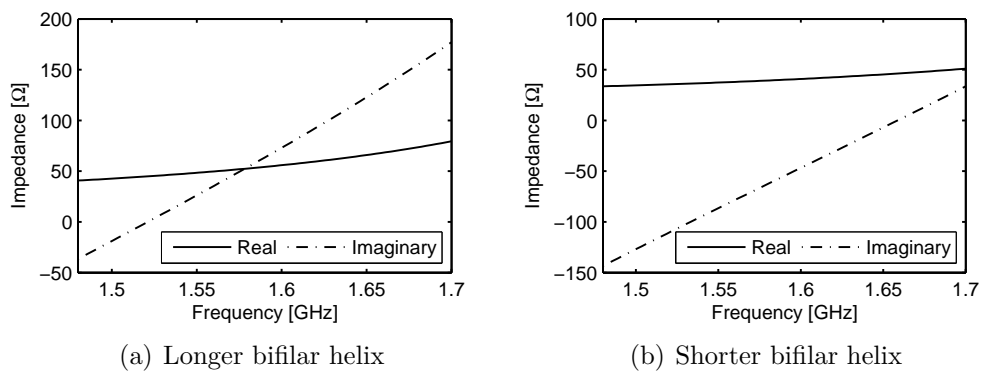


Figure 2.12: Simulated input impedances of the individually fed bifilar helices of the self-phased QHA.

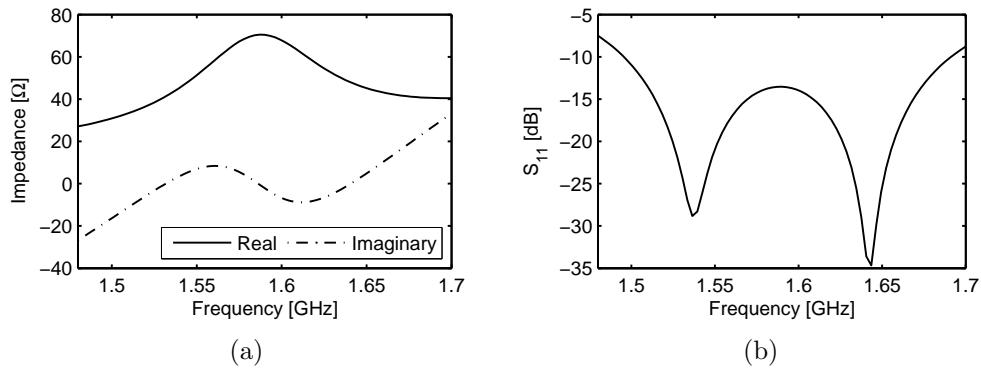


Figure 2.13: (a) Simulated input impedance of a parallel fed self-phased QHA. (b) Magnitude of the reflection coefficient (referenced to a 50Ω system).

2.3.3 Radiation Pattern

As is mentioned in Section 2.3.2, the self-phased QHA has an asymmetrical current distribution and the two bifilar helices radiate unequal power at frequencies away from the center frequency. This is illustrated by the simulated co-polarized component of the far field radiation pattern in Figure 2.14. A cardioid-shaped beam which is uniform in the azimuth plane is only possible at the center frequency.

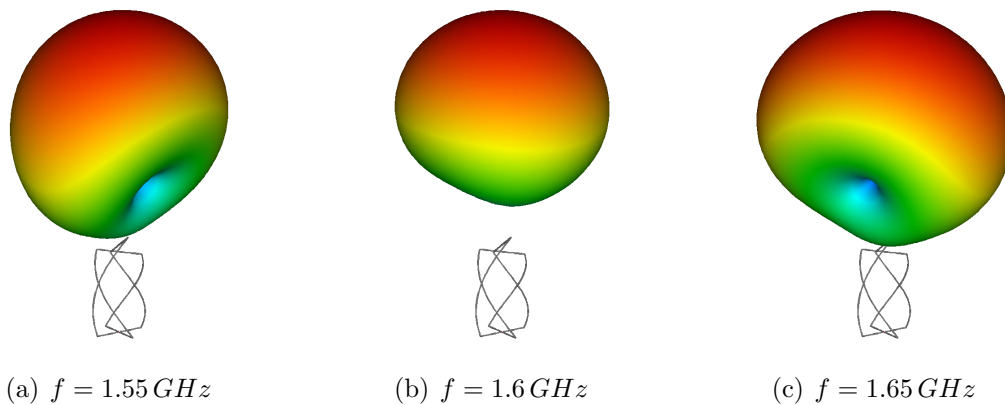


Figure 2.14: Illustrating the asymmetry in the radiation pattern of the self-phased QHA at frequencies away from resonance.

From Figure 2.15 it can be seen that the cross-polarization far-field component is much higher than for the quadrature fed QHAs of Section 2.2. A good axial ratio is only achievable over a much narrower beam width.

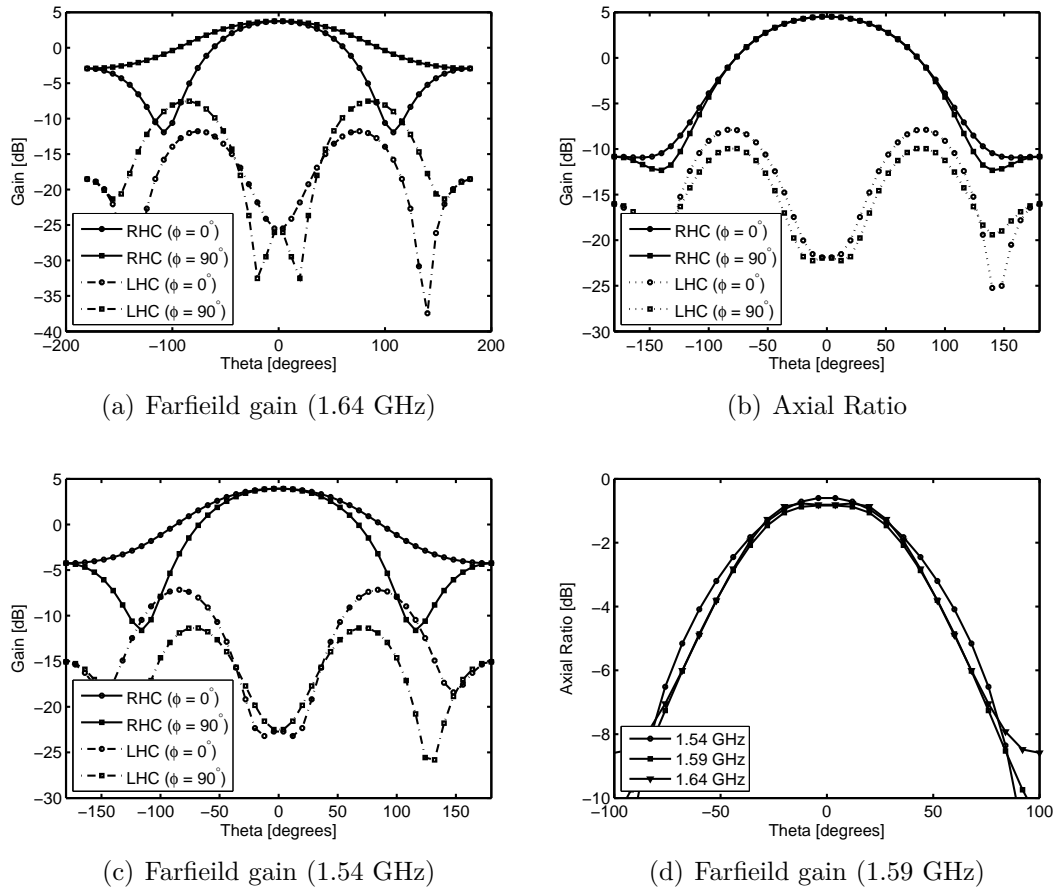


Figure 2.15: Showing the far-field gain components at frequencies (a) below resonance, (b) at resonance and (c) above resonance. Orthogonal elevation plane cuts at $\phi = 0^\circ$ and $\phi = 90^\circ$ are plotted to illustrate the asymmetrical pattern. In (d) the axial ratio at all three frequencies are plotted ($\phi = 0^\circ$).

2.4 Other QHA Configurations

2.4.1 Multi-turn QHAs with Shaped-Conical Radiation Patterns

By extending the resonant fractional-turn QHA to an integral number of turns, the radiated energy can be concentrated into a cone with the gain decreasing from a maximum at the edge of the cone to a local minimum at the center [8]. This pattern is desirable in many satellite ground station applications, as the distance to the satellite is smaller with the satellite at zenith compared to when it is just above the horizon. A uniform signal strength at the receiver can thus be achieved throughout the entire satellite pass.

Kilgus introduced the pitch distance (p) as well as the ratio $k = r/p$. The pitch distance is the distance between consecutive turns of one helical element

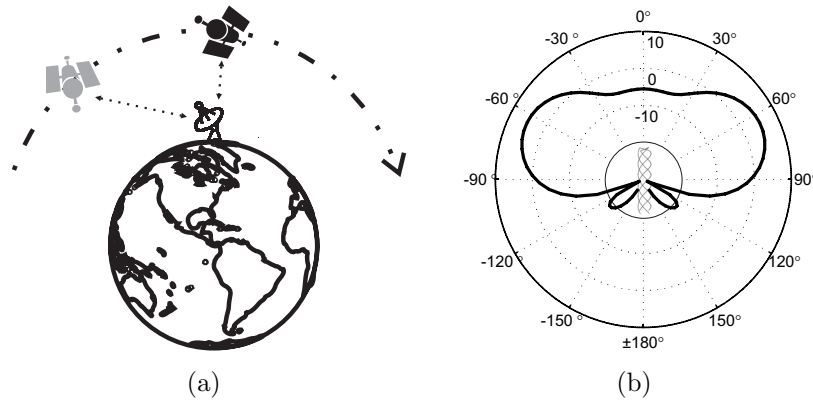


Figure 2.16: (a) Illustrating the varying distance between the satellite and the ground station. (b) A typical shaped-conical radiation pattern from a multi-turn QHA.

measured along the axis of the helix, and is related to the parameters of Figure 2.1 by

$$p = \sqrt{\left(\frac{h}{n^2}\right)^2 - 4(\pi r)^2} = \frac{l}{n} \quad (2.4)$$

Measured data indicated that the parameter range for shaped conical beams is bounded by regions of unsatisfactory performance such as multiple lobes and beams with no center minimum. Graphs of measured radiation characteristics for different parameter sets were presented, enabling the design of an antenna with a specifically shaped beam [8].

A multi-turn QHA with a shaped-conical patterns was designed as a ground station antenna for the ZA-002 South African Small Satellite programme. This is a low earth orbiting (LEO) satellite that can take high resolution pictures of any area in South Africa and enables collaboration with other countries. The center frequency of operation is 403 MHz . Using the data presented by Kilgus, the antenna was designed and simulated in FEKO. The final values of the geometrical parameters are given in Table 2.1.

Table 2.1: Geometrical parameters of the ground station antenna for the ZA-002 satellite programme.

Parameter	Description	Value
r	Volute radius	$34\text{mm} = 0.046\lambda$
l	Axial length	$983.2\text{mm} = 1.32\lambda$
p	Pitch Distance	$491.6\text{mm} = 0.66\lambda$
k	Ratio r/p	0.0692
n	Number of turns	2
gpr	Ground plane radius	$372.2\text{mm} = 0.5\lambda$

The FEKO simulation model and the co- and cross-polarized components of its far-field radiation pattern is shown in Figure 2.17. Figure 2.18 plots the input impedance of a single helical elements. As is discussed in Section 3.5.2, a much wider matched impedance bandwidth can be achieved by feeding the four helices with a quadrature phased feed network.

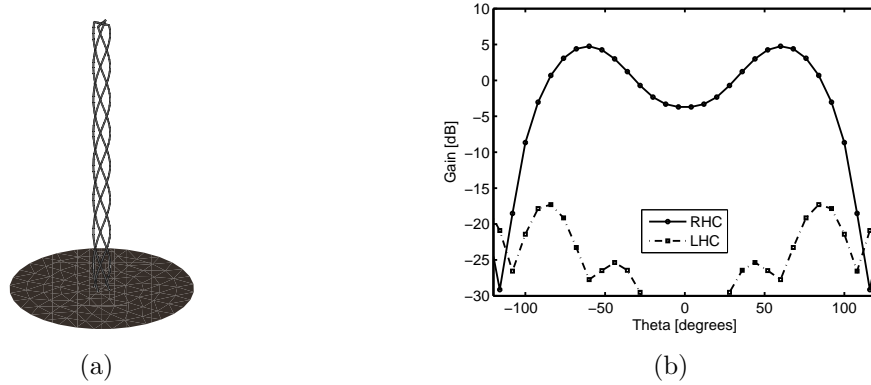


Figure 2.17: (a) Simulation model of the ZA-002 ground station antenna. (b) Co- and cross-polarized components of the far-field gain at 403 MHz.

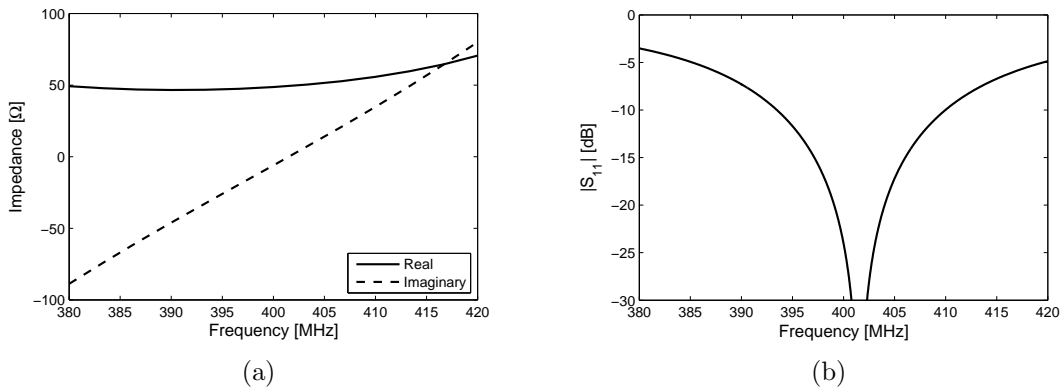


Figure 2.18: (a) Input impedance of a single helical element of the multi-turn ground station antenna. (b) Magnitude of the input reflection coefficient referenced to a $50\ \Omega$ system.

2.4.2 Printed Quadrifilar Helix Antenna

The printed quadrifilar helix antenna (PQHA) has also enjoyed popularity owing to its low cost and light weight [9, 10, 11]. It consists of a thin substrate on which the metallic radiating elements are printed and then shaped into a cylinder. This

antenna offers similar performance to its wire counterpart, while simplifying the manufacturing process to a great extent. Figure 2.19 shows an example of a PQHA FEKO simulation model. [12] reports a successful implementation of a PQHA operating in the Ku-band.



Figure 2.19: Example of a printed quadrifilar helix FEKO model.

2.4.3 Tapered QHAs

In an attempt to achieve good circularly polarized wide angle radiation with a low-profile radiating element, the use of QHA elements with a tapered profile is considered. For a given resonant length, the axial height of the element is reduced by increasing (or decreasing) the volute radius down the length of the antenna.

The FEKO model of a design which implements an exponential taper is shown in Figure 2.20. This complex looking shape is created by exponentially increasing the radius starting from the top end, while maintaining a constant amount of rotation (helical turn) per unit length. At any height h , the QHA radius is given by

$$\rho(h) = r_0 + e^{\alpha(1-\frac{h}{L})} \quad (2.5)$$

where r_0 is the starting radius at the top, and L is the total height of the volute. The scaling constant α is optimized at 3.8 for the presented design. The feed point is located at the top end of the helices, and a small ground plane is used to short the bottom ends. Feeding the antenna could be achieved by placing the feed cables vertically in the center of the antenna where the fields cancel due to symmetry. Alternatively, one could use an infinite balun structure where the helical elements are constructed of semi-rigid coaxial cable and the outer conductor used as radiating element. This scheme is similar to the feed point adjustment of Section 3.3.2.

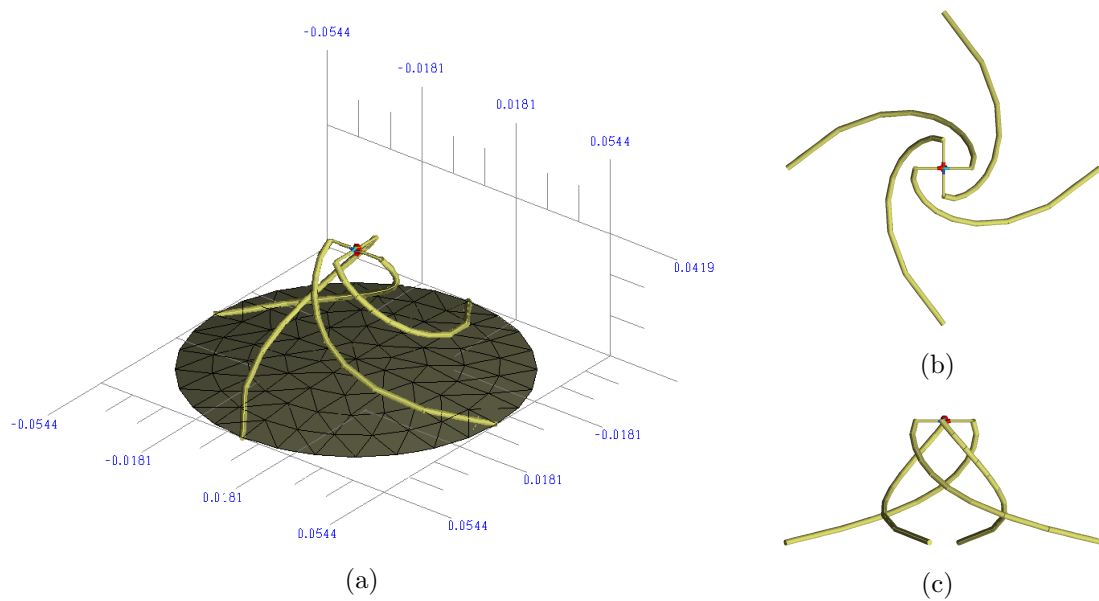


Figure 2.20: (a) Exponentially tapered QHA. (b) Top view. (c) Side View.

Figures 2.21 and 2.22 respectively show the radiation and impedance characteristics of the antenna. A wide, cardioid-shaped beam with good circular polarization is realized. The input impedance is matched to a 30Ω system, and the bandwidth will be increased by the use of a combining feed network to provide the quadrature phasing.

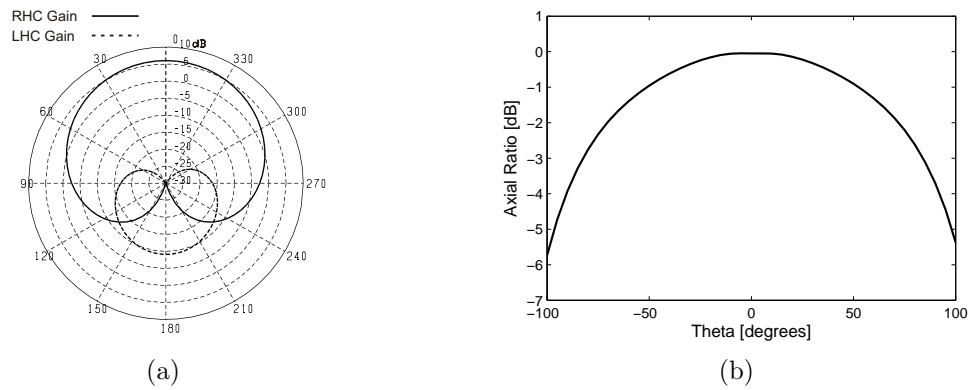


Figure 2.21: (a) Co- and cross-polarization components of the far-field radiation pattern. (b) Axial ratio in the elevation plane. $\phi = 0^\circ$.

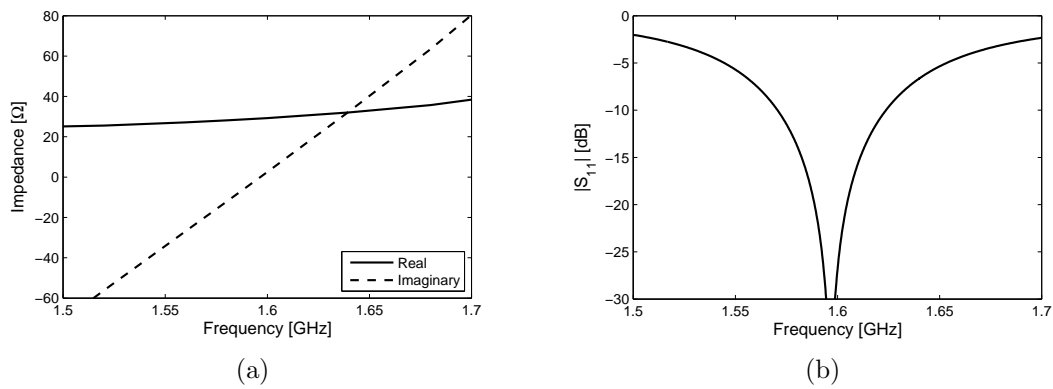


Figure 2.22: (a) Input impedance of the exponentially tapered QHA. (b) Magnitude of the input reflection coefficient referenced to a $30\ \Omega$ system.

2.5 Summary

A parametrical study of the traditional quadrature-fed QHA is presented. This is done for three variations which include the open-ended $\lambda/4$ and $3\lambda/4$ elements, as well as the $\lambda/2$ QHA with shorted ends. Generally longer elements with smaller radii radiates a wide beam with significant contributions and good axial ratio at low elevation angles. Shorter elements with larger radii tends to radiate directly towards broadside. Fed at the bottom ends, the $\lambda/4$ QHA has a very small input impedance and a radiation pattern that is rather insensitive to geometrical changes.

It is shown that by constructing two bifilar loops of different lengths and feeding them in parallel, the current can be forced to divide automatically with the correct quadrature phasing. Although this scheme greatly simplifies the feed network and offers a wider matched impedance bandwidth, it only produces the desired radiation characteristics over a small bandwidth where the current in the two bifilar loops is symmetrical.

By extending the fractional turn QHA to an integral number of turns, the radiated energy can be concentrated into a conical beam. This can be used to provide near uniform receiver signal strength for an entire satellite pass in ground station applications. A design for the *ZA – 002* programme is presented.

Other QHA configurations include the printed variety where the conducting helical elements is printed on a thin, cylindrically shapeable substrate. This provides a light weight, low cost alternative to the wire counterpart. The use of QHAs with tapered profiles is discussed as a method to achieve wide angle radiation with low profile elements.

Chapter 3

The QHA as Array Element

3.1 Introduction

The ability to scan effectively to low elevation angles with good circular polarization is an essential, distinguishing property of phased array antennas for aeronautical INMARSAT and other satellite tracking applications. This wide angle performance is generally difficult to achieve and is further complicated by the degrading effects of mutual coupling within an array environment.

Experimental investigation during the design of an existing product revealed that the addition of a parasitic circular disc above a cavity-backed, quadrature-fed crossed slot element improved the ability to scan to low elevation angles when this element is used in a tightly packed array [1]. This is counter-intuitive as the element pattern for a single element, with the parasitic patch present, is very directive. In an array environment however, the active single element pattern is much wider and under some circumstances even more directive towards the horizon. The patches had the effect of increasing the coupling between elements in the array and it was believed that some kind of traveling mode is assisting the ability to scan to low angles.

To examine the viability of using the QHA as an element in a wide angle, circularly polarized scanning array, the top patch is incorporated into the structure and compared to arrays of QHAs without the disc. An infinite ground plane is also added to the simulation model. Mainly two antennas are considered: a $\lambda/2$ QHA with the disc serving as a termination for the helices, and an open-ended $\lambda/4$ QHA with the disc floating parasitically above the helices. One of these is selected for which a prototype is manufactured and measured. A microstrip feed network is designed to provide input signals with the correct amplitude and phasing to the helices. As is discussed in Section 3.5.2, the feed network also

improves the impedance bandwidth. Measured results are given in Section 3.6.

3.2 Half-Wavelength QHA

3.2.1 Physical Configuration

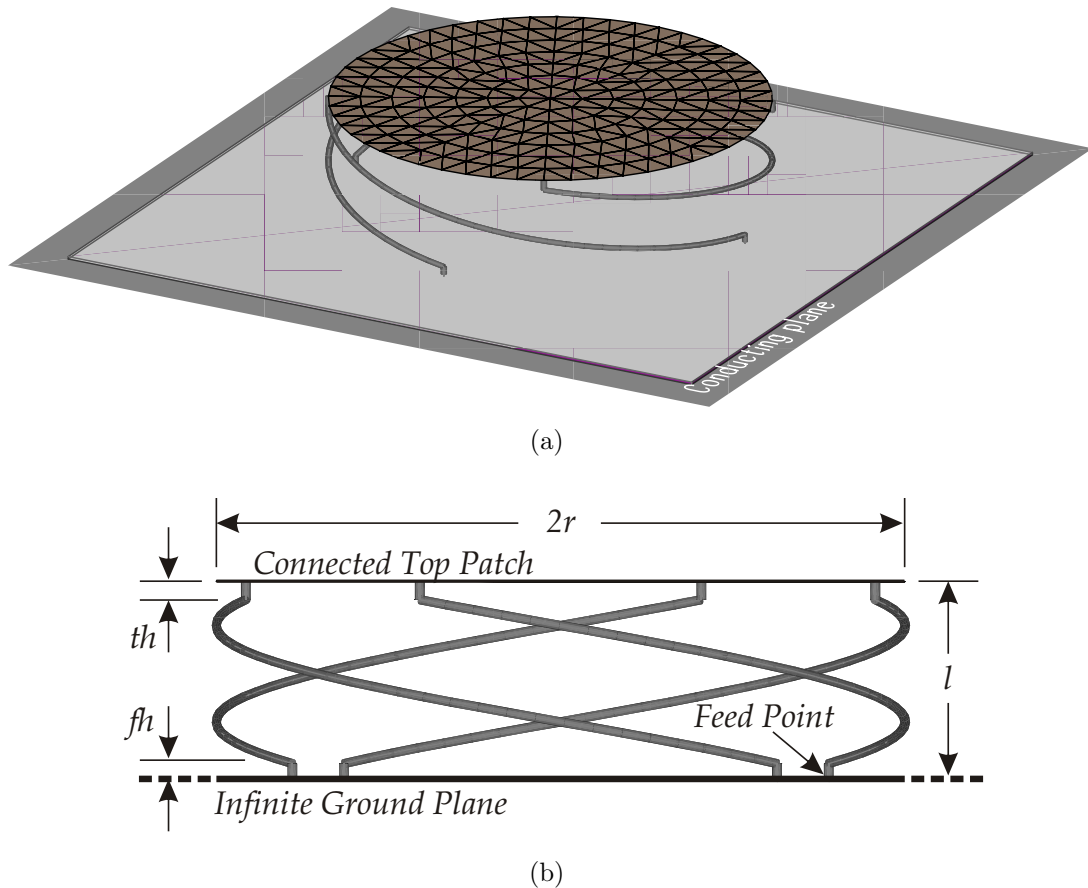


Figure 3.1: (a) Simulation model of the $\lambda/2$ QHA with top patch connected to the helical elements. (b) Side-on view of the $\lambda/2$ QHA showing the position of the shorting disc and other dimensional features.

The $\lambda/2$ QHA that is considered consists of four equispaced helical conductors of which the bottom ends are connected to an infinite ground plane, and the top ends are shorted together by a circular disc. Each helix is fed at the connection to the ground plane. In a practical model, the ground plane will also be the ground plane of a dielectric substrate on which a microstrip feed network is to be printed. The bottom ends of the helices will then be connected to the microstrip tracks – either directly in the case where the feed network is above the ground plane,

or via a hole in the ground plane and substrate when the microstrip tracks are underneath the ground plane.

Table 3.1 summarizes the values of the chosen geometrical parameters of the disk-shortened $\lambda/4$ QHA design that was considered for prototyping. The final choice of parameters was influenced by the impedance level necessary for the feed network design, far-field radiation properties and size constraints. In arriving at these values, extensive use was made of the developed parameter sweeping software of Appendix A. The impedance and radiation results presented in Sections 3.2.2 and 3.2.3 are for an antenna with these dimensions.

Table 3.1: Geometrical parameters of the disc-shortened $\lambda/2$ QHA considered for prototyping.

Parameter	Description	Value
r	Volute radius	$35 \text{ mm} = 0.187\lambda$
l	Axial length	$18 \text{ mm} = 0.096\lambda$
n	Number of turns	0.425
th	Top-end bend	2 mm
fh	Feed-end bend	2 mm
d	Conductor diameter	0.6 mm

3.2.2 Impedance

To enable the compacting of the feed network, the $\lambda/2$ QHA was designed to have an input resistance close to 90Ω . This allowed the microstrip lines of the hybrid circuits and matching sections to be routed close together as they have characteristic impedances for which the line widths are fairly narrow. The imaginary part of the input impedance at the helix feed point does not necessarily have to be zero, as it will be transformed to the desired value by a length of transmission line or another kind of matching circuit in the feed network. Figure 3.2 shows the input impedance of the $\lambda/2$ QHA with a top shorting disc at the feed point indicated in Figure 3.1 (b). This is the active impedance with all the other ports excited with the correct amplitude and phasing. When the antenna is combined with a feed network it will have a much improved impedance bandwidth, as is discussed in Section 3.5.2. The software of Appendix A was used to obtain the final values of the dimensional parameters which yield the desired input impedance.

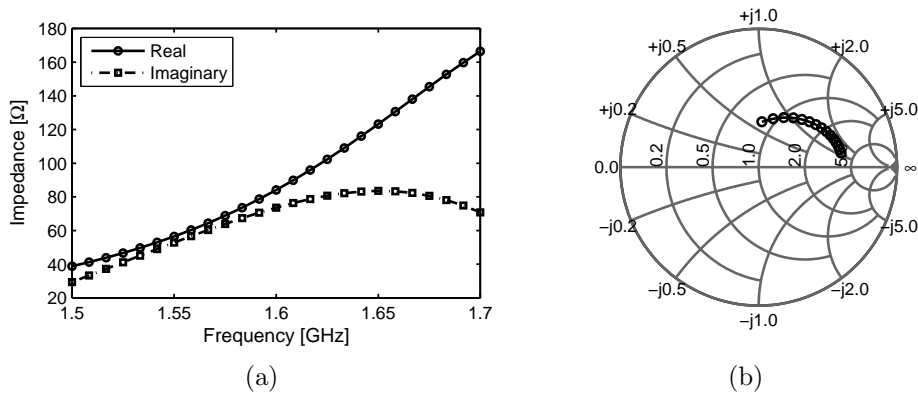


Figure 3.2: (a) Real and imaginary components of the simulated input impedance of the $\lambda/2$ QHA with shorting disc. (b) Smith chart plot of the input impedance (normalized to 50 Ω).

3.2.3 Radiation

To be useful as an element in an array for aeronautical applications, a low profile is essential. For QHAs this corresponds to having a small axial length/radius ratio. It can be seen from the parametrical studies in Chapter 2 that it is difficult to cover an entire hemisphere and achieve good axial ratio over a wide beam for small values of R (ie. low profile elements). When a large ground plane is introduced (as will be the case in an array environment) the axial ratio at low elevation angles is degraded even further. Figure 3.4 shows the simulated radiation properties of a $\lambda/2$ QHA of which the bottom ends are connected to a perfectly conducting, infinite ground plane, and the top ends are shorted together by radial wires.

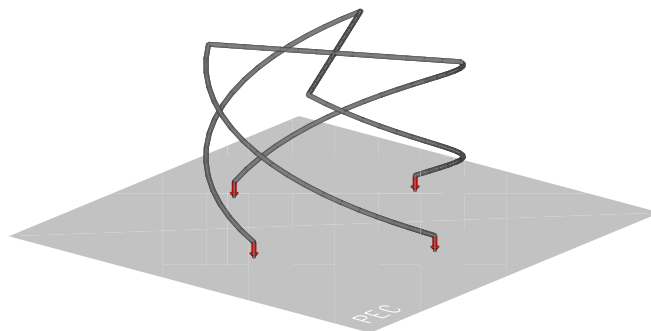


Figure 3.3: Example of a simulation model for the $\lambda/2$ QHA without the shorting disc.

When the top patch is introduced to short the helical elements there is a noticeable improvement in the axial ratio, especially at low elevation angles. As is

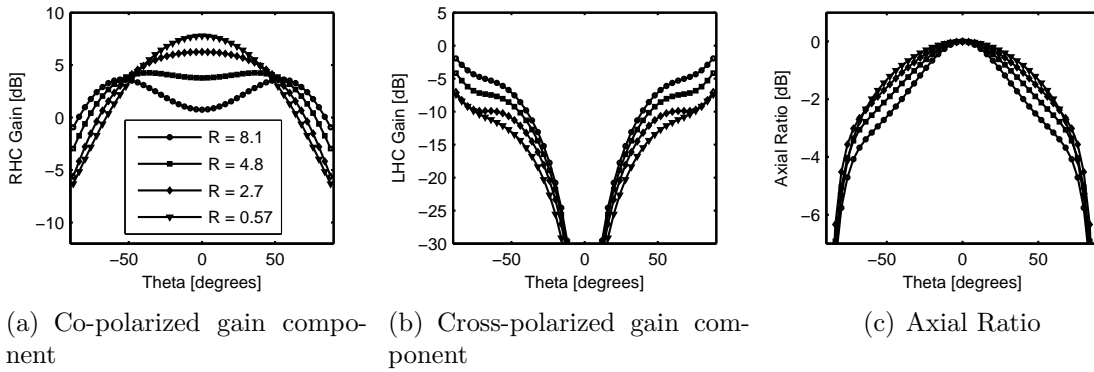


Figure 3.4: Elevation plane far-field radiation properties of a $\lambda/2$ QHA with an infinite ground plane and no shorting-disc for a varying axial length/radius ratio (R). $n = 0.425$.

the case with the cavity-backed crossed slot element of [1], the radiation pattern is very directive towards broadside with the top patch present. The simulated co- and cross-polarization gain components, as well as the axial ratio of a disc-shortened $\lambda/2$ QHA with the dimensions of Table 3.1 are plotted in Figure 3.5.

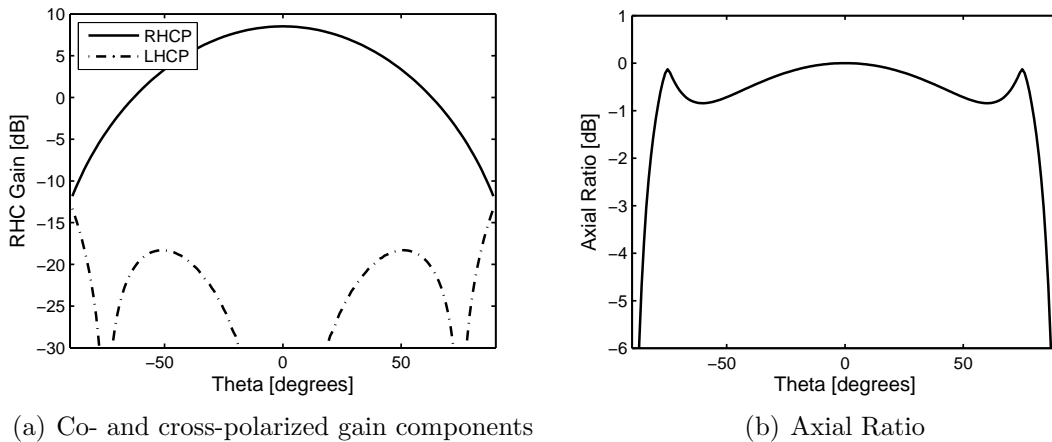


Figure 3.5: Far-field radiation characteristics of the $\lambda/2$ QHA with top shorting disk.

Of particular importance when the top patch is included in the structure, is the insensitivity of the radiation pattern to variations in axial length and number of turns. This allows the QHA to be designed with a very low profile while still achieving excellent axial ratio at low angles. The size of the disk (and consequently the QHA radius if the helical elements are attached to the edges of the disc) is the dominant factor influencing the radiation characteristics. Generally, larger patch sizes provide better low angle axial ratio performance, but as the

diameter approaches a quarter of a wavelength this starts to degrade. If the element is to be used in an array, the patch size is also limited by the spacing of elements within the array.

3.3 Quarter-Wavelength QHA

3.3.1 Physical Configuration

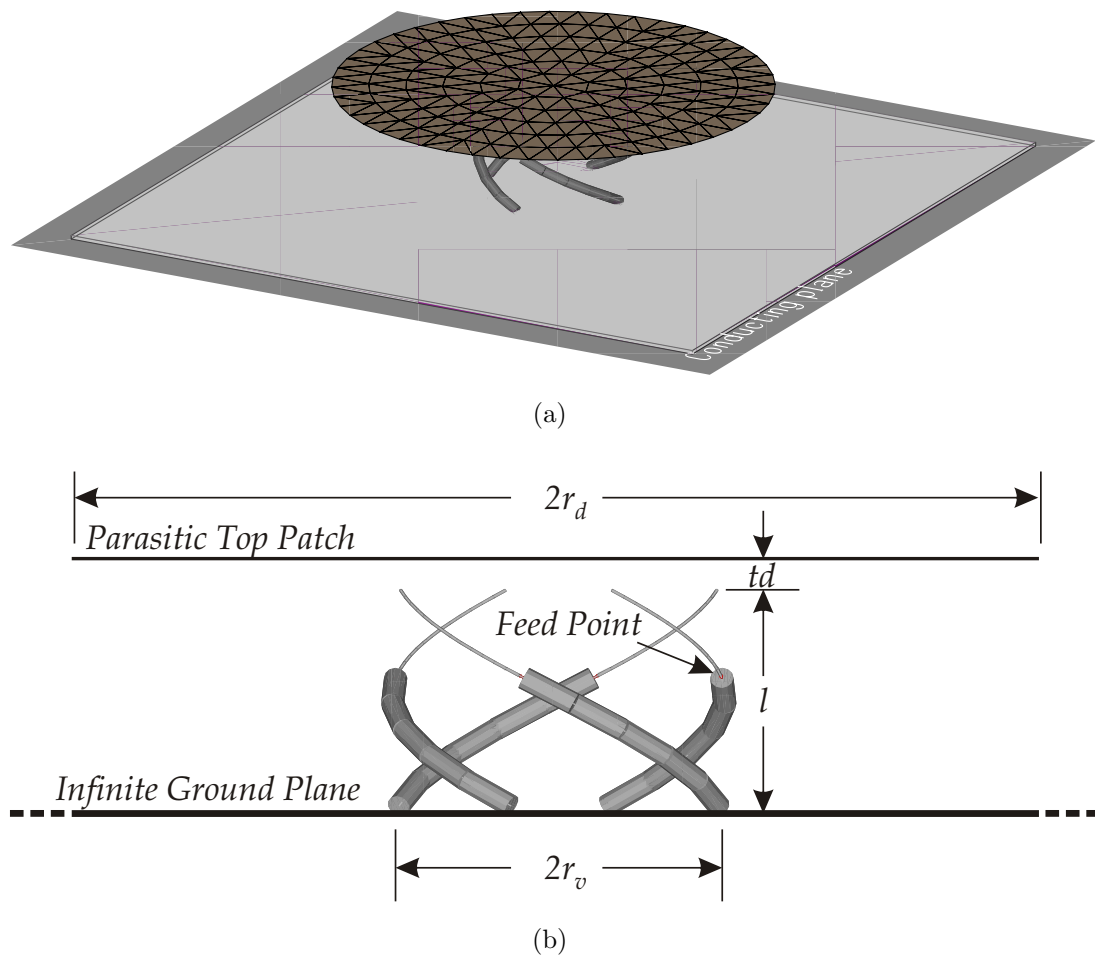


Figure 3.6: (a) Simulation model of the $\lambda/4$ QHA with parasitic top patch floating above the helical elements. (b) Side on view of the $\lambda/4$ QHA showing the position of the disc above the helices.

For the $\lambda/4$ QHA the helices and circular disc are not connected, but is separated by a distance td (see Figure 3.6). To enable the adjustment of the input impedance by moving the feed position (as will be discussed in Section 3.3.2), the helical conductors is constructed from semi-rigid coaxial cable. This is modeled in FEKO as a thick wire for the bottom part (outer conductor) and thin wire for

the top (center conductor). The feed is located at the junction between the two wires with different radii. Similar to the $\lambda/2$ counterpart, the bottom ends of the helices are connected to an infinite ground plane. In a practical model the semi-rigid cable will be extended through the ground plane and the center conductor attached to the output of a feed network. The outer conductor is shorted to the ground plane at the attachment point.

Table 3.2: Geometrical parameters of the $\lambda/4$ QHA with parasitic patch considered for prototyping.

Parameter	Description	Value
r_v	Volute radius	$29.6 \text{ mm} = 0.158\lambda$
r_d	Disc radius	$35 \text{ mm} = 0.187\lambda$
l	Axial length	$19 \text{ mm} = 0.101\lambda$
n	Number of turns	0.4
td	QHA and disc separation	3 mm
fp	Feed position (fraction of helical element)	0.65
d_o	Outer conductor diameter	2.1 mm
d_i	Inner conductor diameter	0.29 mm

3.3.2 Input Impedance and Feed Point Adjustment

When fed at the connection between the helical elements and the ground plane, the $\lambda/4$ QHA with open-circuited ends has a very low input resistance. This makes it very difficult to match the antenna to the feed network. With the ends open-circuited and the length adjusted for resonance, the helical conductors have a sinusoidal current distribution with a null at the end and a maximum at the ground plane junction (Figure 3.7). By moving the feed up the helical element to a point of lower current, the input impedance can be adjusted to a desired level.

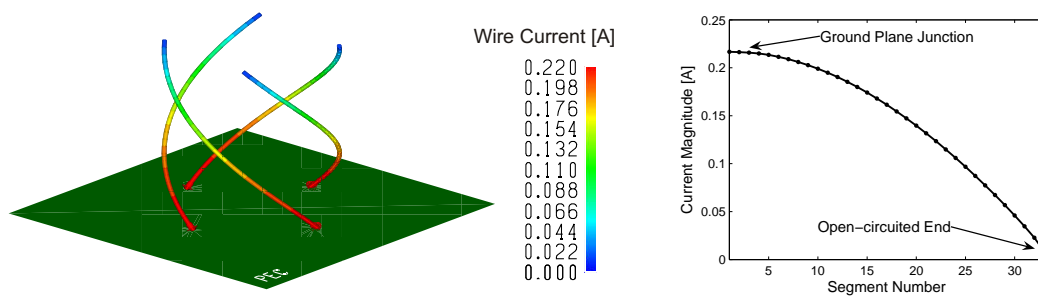


Figure 3.7: Current distribution on the helical conductors.

Practically, this can be accomplished by constructing the QHA from semi-rigid coaxial cable. At the point where the feed is to be located, the outer conductor and dielectric is removed and only the inner conductor is extended to the end of the helical element. Due to the skin effect the current will curl around and flow on the outside of the outer conductor. This is illustrated in Figure 3.8 (a). The problem is thus separated into two parts: a length of coaxial cable up to the feed point, and the radiating currents on the outside of the outer conductor and the protruding center conductor. In Figure 3.8 (b), the FEKO simulation model for the structure is shown. It consists of two helical conductors between which the source is located. The diameter of the bottom conductor corresponds to the outside diameter of the semi-rigid outer conductor, and the top conductor is the same as the semi-rigid center conductor. The length of coaxial cable acts as an impedance transformer and the input impedance extracted from FEKO needs to be adjusted according to

$$Z_{in} = \frac{Z_L + jZ_0 \tan \beta l}{Z_0 + jZ_L \tan \beta l} \quad (3.1)$$

where Z_L is the impedance at the feed point, Z_0 is the characteristic impedance of the coaxial line, $\beta = 2\pi/\lambda$ is the propagation constant for the approximated lossless line, and l is the length of transmission line extended from the simulated feed point.

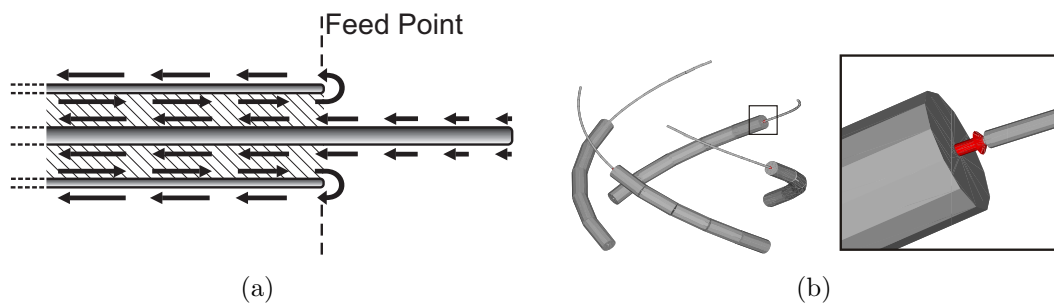


Figure 3.8: (a) Illustrating the currents on the coaxial cable. (b) FEKO simulation model of the helical elements with expanded feed point detail. (The ground plane and top patch are not shown).

The potential $\lambda/4$ prototype was designed to have an input resistance close to $75\ \Omega$ at the connection to the ground plane. The reason for this is that when a $75\ \Omega$ semi-rigid coaxial cable is used to construct the helices, the input impedance at the simulated feed point (located higher up on the helical element) can be matched to $75\ \Omega$ without the need to factor in the impedance transformation from the length of transmission line. This also provides a convenient impedance level for which a microstrip feed network can be designed. In Figure 3.9 the input impedance at the feed point and the transformed impedance at the ground plane is shown.

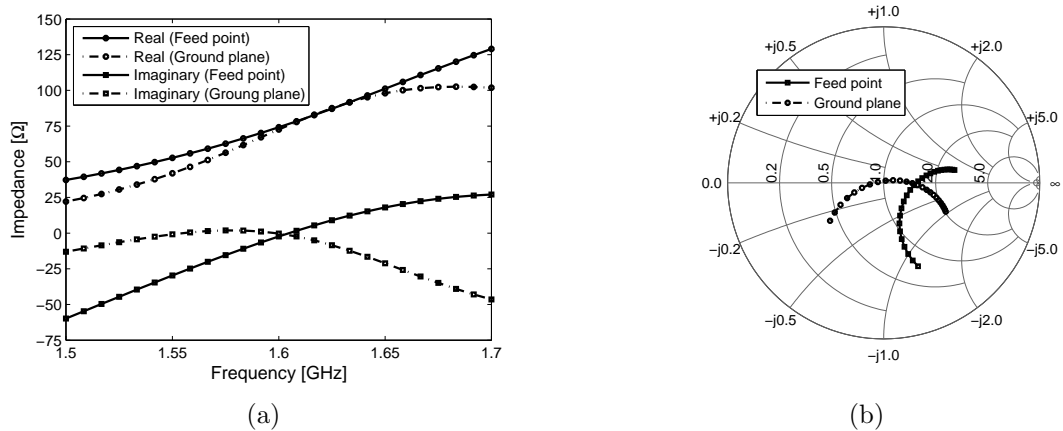


Figure 3.9: (a) Real and Imaginary components and (b) a Smith chart plot of the input impedance at the simulated feed point and at the ground plane of the $\lambda/4$ QHA. The Smith chart is normalized to $50\ \Omega$.

3.3.3 Radiation

As is the case for the $\lambda/2$ QHA of Section 3.2.3, there is noticeable improvement in low elevation angle axial ratio performance when the parasitic disc is introduced. The size of the disc is the dominant parameter in determining the radiation properties. Once again larger patch sizes have better low angle axial ratios up to a point where the diameter of the disc approaches a quarter of a wavelength. Figure 3.10 shows the radiation properties of a QHA with the configuration of Section 3.3.1 and dimensions given in Table 3.2.

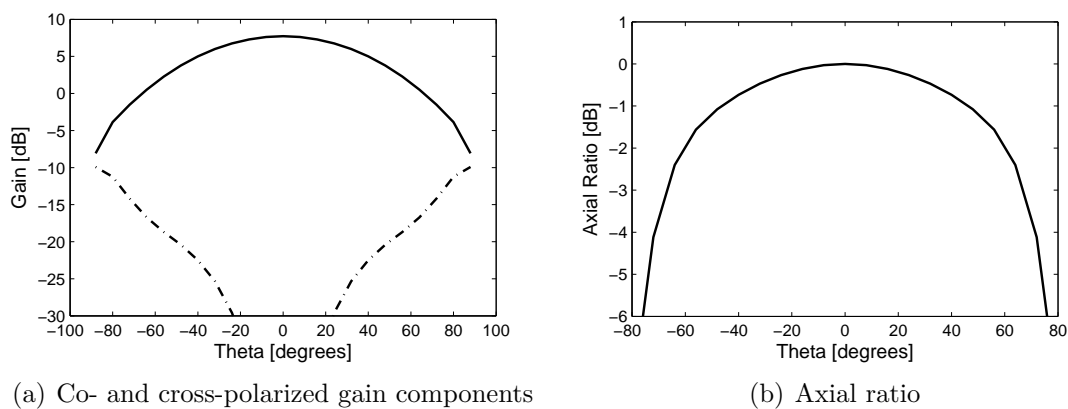


Figure 3.10: Far-field radiation characteristics of the $\lambda/4$ QHA with parasitic disc.

3.4 Chosen Element for Prototype

Further simulations were done in which certain asymmetries were introduced to the structure to investigate the effects that tolerances introduced with manual construction will have on the performance of the antenna. Of particular importance was the sensitivity of the $\lambda/4$ QHA to dissimilar distances between the top ends of the helices and the parasitic disk (td in Figure 3.6 b). This varying capacitance had a strong degrading influence on both the input impedance and radiation performance. Mainly for this reason it was decided to manufacture the $\lambda/2$ QHA element with the helices connected to the top disk, as this is easier to construct, and less sensitive to asymmetries in the structure.

3.5 Feed Network

The microstrip circuit designed to feed the QHA has to meet certain demands, the most obvious being the generation of equal amplitude signals with quadrature phasing at the antenna input terminals. As the QHA is designed to be used as an element in an array, the feed network must be compact enough so as to not interfere with the spacing of antenna elements in the array. It must also provide a good impedance match between the antenna and the source, and should have a low insertion loss. This section outlines the design and simulation of the microstrip feed network for the $\lambda/2$ QHA.

3.5.1 Obtaining the Active Antenna Input Impedance from Exported S-Parameters.

In the design of the antenna in Section 3.2, the input impedance achieved through simulation is the active input impedance of one fed helical element when all the others are fed with the correct relative phasing and amplitude. To enable the convenient optimization of the feed network, the 4-port S-parameters exported from FEKO needs to be decoupled to obtain four identical 1-ports. This will prevent the input impedance at an antenna port from being influenced by an incorrect signal at another port while the feed network is adjusted to obtain the desired impedance match and output signals. In the ideal case where the output signals of the feed network have equal amplitude and symmetrical quadrature phasing, the input impedance at each of the four original ports will be exactly the same as for the decoupled 1-port.

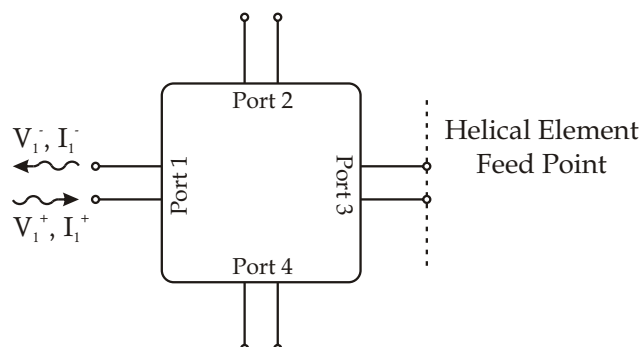


Figure 3.11: 4-port representation of the QHA for which the feed network is designed.

Consider the QHA as the 4-port network shown in Figure 3.11, where V_n^+ is the voltage wave incident on port n , and V_n^- is the voltage wave reflected from

port n . The scattering matrix $[S]$ is defined in relation to these incident and reflected voltage waves as

$$\begin{bmatrix} V_1^- \\ V_2^- \\ V_3^- \\ V_4^- \end{bmatrix} = \begin{bmatrix} S_{11} & S_{12} & S_{13} & S_{14} \\ S_{21} & S_{22} & S_{23} & S_{24} \\ S_{31} & S_{32} & S_{33} & S_{34} \\ S_{41} & S_{42} & S_{43} & S_{44} \end{bmatrix} \begin{bmatrix} V_1^+ \\ V_2^+ \\ V_3^+ \\ V_4^+ \end{bmatrix} \quad (3.2)$$

or

$$[V^-] = [S] [V^+] \quad (3.3)$$

If the helical elements are fed with equal amplitude and quadrature phasing, and there is negligible reflection due to mismatch between the antenna and the feed network, the normalized incident voltage vector is

$$[V^+] = \begin{bmatrix} 1\angle 0^\circ \\ 1\angle 90^\circ \\ 1\angle 180^\circ \\ 1\angle 270^\circ \end{bmatrix} = \begin{bmatrix} +1 \\ +j \\ -1 \\ -j \end{bmatrix} \quad (3.4)$$

From 3.2 and 3.4, the reflection coefficient at port 1 can now be written as

$$\begin{aligned} \Gamma_1 &= \frac{V_1^-}{V_1^+} = S_{11} + \frac{1}{V_1^+} (S_{12}V_2^+ + S_{13}V_3^+ + S_{14}V_4^+) \\ &= S_{11} + jS_{12} - S_{13} - jS_{14} \end{aligned} \quad (3.5)$$

Due to symmetry, the reflection coefficients at all four ports are identical and can be viewed as the S_{11} of four decoupled 1-ports, provided that the feed network is generating the correct feed signals and an acceptable impedance match between the antenna and feed network is achieved. This reflection coefficient is related to the active input impedance by

$$Z_{in} = Z_0 \frac{1 + \Gamma}{1 - \Gamma} \quad (3.6)$$

where Z_0 is the characteristic impedance used in the calculation of the original S-parameters. It is to this input impedance that the output terminals of the feed network should be matched.

3.5.2 Impedance Bandwidth Improvement

When combined with a feed network that provides quadrature phasing, the QHA (or any other narrowband resonant structure) will have an improved impedance bandwidth. The reason for this is illustrated on the Smith chart of Figure 3.12. In the simplest case, the 90° phase shift is accomplished by adding a $\lambda/4$ length of transmission line. This has the effect of rotating the impedance on the Smith chart by 180° around the characteristic impedance point of the transmission line (center of the Smith chart in the case of Figure 3.12). When this impedance is combined in parallel with the original impedance, it has a notably improved impedance bandwidth (tighter grouping on the Smith chart). The input resistance is roughly half of the original value, and the reactance is close to zero over a wider frequency band.

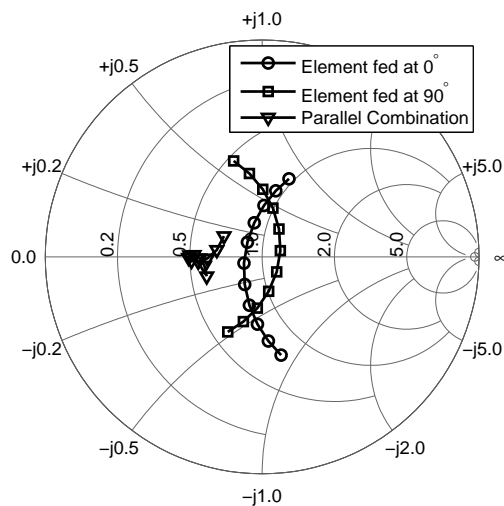


Figure 3.12: Illustrating the improvement in impedance bandwidth when to quadrature phased elements are fed in parallel.

3.5.3 Design of the Feed Network

Size

To enable the entire element consisting of the radiating QHA and the feed network to function as an independent unit within an array, the microstrip feed network is designed to fit underneath the antenna. This entails that the entire circuit be able to fit within a circular area of radius $r = 35 \text{ mm}$ (from Table 3.1). The

output terminals of the feed network should correspond to the connection points between the helical elements and the ground plane.

Different Topologies

Two options were considered to provide the necessary phase shift and power division at the antenna ports.

The first, and easiest, is to use lossless T-junction power dividers for the equal division of the input signal between the output ports. The necessary quadrature phase shift is then achieved by adding different multiples of $\lambda/4$ transmission line lengths to the signal paths. As is discussed in Section 3.5.2, this scheme will provide a good impedance match at the input port over a wide band. It can even be optimized to provide equal power division over two frequency bands (corresponding to the Inmarsat transmit and receive bands at 1.54 GHz and 1.64 GHz). An inherent problem with using lengths of transmission line to provide the required phase shift is that it is only accurate over a narrow band. To achieve good axial ratio it is imperative that the four helical conductors of the QHA is fed with exact quadrature phasing - a requirement that cannot be met with this topology, making it unsuitable for the application.

An alternative network of which a diagram is shown in Figure 3.13 (a), consists of two 90° hybrids and one 180° degree hybrid. In Figure 3.13 (b) and (c), schematic circuits of the hybrid networks are given in normalized form. The bandwidth of the hybrid circuits is in the order of 20–30%, making it suitable to be used in the feed circuit for the QHA [13].

Impedance Match, Power Transfer and Phasing

The hybrid circuits will inherently have a good input impedance bandwidth, as reflections due to mismatch will be dissipated in the resistive termination (R in Figure 3.13). As a consequence, the feed network should be optimized to have equal power transfer to all the output ports, minimum insertion loss and accurate quadrature phasing over the required frequency band.

At the inputs and outputs of the 90° hybrids, the impedance is $90\ \Omega$. The output lines are extended by tapered lines to provide an impedance match to the input of the antenna, as well as to create a mechanically robust attachment point for the helical wires. From Figure 3.13 it can be seen that the impedance for the wider arms of the hybrid is $90/\sqrt{2} \simeq 64\ \Omega$. Also, the in- and output ports and connecting sections of the 180° hybrid has impedances of $64\ \Omega$ and $\sqrt{2} \cdot 64 \simeq 90\ \Omega$ respectively. Lines transforming the impedance is added to match the output of

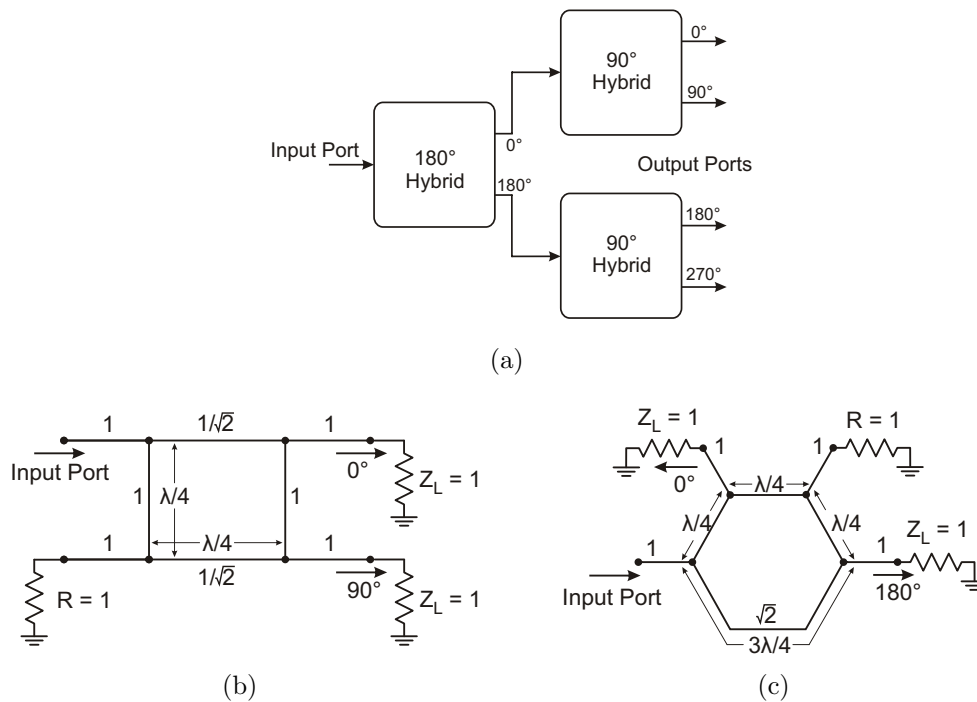


Figure 3.13: (a) Simplified diagram of the hybrid feed network. Normalized schematic circuits of the (b) 90° and (c) 180° hybrid networks.

the 180° hybrid to the inputs of the 90° hybrids, and the input of the 180° hybrid to the 50 Ω input of the entire circuit.

The dielectric substrate used for the microstrip circuit is *RO 4003* from Rogers with $\epsilon_r = 3.38$ at the frequency of operation [14]. With a height of 0.5 mm, the track widths for the required characteristic impedances are just wide enough to enable accurate manufacturing. The highest line impedance is about 90 Ω, corresponding to a track width of 0.3 mm. This narrow line widths simplifies the compacting of the feed network to fit into the permitted space.

Applied Wave Research’s Microwave Office is used in the design, verification and optimization of the feed network. By defining the lengths, widths and bending radii parametrically as a set of interdependent equations, the required response can be adjusted while still satisfying the dimensional constraints. An exported layout of the microstrip tracks of the final design is shown in Figure 3.14.

In Figure 3.15 the relative power (with a 0 dBm signal at the input to the feed network) and phase of the signals at the four output ports of the the feed network are plotted. The impedances and line lengths of the feed network are optimized for equal power division with minimum insertion loss, and accurate quadrature phasing around the Inmarsat receive and transmit bands (1.54 GHz

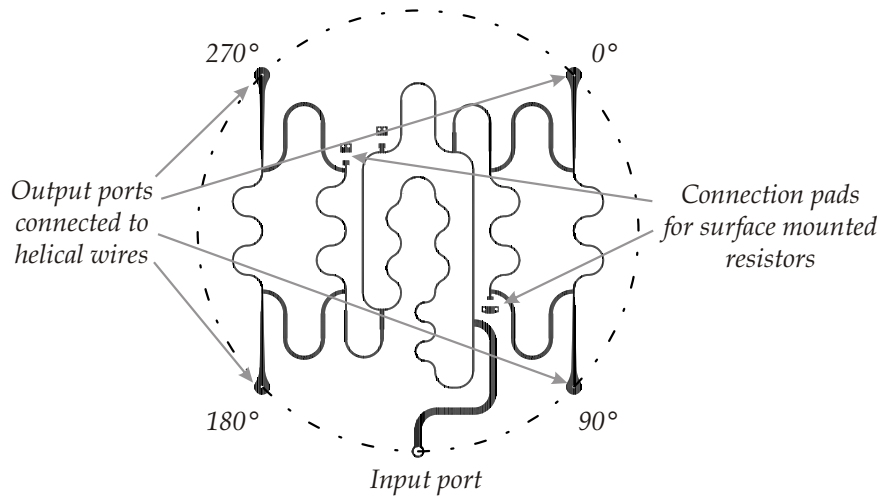


Figure 3.14: Layout of the microstrip feed network.

and 1.64 GHz). The use of hybrid networks ensures good quadrature phasing over the entire band. Figure 3.16 illustrates the inherent wide impedance bandwidth of the hybrid networks which is a result of the reflected power due to mismatch being dissipated in the resistive terminations.

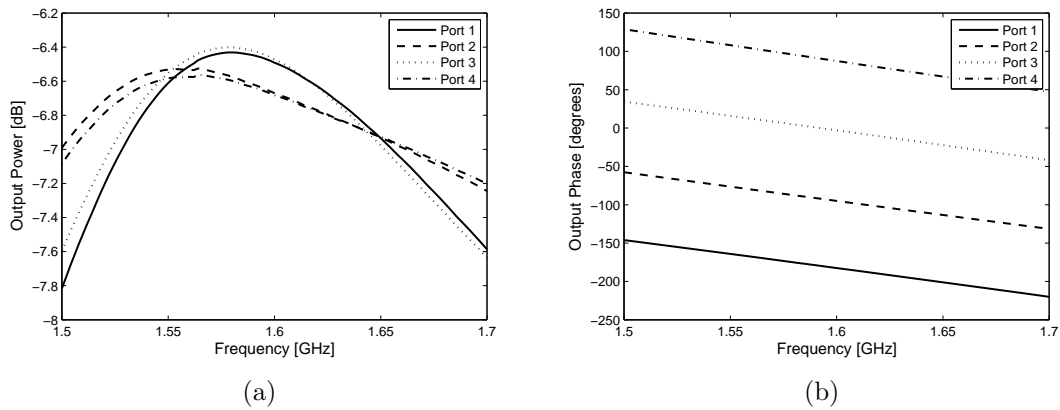


Figure 3.15: (a) Power delivered at the output ports of the feed network with a 0 dBm signal applied at the input. (b) Relative phase of the signals at the output ports.

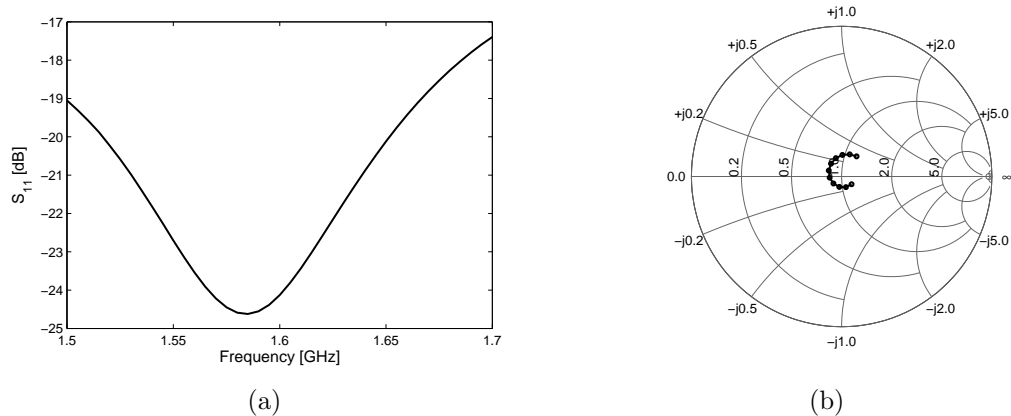


Figure 3.16: (a) Reflection coefficient at the input of the feed network when the FEKO S-parameter model of the antenna is connected to the output ports. (b) Smith chart plot of the reflection coefficient at the input port.

3.5.4 Verification with FEKO

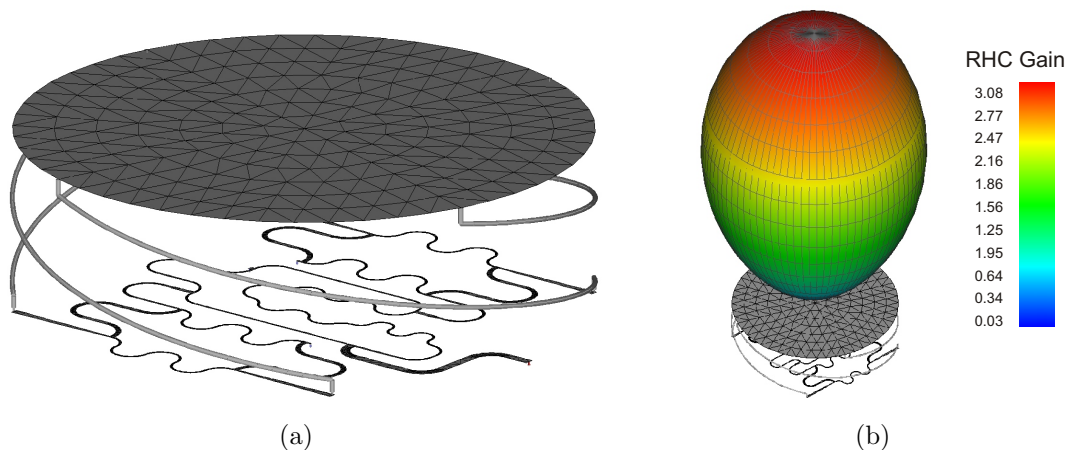


Figure 3.17: (a) FEKO simulation model with the QHA connected to the microstrip feed network imported from Microwave Office. The infinite dielectric layer and ground plane are omitted. (b) Co-polarized gain component illustrating the directive radiation pattern of the single element $\lambda/2$ QHA in isolation.

The microstrip layout is exported from Microwave Office in DXF format to enable the inclusion in FEKO. This is imported as a metal layer of meshed triangles. The Green's Function (GF) card in FEKO is used to model the dielectric substrate and ground plane as an infinite dielectric layer with an infinite conducting plane at the bottom. Resistively loaded wire segments connect the terminated ports of the hybrid circuits to the ground plane to model the terminations. The microstrip feed is also modeled as a wire segment to ground, and could add some

series inductance to the input impedance. At the ends of the feed network output ports, the bottom ends of the QHA helices of Section 3.2 are connected to the microstrip tracks. The complete model without the infinite dielectric layer and ground plane is shown in Figure 3.17.

Figure 3.18 shows the very good impedance match achieved at the input of the feed network which is largely attributed to the inherently large impedance bandwidth of the hybrid circuits. A better indication of the performance of the feed network and antenna combination are the plots of the current magnitude and phase of the segments connecting the helices to the microstrip tracks of Figure 3.19. The good power division and acceptable quadrature phasing of the signals fed to the four ports of the QHA produces the radiation performance shown in Figure 3.20. This compares very well with the results of the QHA model fed by the ideal sources of Section 3.2.

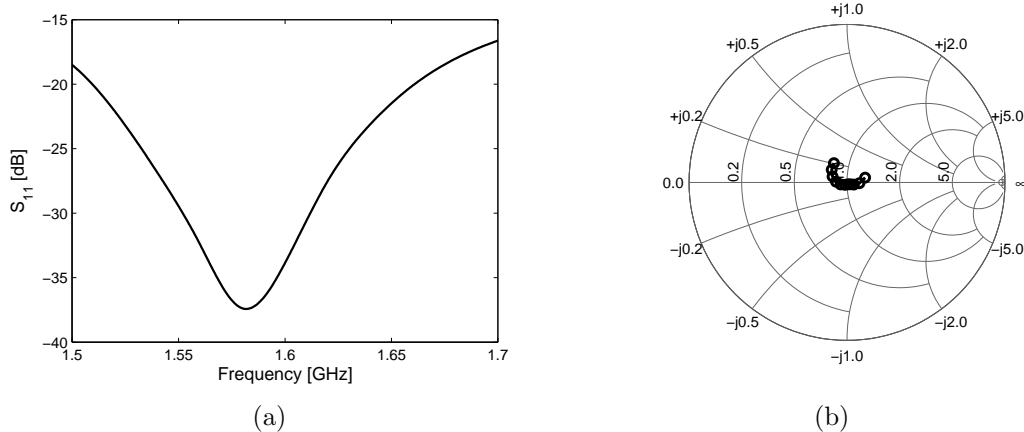


Figure 3.18: (a) Magnitude and (b) Smith chart plot of the input impedance reflection coefficient of the feed network with antenna connected (FEKO simulation).

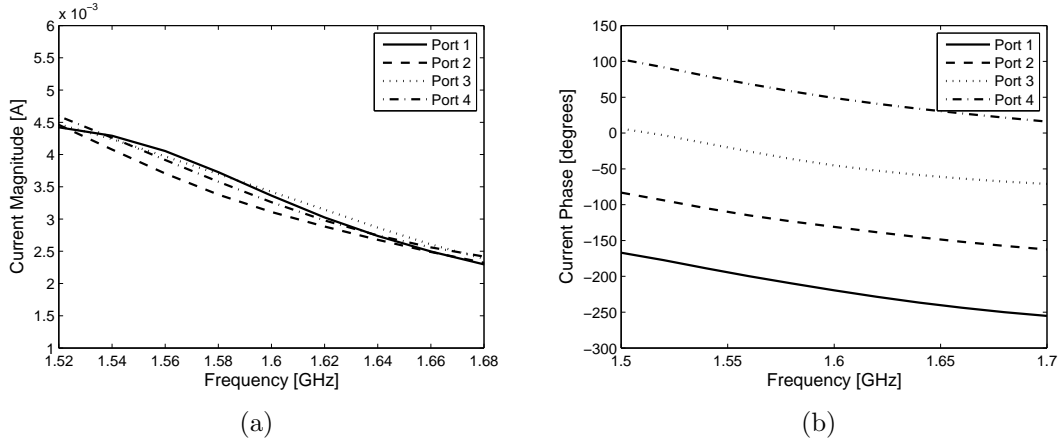


Figure 3.19: (a) Magnitude and (b) phase of the current in the segments that connect the microstrip tracks to the helices.

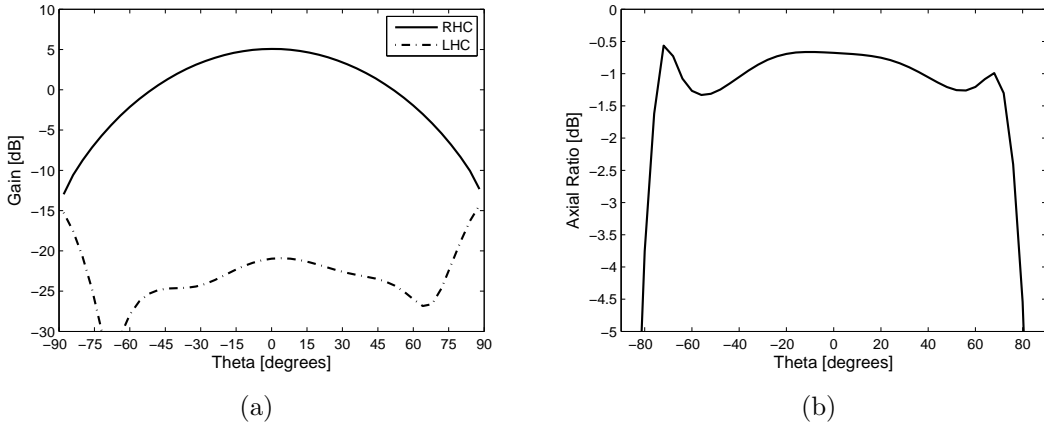


Figure 3.20: Simulated (a) gain and (b) axial ratio of the $\lambda/2$ QHA prototype fed by the microstrip feed network. $\phi = 0^\circ$.

3.6 Measured Results

Figure 3.21 shows the printed feed network as well as the complete assembled QHA that was built with the values of the dimensional parameters summarized in Table 3.1. The top shorting disc is printed on the thinnest available dielectric substrate (0.2 mm FR4) to minimize its effect on the fields. A cylindrical foam disk supports the substrate and maintains the shape of the bent helical wires. The tracks of the microstrip feed network is positioned on top (antenna side) with the bottom ends of the helices soldered directly to them.

The measured far-field radiation pattern of Figure 3.23 shows reasonable agreement with the simulations of Section 3.5.4. A slight asymmetry is noticed, and can be attributed to the considerable tolerances introduced to the struc-

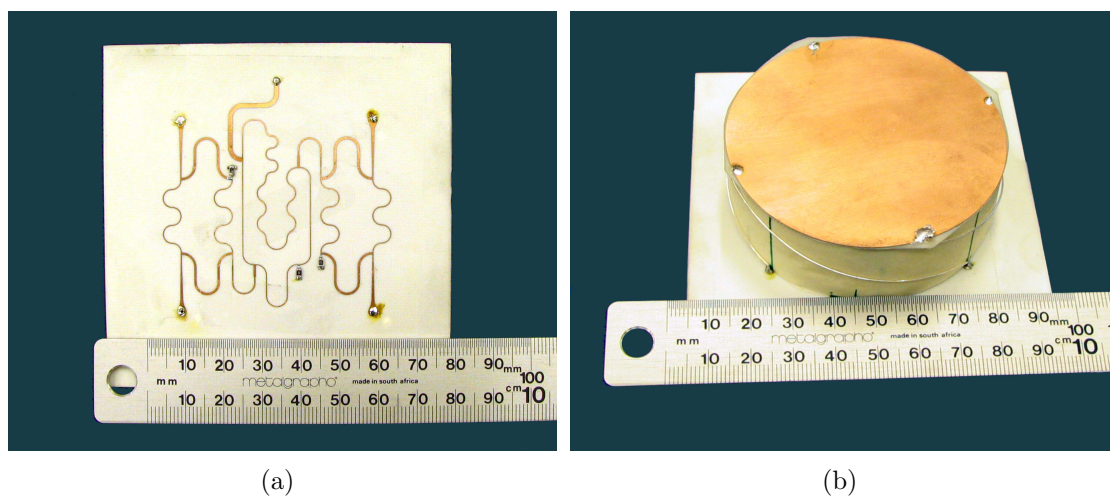


Figure 3.21: (a) Microstrip feed network. (b) $\lambda/2$ QHA with top shorting disc prototype connected to the feed network.

ture when constructing it by hand. The helical wires are particularly difficult to shape with precisely accurate pitch angle, resonant length and symmetry. A good impedance match is achieved over the entire frequency band of interest at the input of the feed network.

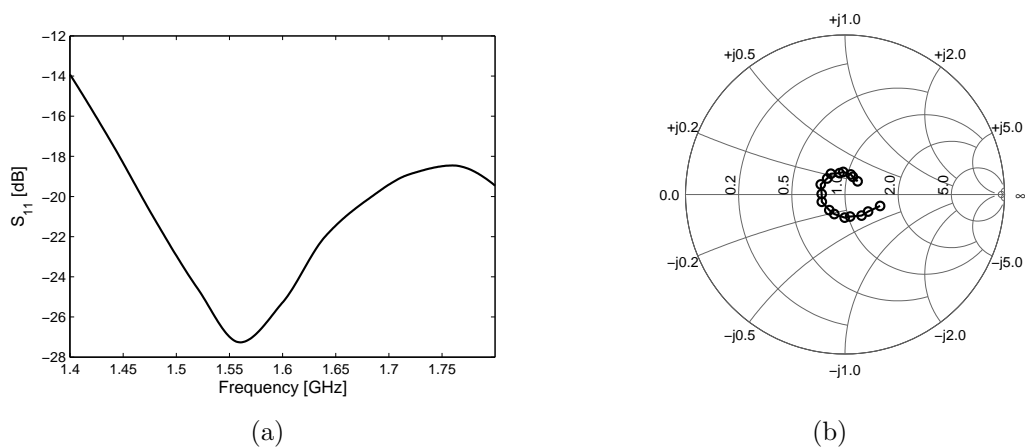


Figure 3.22: (a) Magnitude and (b) Smith chart plot of the input impedance reflection coefficient of the constructed antenna with microstrip feed network.

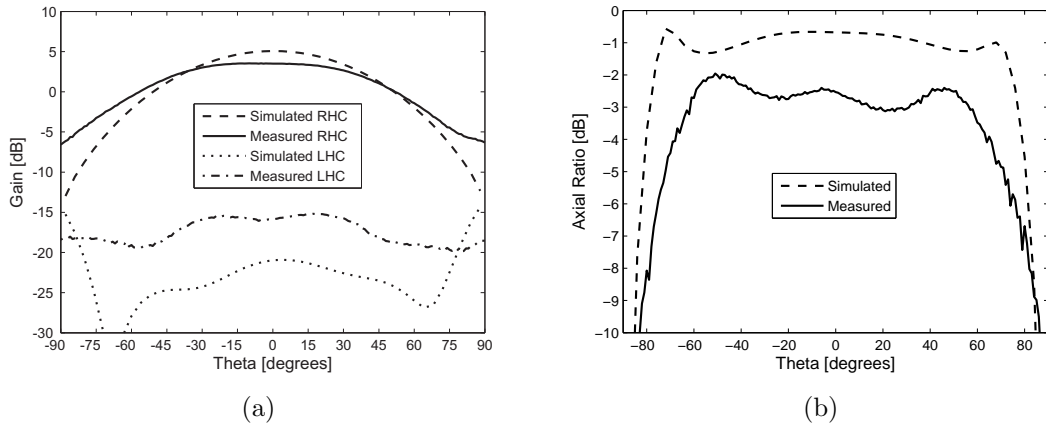


Figure 3.23: Measured and simulated (a) gain and (b) axial ratio of the $\lambda/2$ QHA prototype fed by the microstrip feed network ($f = 1.6 \text{ GHz}$).

3.7 Summary

To investigate the capabilities of the QHA as an element in wide angle scanning arrays, a top patch structure which improved low angle scanning in a previously studied array [1] was incorporated into the structure. For the $\lambda/2$ QHA this patch acted as a short for the ends of the helices, while the patch floated parasitically above the open ended $\lambda/4$ QHA. In an isolated environment this disk has the effect of making the radiation pattern very directional towards broadside with good axial ratio over most of the upper hemisphere. The size of the disk is the primary factor in determining the radiation characteristics, which makes it possible to design the QHA to have a low profile and still achieve good low angle circular polarization. This is not possible with the traditional QHAs investigated in Chapter 2.

A microstrip feed network providing the necessary power division and quadrature phasing is designed to feed a manufactured $\lambda/2$ QHA prototype. Good agreement is achieved between the measured and simulated results, with slight deviations attributed to construction imperfections.

Chapter 4 investigates the effects of the incorporated top disk on the radiation performance of the QHA elements within an array environment.

Chapter 4

Array Performance of the QHA Elements

4.1 Introduction

The main purpose of the connected and parasitic disks which were incorporated into the traditional $\lambda/2$ and $\lambda/4$ QHA structures in Chapter 3, is to improve radiation performance when these antennas are used as elements within an array. In particular, emphasis is placed on improving the ability to scan to low elevation angles with sufficient gain and good axial ratio. This chapter investigates and compares the array performance of the various QHAs without and with top patches of diverse form, size and spacing, and within different array configurations.

An overview of classic array multiplication theory and its relevance to steering an array to low elevation angles is given in Section 4.2. The perturbing effects of mutual coupling on the ideal case theory is also discussed, along with methods used to compensate for mutual coupling in arrays. By exciting only a single element while resistively terminating the others, the active single element pattern can be obtained. This pattern is related to the scattering parameters of the array and can be used to predict angles at which mutual coupling will severely degrade radiation performance. Section 4.3 describes the various array topologies used throughout the study. When evaluating the coupling between different QHA elements in an array it is desired to have discrete coupling coefficients between individual elements. To that end, the four port antenna is combined mathematically with the five port feed network of the previous chapter to obtain a one port array element. In Section 4.5 the aforementioned array topologies are used to compare the array characteristics of three different QHA elements: a tradi-

tional open-ended $\lambda/4$ QHA, a parasitically topped $\lambda/4$ QHA and a disk-shortened $\lambda/2$ QHA. The active single element pattern of the middle element of each array is shown and the magnitude of the coupling between the center element and other elements evaluated. Finally, the arrays are electronically phase steered from broadside to the horizon and the radiation performance compared.

Large computational resource requirements and lengthy simulation times become a hindrance when investigating the performance of relatively large array structures. To facilitate the study of the arrays, a Matlab program was developed which uses FEKO to simulate array structures and stores results for convenient subsequent examination and analysis. A graphical user interface allows the user to specify geometrical parameters which define the array configuration for which a FEKO model will be created automatically, as well as simulation parameters to be used when running the FEKO solver. This software is discussed and illustrated in detail in Appendix B.

4.2 Introducing Array Theory and Stating the Necessary Conditions for Low Elevation Angle Scanning

The total fields radiated by an array antenna is determined by the vector addition of the fields radiated by the individual elements within the array environment [15]. Increased directivity in a desired direction is achieved through constructive interference in that direction, and destructive interference in the remaining space. This can be accomplished by adjusting the dimensional arrangement of the elements, and the relative phasing of the element excitation.

4.2.1 Classic Array Pattern Multiplication without Mutual Coupling

When there is no coupling between the elements, the contribution of each element to the radiated far-field will be the same as that of an isolated element, displaced from a reference point. In this ideal case where the radiated pattern is determined by the vector addition of identical element patterns, the total field of the array can be written as the field of a single isolated element positioned at the origin multiplied by an array factor. This array factor is then a function of the geometry of the array as well as the excitation amplitude and phase.

Figure 4.1 shows an N element hexagonal array of arbitrary elements located in the $z = 0$ plane. The x - and y -coordinates of the m^{th} element is indicated in the figure as (x_m, y_m) . Assuming far-field observation and applying the usual approximations ([15] pp 250–251), the pattern radiated by the array can be written as

$$F_t(\theta, \phi) = F_e(\theta, \phi) \cdot AF(\theta, \phi) \quad (4.1)$$

where the pattern of the isolated element is $F_e(\theta, \phi)$. If A_m and β_m are respectively the relative amplitude and phase of the m^{th} element, the array factor is given by

$$AF(\theta, \phi) = \sum_{m=1}^N A_m \cdot e^{j[k(x_m \sin \theta \cos \phi + y_m \sin \theta \sin \phi) + \beta_m]} \quad (4.2)$$

In order to have a main beam directed along $\theta = \theta_0$ and $\phi = \phi_0$, the excitation phase shift for element m relative to the reference element at the origin must be

$$\beta_m = -k \sin \theta_0 (x_m \cos \phi_0 + y_m \sin \phi_0) \quad (4.3)$$

If the coordinates of each array element relative to the reference point is used when adding its contribution to the field as in 4.2, this array factor is valid for an arbitrary arrangement of elements.

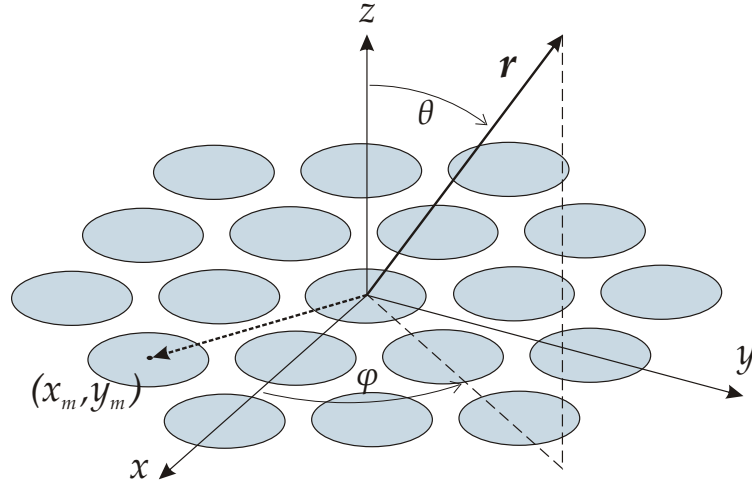


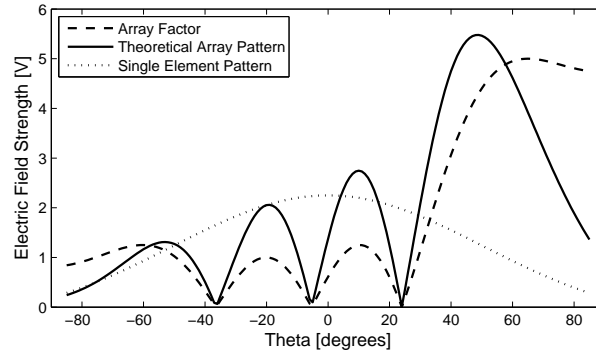
Figure 4.1: Array of N arbitrary radiating elements.

4.2.2 Pattern Multiplication Examples

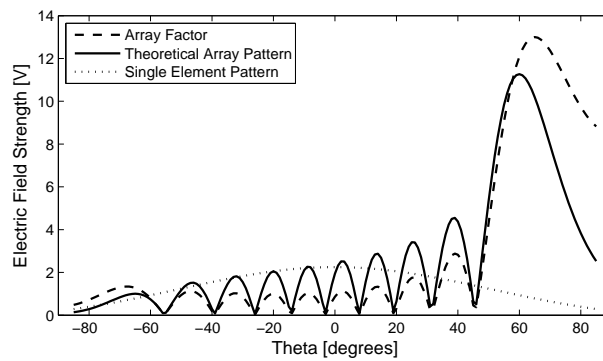
From (4.1) it is evident that in order for the array to radiate to a specific angle in space, the single element pattern must have a significant contribution at that

angle. If the main beam is to be steered to low elevation angles with acceptable circular polarization, the isolated element must have a very broad beam with a good axial ratio at low angles. This is generally difficult to achieve with low profile radiating elements and is further complicated by the presence of a large ground plane.

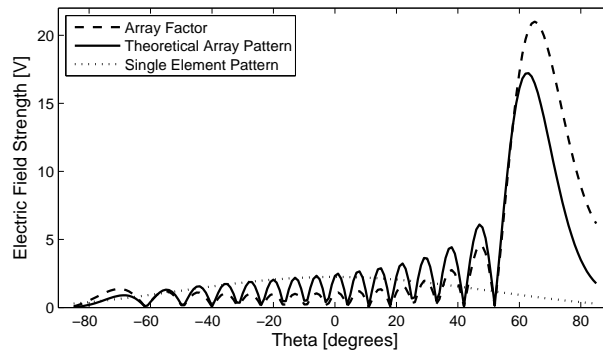
Figure 4.2 shows the calculated array factor and radiation pattern of a linear array with an increasing number of elements. The single element pattern used is that of the disk-shortened $\lambda/2$ QHA of Section 3.2.3. The array factor was calculated using (4.2), with $\theta_0 = 65^\circ$ and $\phi_0 = 0^\circ$ the angles to which the main beam is steered. In the first figure plotting the calculated array pattern of a 5 element array, the product of the array factor and the single element pattern has a maximum closer to $\theta = 45^\circ$ even though the relative phasing of the element was chosen to have an array factor maximum along $\theta = 65^\circ$. This is because the single element pattern is much more directive towards broadside than the horizon. As the number of elements increases, the array factor begins to dominate in (4.2) and the maximum of the radiated main beam moves closer to the desired angles for which the phasing was calculated. This illustrates the necessity of having elements that can radiate to low elevation angles within the array environment if the beam is to be steered over a wide angle. The effect of neighboring elements on the pattern of individual radiating element patterns is discussed further in Section 4.2.3.



(a) 5 Elements



(b) 13 Elements



(c) 21 Elements

Figure 4.2: Theoretically calculated elevation plane array radiation pattern for a linear array of varying number of elements. The disk-shortened $\lambda/2$ QHA of Section 3.2.3 is used as radiating element.

4.2.3 Practical Arrays with Mutual Coupling

While the classical array multiplication method described in Section 4.2.1 pertains only to the ideal case where no coupling is present, it does demonstrate the necessary conditions for an array to be able to scan to low elevation angles. In a practical array where there is coupling present between the elements, the pattern contribution of an individual element generally differs from the pattern of the same element in an isolated environment. This is illustrated by feeding only that element, and passively terminating the other elements. The pattern obtained in this case is called the active single element pattern. This pattern is different from the isolated element pattern because adjacent elements will also radiate some power due to mutual coupling induced currents on them [16]. This pattern has also been termed the scan element pattern [17].

In phase-steered arrays, additional issues arise which complicate the analysis and synthesis of the array and can be attributed to the effects of mutual coupling. The input impedance (or scan impedance) of the array elements varies with the angle to which the main beam is steered. This causes unequal power to be radiated by the elements as the reflection due to mismatch differs.

Scan Impedance and Scan Blindness

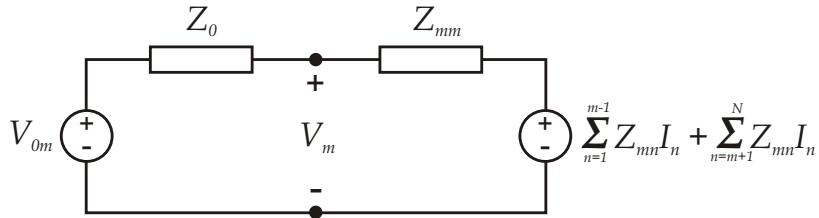


Figure 4.3: Equivalent circuit of radiating element number m with its feed within an N element array ([17]).

The equivalent circuit of the m^{th} element and its source within an N element array is shown in Figure 4.3. The total voltage at the antenna port will be

$$V_m = \sum_{n=1}^N Z_{mn} I_n \quad (4.4)$$

where Z_{mn} is the mutual impedance between elements m and n when $m \neq n$, and the self-impedance of element m when $m = n$. If V_{0m} is the voltage applied

to element m , the current can be calculated from

$$V_{0m} = Z_0 I_m + \sum_{n=1}^N Z_{mn} I_n \quad (4.5)$$

where Z_0 is the source impedance. This defines N linear equations with N unknowns I_1, I_2, \dots, I_N that can be solved for. The impedance of the m^{th} element within the array (scan impedance) is then

$$Z_{m\text{scan}} = \sum_{n=1}^N Z_{mn} \frac{I_n}{I_m} \quad (4.6)$$

This is called the scan impedance as it depends on the voltage applied to the elements, which in turn is determined by the desired angle to which the array is to be steered. In a finite array, the scan impedance will in general be different for each element. However, the impedances of the elements sufficiently removed from the edges of the array can for most purposes be approximated as equal.

As the scan impedance changes with scan angle, impedance mismatch and corresponding power loss will occur. Frequently one encounters a specific scan angle for an array at which the input impedance reflection coefficient is close to unity and no power can be radiated to that angle. This is known as scan blindness.

Active Single Element Pattern

As previously mentioned, the radiation pattern from an element within an array with all the other elements resistively terminated will in general be different from the pattern radiated by the same element in isolation. This is because adjacent elements radiate some power due to mutual coupling with the fed element. The active single element pattern is also dependent on the position within the array. If the array is large, however, most of the elements will see a uniform neighboring environment, and the pattern can be approximated as equal. The pattern of the fully excited array can then be expressed as the product of the array factor and the active element pattern.

It has also been shown that the realized gain of the fully excited array is proportional to the active element pattern at the same angle [16]. Therefore, if the measured active single element pattern has dips or nulls at a particular angle, this angle will represent a blind angle for the fully excited steered array.

The active element pattern can also be expressed in terms of the scattering

parameters of the array [18]. This relationship can be inverted to obtain the scattering parameters from the active element patterns. It is also possible to obtain the active input impedance of any element in the fully excited array, at any scan angle, from the active element pattern data.

Compensation of Mutual Coupling Effects

Different methods to compensate for the effects of mutual coupling in phased arrays have been proposed in literature. This is often done by modifying the excitation vector which represent the relative amplitude and phase of the signals applied to the array elements. The key to this technique is to recognize that a composite array pattern can be considered as the weighted sum of the isolated element patterns, and the effect of mutual coupling is to parasitically excite the neighboring elements. By driving the elements with modified excitations, such that the desired array aperture distribution is obtained in the presence of these parasitics, the mutual coupling effects can be compensated for. Mathematically this compensation consists of a matrix multiplication between a coupling matrix and the desired excitation vector to obtain a new excitation vector. The mutual coupling error can be compensated for at all angles simultaneously, making the correction scan independent. This technique has been demonstrated and experimentally verified [19, 20].

The design and analysis of linear, asymmetrical beam-forming networks which connects a large set of radiating elements to a much smaller set amplitude- and phase-controlled microwave sources is presented in [21]. In theory, this network is simultaneously impedance-matched for all angles at both the antenna and source interfaces.

Compensation methods based on the active single element pattern have also been introduced [22, 23]. In these methods unique active element patterns are measured for each element or groups of elements, and used in calculations predicting array performance.

These methods for mutual coupling compensation aim to cancel the steering-dependent impedance mismatch and ensure that the correct source aperture distribution is provided for all scan angles. The scan blindness effect will then also be suppressed. The focus of this thesis is on examining the ability to achieve low elevation angle beam steering with good axial ratio, and not to obtain a good impedance match at all scan angles. The compensation of mutual coupling is thus beyond the scope of this study and recommended for future work.

4.3 Description of Array Geometries Used

Throughout this study several element arrangements are used in arraying the antenna elements, of which the ones most frequently used are discussed in this section. The numbering convention which is used in all subsequent references to specific array elements is also indicated. In all of the following geometries the first element is located at the origin of the cartesian coordinate system.

4.3.1 Linear Array

The simplest array geometry is the linear arrangement of Figure 4.4. A one dimensional array is formed which is electronically steerable in the elevation plane only. The element numbering is straightforward and is indicated in the illustration.

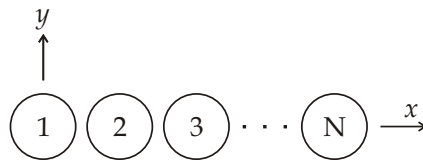


Figure 4.4: Linear array arrangement.

With d being the spacing between adjacent elements, the coordinates of element m is

$$x_m = (m - 1)d$$

$$y_m = 0$$

4.3.2 Rectangular Array

Figure 4.5 illustrates the rectangular arrangement used, consisting of an N element array with n rows and n columns. The elements are numbered sequentially along each row, and then along the columns. If d is the distance between elements, the x - and y -coordinates of the m^{th} element is given by

$$x_m = d[(m - 1) \text{MOD } n] \quad (4.7)$$

$$y_m = d[(m - 1) \text{DIV } n] \quad (4.8)$$

This two dimensional array can be steered in both the elevation and azimuth planes.

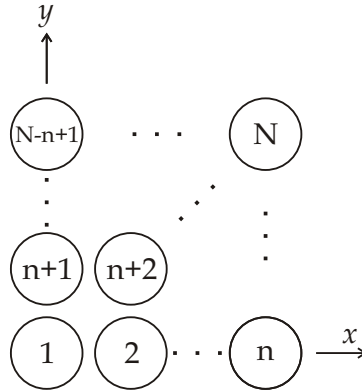


Figure 4.5: Rectangular array arrangement.

4.3.3 Hexagonal Array

The hexagonal arrangement shown in Figure 4.6 enables the elements of the array to be placed closer together than in the rectangular array. While being fundamentally spaced on an equilateral triangular grid, the planar hexagonal array offers a good approximation of a circular array which allows for uniform steering of the beam in the azimuth plane. The numbering of the elements is organized by grouping the elements of the array into M levels which consists of concentric hexagonal rings (Figure 4.6a). Elements are numbered sequentially from the inner levels outwards, and counter-clockwise from the element located on the positive x -axis for each level (Figure 4.6b). The number of elements in a complete hexagonal ring is $6m$ where m is the level indicated in the figure and $m > 0$. The total number of elements for an M -level hexagonal array is thus

$$N = 1 + \sum_{m=1}^M 6m, \quad m > 0 \quad (4.9)$$

A detailed formulation of the coordinates for each element within the hexagonal array is included in Appendix C.

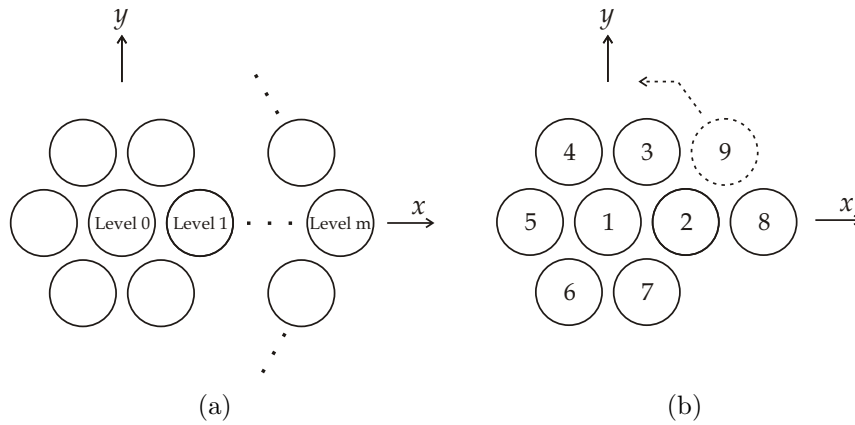


Figure 4.6: Hexagonal array arrangement.

4.4 Combining the Antenna and Feed Network

In the FEKO simulations of the antenna arrays consisting of QHA elements, a quadrature feed network is not included for each element. This is done to simplify the simulation model and save computational resources, as well as to prevent the feed network from influencing the investigation into array performance. Each helical element is fed explicitly with the required amplitude and phasing. The resulting scattering matrix exported from FEKO is $4N \times 4N$ in size, where N is the number of QHA elements of which the array consists. This makes it difficult to quantify the coupling between discrete QHAs as the elements in the scattering matrix only contain information on the interaction between individual helical elements.

In order to obtain a single port representation of each QHA, the 5-port feed network designed using Microwave Office is connected mathematically to the $4N$ -port antenna array simulated in FEKO. Before this can be done, the $4N$ -port antenna parameters needs to be converted to $5N$ -port parameters by adding a dummy port, which has an infinite input impedance and is completely isolated from the other ports, to every QHA. The isolation property of the additional ports is included in the antenna S-parameters by adding a row of zeros before every 4^{th} row and a column of zeros before every 4^{th} column. Because of the infinite input impedance of the added ports, elements $5(m-1) + 1$, with $m = 1, 2 \dots N$, of the diagonal are $1 \angle 0$. This process is described in (4.10) and (4.11).

$$[S_{4N \times 4N}] = \begin{bmatrix} S_{11} & S_{12} & \cdots & S_{1N} \\ S_{21} & S_{22} & & \\ \vdots & & \ddots & \vdots \\ S_{N1} & & \cdots & S_{NN} \end{bmatrix} \quad (4.10)$$

⇓

$$[S_{5N \times 5N}] = \begin{bmatrix} 1 \angle 0 & 0 & 0 & 0 & 0 & \cdots \\ 0 & S_{11} & S_{12} & S_{13} & S_{14} & \\ 0 & S_{21} & S_{22} & S_{23} & S_{24} & \\ 0 & S_{31} & S_{32} & S_{33} & S_{34} & \\ 0 & S_{41} & S_{42} & S_{43} & S_{44} & \\ \vdots & & & & & \ddots \end{bmatrix} \quad (4.11)$$

A $5N \times 5N$ feed network scattering matrix is created by repeating the original block of 5×5 feed network parameters vertically and horizontally. The modified feed and antenna scattering matrices are converted to admittance matrices (Y-parameters) and corresponding matrix elements added together to make a parallel connection between the two networks. This connection is illustrated in Figure 4.7.

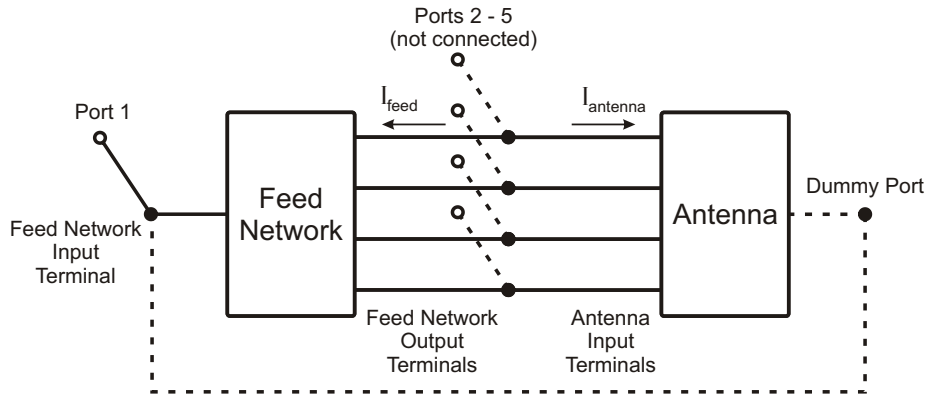


Figure 4.7: A diagram representing the parallel connection between the 4-port antenna and 5-port feed network.

The admittance matrix $[Y]$ is defined as

$$\begin{bmatrix} I_1 \\ I_2 \\ \vdots \\ I_M \end{bmatrix} = \begin{bmatrix} Y_{11} & Y_{12} & \cdots & Y_{1M} \\ Y_{21} & & & \\ \vdots & \ddots & & \vdots \\ Y_{M1} & \cdots & Y_{MM} & \end{bmatrix} \begin{bmatrix} V_1 \\ V_2 \\ \vdots \\ V_M \end{bmatrix} \quad (4.12)$$

where I_i and V_i are the total voltage and current at the i^{th} terminal, and $M = 5N$. As only port 1 of the mathematically combined network is an actual physical port (input/output of the feed network), the currents at the other ports are zero ($I_{feed(2..5)} = -I_{antenna(2..5)}$). Thus only the currents I_k with $k = 5(n-1) + 1$, $n = 1, 2..N$ are non-zero. The Y-parameters are then converted to Z-parameters which is defined as

$$\begin{bmatrix} V_1 \\ V_2 \\ \vdots \\ V_M \end{bmatrix} = \begin{bmatrix} Z_{11} & Z_{12} & \cdots & Z_{1M} \\ Z_{21} & & & \\ \vdots & \ddots & & \vdots \\ Z_{M1} & \cdots & Z_{MM} & \end{bmatrix} \begin{bmatrix} I_1 \\ I_2 \\ \vdots \\ I_M \end{bmatrix} \quad (4.13)$$

Elements corresponding to $Z_{ij} = \frac{V_i}{I_j}$, where $(i-1)$ and $(j-1)$ are multiples of 5, are selected to form a reduced $N \times N$ impedance matrix.

$$[Z_{M \times M}] = \begin{bmatrix} Z_{11} & Z_{12} & \cdots & Z_{1M} \\ Z_{21} & & & \\ \vdots & \ddots & & \vdots \\ Z_{M1} & \cdots & Z_{MM} & \end{bmatrix} \quad (4.14)$$

$$\Downarrow$$

$$[Z_{N \times N}] = \begin{bmatrix} Z_{11} & Z_{16} & \cdots & Z_{1(M-4)} \\ Z_{61} & & & \\ \vdots & \ddots & & \vdots \\ Z_{(M-4)1} & \cdots & Z_{(M-4)(M-4)} & \end{bmatrix} \quad (4.15)$$

This impedance matrix can now be converted back to an $N \times N$ scattering matrix of which the elements describe the interaction between the individual QHA elements of the array. By reducing the scattering matrix in this fashion it is assumed that when the feed network is included in the array it will have negligible contribution to the coupling between elements.

4.5 Comparing Array Characteristics of Different QHA Elements

This section presents a comparison between the radiation and coupling characteristics of different QHA elements when operating within an array environment. These include the two top-disk elements of Chapter 3, as well as a normal $\lambda/4$ QHA element without any parasitic disk. In arranging the elements, the three topologies discussed in Section 4.3 are used. Emphasis is placed on the level of coupling between elements, as well as the influence of the neighboring environment on the active single element pattern. When evaluating the coupling between elements, the reduced scattering matrix which was constructed mathematically by combining the designed feed network with the radiating element (Section 4.4), is considered. The ability of the arrays to be steered to low elevation angles with sufficient gain and good axial ratio is also examined briefly. Throughout this section an inter element spacing of 72 mm is used which creates tightly packed arrays for both the parasitically topped $\lambda/4$ elements as well as the disk-shortened $\lambda/2$ elements. The same spacing is used for the $\lambda/4$ elements without top disks. Investigation into the impedance variations of the different arrays when scanned to different angles was not done and is recommended for further studies.

The Matlab software developed for studying arrays is used extensively throughout this section. A lot of time and effort is saved as the creation of the simulation models is completely automated and the results are saved for examination afterward. The desired geometrical and excitation parameters are entered or selected from drop-down menus and used in the setup of the simulation project. Specifying the excitation coefficients for steering the main beam is simplified to a great extent, as only the desired values of θ_0 and ϕ_0 to which the beam is to be steered needs to be selected. The program then uses the already defined array geometry to calculate the required phasing for all four ports of each QHA element, and incorporates it into the creation of the FEKO simulation model. Appendix B gives a detailed explanation of the software.

4.5.1 Linear Array

Active Single Element Pattern

Figure 4.8 shows the 3D simulated radiation patterns of 25 element linear arrays comprised of the three elements mentioned in the introduction. Only the center element is fed, with the other elements passively terminated in the system characteristic impedance. The resulting plots show the differences in the active single element patterns of the middle element with different element types used. An elevation plane cut with $\phi = 0^\circ$ compares the patterns of the different elements in Figure 4.9. It is seen that the pattern of the $\lambda/4$ QHA with parasitic disk is drawn more towards the neighboring elements than the other two.

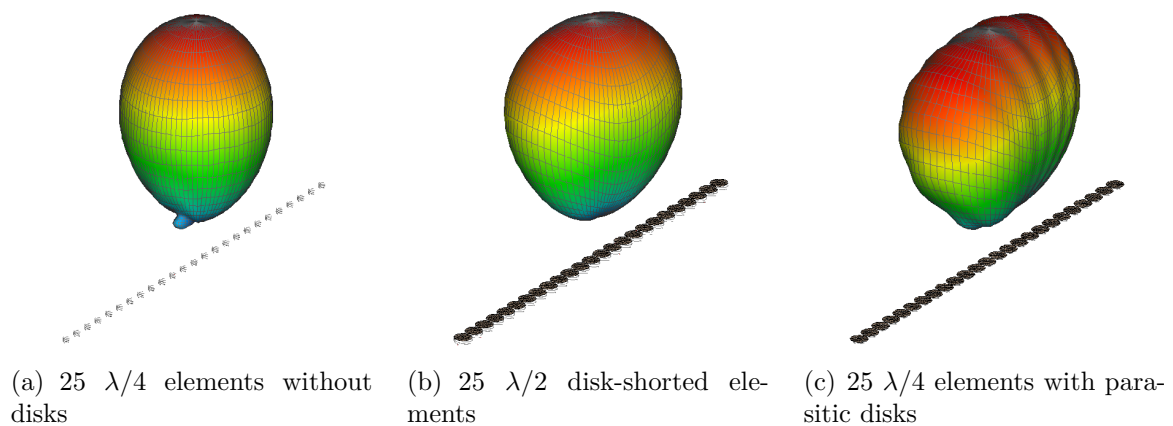


Figure 4.8: RHC polarized component of the far-field radiation pattern with only the center element fed.

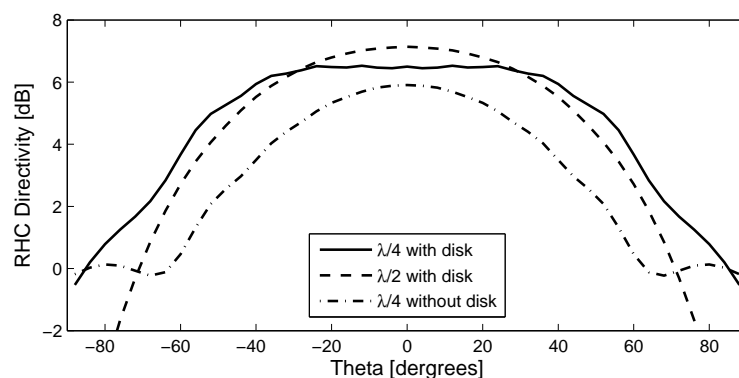


Figure 4.9: Comparison of the middle element active element pattern of a 25 element linear array comprised of different radiating elements. $\phi = 0^\circ$.

Coupling

In Figure 4.10, the coupling coefficients between the different array elements and the center element (number 13) is plotted vs. the element number. In this linear array, the difference between the element numbers is directly proportional to the element separation, so the scaling of the horizontal axis can also be viewed as the distance along the x -axis.

For the topless $\lambda/4$ and disk-shortened $\lambda/2$ elements, the level of coupling diminishes quickly for elements that are positioned a greater distance from the reference element. However, a comparatively sustained level of coupling is noticed for the linear array of $\lambda/4$ QHA elements with parasitic top disks positioned above them.

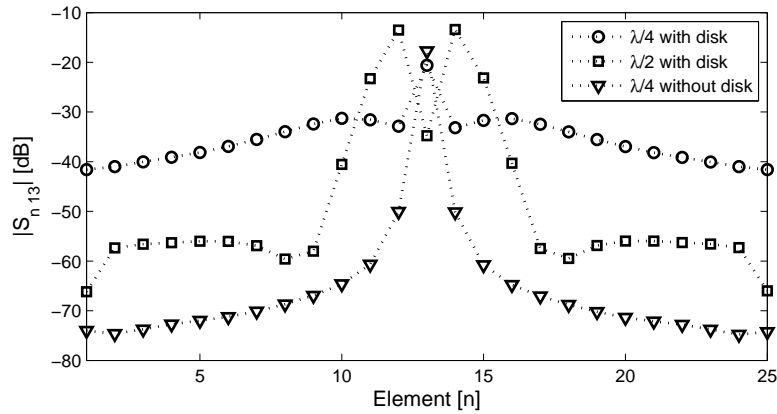


Figure 4.10: Coupling coefficients between the elements of the linear arrays.

Scanning

In Section 4.2.1 it is shown that in order for an array to be steered effectively to low elevation angles, the individual radiating elements within the array environment must have a significant contribution at those angles. Figure 4.11 plots the RHC component of the far-field patterns as well as the axial ratio sampled at the angles used for calculating the phasing when the main beam is steered from $\theta_0 = 0^\circ$ to $\theta_0 = 80^\circ$. As is the case in Section 4.2.2, this is not necessarily the maximum of the resulting radiation pattern. The $\lambda/4$ disk-topped array has a slightly larger field component closer to the horizon. It also has a superior axial ratio, especially between $\theta_0 = 30^\circ$ and $\theta_0 = 70^\circ$.

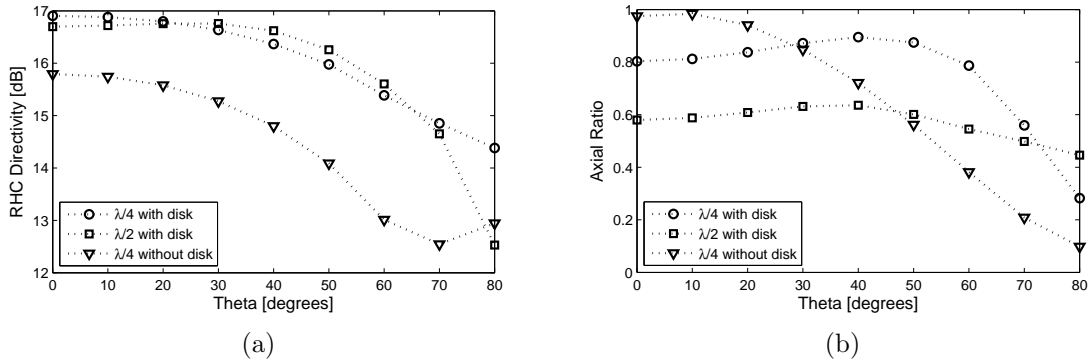
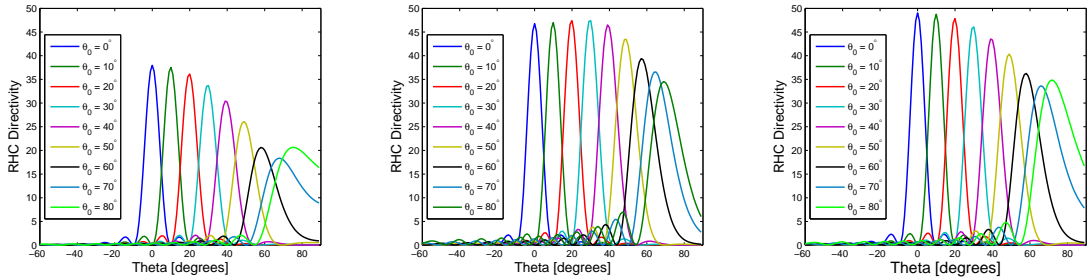


Figure 4.11: (a) Co-polarized component of the far-field radiation pattern, and (b) Axial ratio on the linear arrays at the specified angles to which beam steering is attempted.



(a) 15 $\lambda/4$ elements without disks (b) 15 $\lambda/2$ disk-shortened elements (c) 15 $\lambda/4$ elements with parasitic disks

Figure 4.12: Resulting radiation pattern of the linear arrays with the element phasing calculated to have an array factor maximum at θ_0 and ϕ_0 . The values of θ_0 are indicated in the figures, and $\phi_0 = 0^\circ$.

4.5.2 Rectangular Array

Active Single Element Pattern

With only the center element fed, the resulting radiation patterns of the three different 49 element rectangular arrays show some similarities to those of the linear arrays. The pattern of the disk-topped $\lambda/4$ element array forms a cone-shaped beam with a maximum at about $\theta = 25^\circ$. It also has an overall greater directivity at low elevation angles than the arrays of the other two elements.

Coupling

Figure 4.15a plots the coupling coefficients between elements located on the array diagonal, as indicated in 4.15b. This also makes the scale of the horizontal axis proportional to the separation distance between the elements. The topless $\lambda/4$

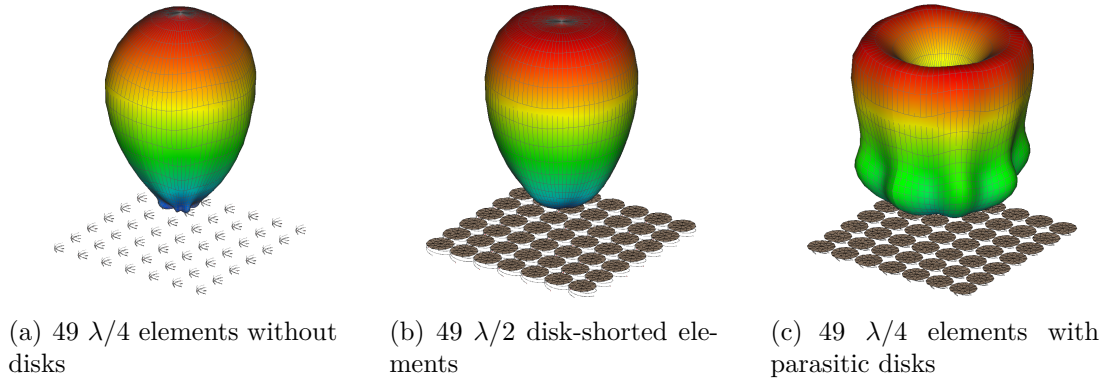


Figure 4.13: RHC polarized component of the far-field radiation pattern of the rectangular arrays with only the center element fed.

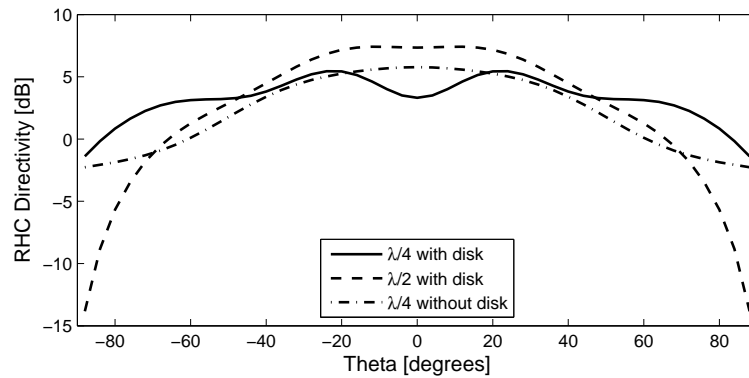


Figure 4.14: Comparison of the middle element active element pattern of a 49 element rectangular arrays comprised of different QHA elements. $\phi = 0^\circ$.

QHA array exhibits a very rapid drop in coupling as the distance increases. With the top disk $\lambda/4$ QHA array, and to a much lesser extent the $\lambda/2$ QHA array, the sustained level of coupling is again noticed.

Scanning

In Figure 4.16, the radiation patterns of the three different 49 element rectangular arrays are shown with scan angles $\theta_0 = 0^\circ$ to $\theta_0 = 80^\circ$, and $\phi_0 = 0^\circ$. As is illustrated in Figure 4.16, the $\lambda/4$ QHAs with top hats again have a slightly larger co-polarized directivity component at the low elevation angles to which scanning is attempted. The axial ratio of the array comprised of these elements is also superior over most of the hemisphere. The larger axial ratio of the $\lambda/2$ elements at $\theta = 80^\circ$ in Figure 4.16b is misleading, as the field component compared to the other elements at this angle is much smaller (Figure 4.16a). Figure 4.17 shows that the beams of the topped $\lambda/4$ QHA arrays is steered more accurately to the

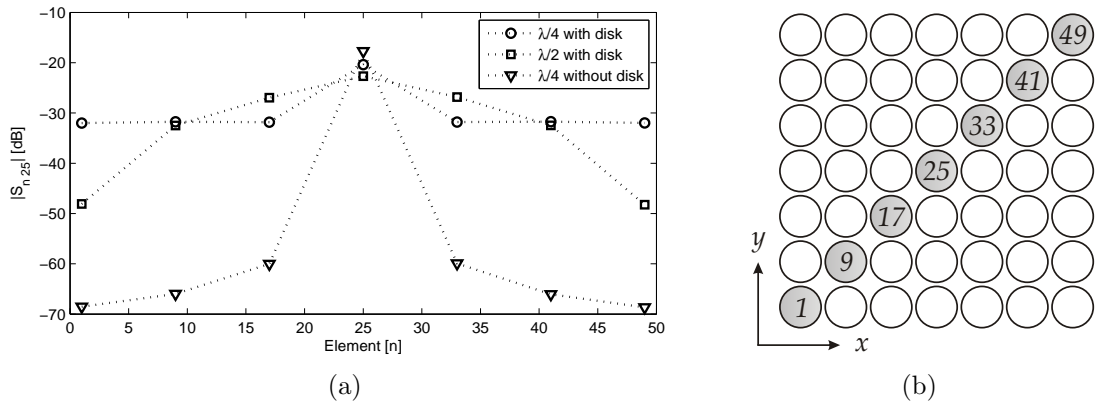


Figure 4.15: Coupling coefficients between the diagonal elements of the rectangular arrays.

desired θ value than the other two arrays.

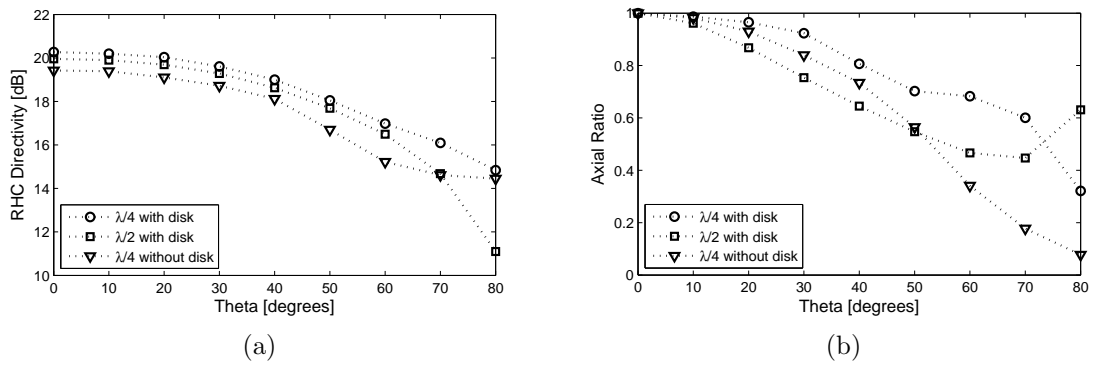
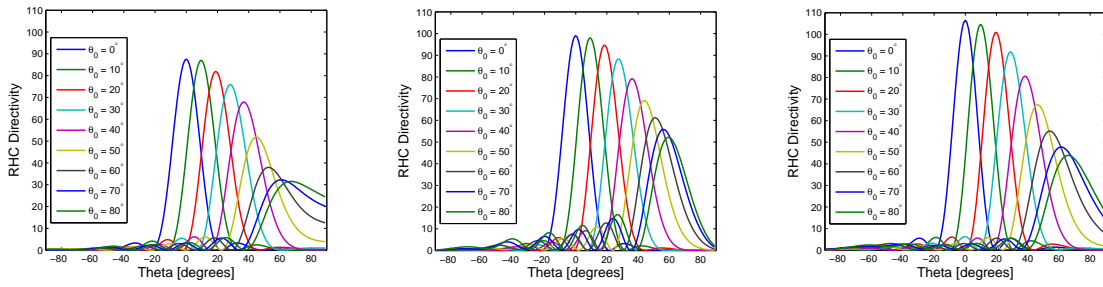


Figure 4.16: (a) Co-polarized component of the far-field radiation pattern, and (b) Axial ratio of the rectangular arrays at the specified angles to which beam steering is attempted.



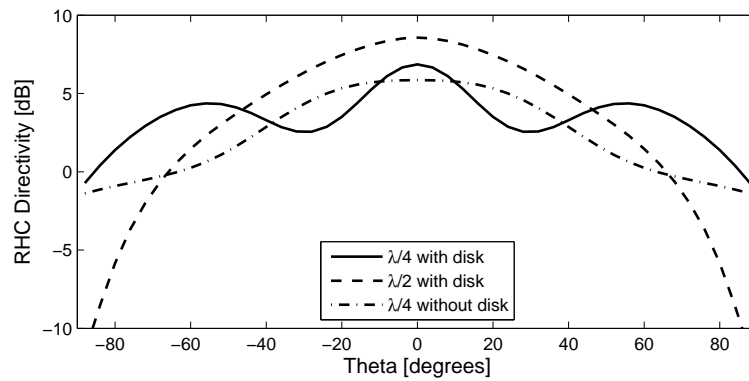
(a) 49 $\lambda/4$ elements without parasitic disks (b) 49 $\lambda/2$ disk-shortened elements (c) 49 $\lambda/4$ elements with parasitic disks

Figure 4.17: Resulting radiation pattern of the rectangular arrays with the element phasing calculated to have an array factor maximum at θ_0 and ϕ_0 . The values of θ_0 are indicated in the figures, and $\phi_0 = 0^\circ$.

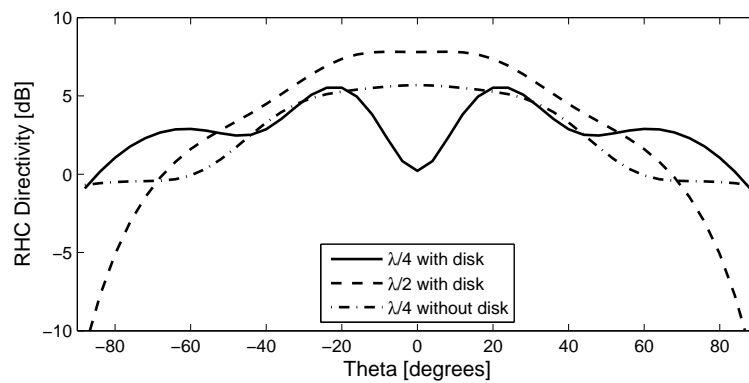
4.5.3 Hexagonal Array

Active Single Element Pattern

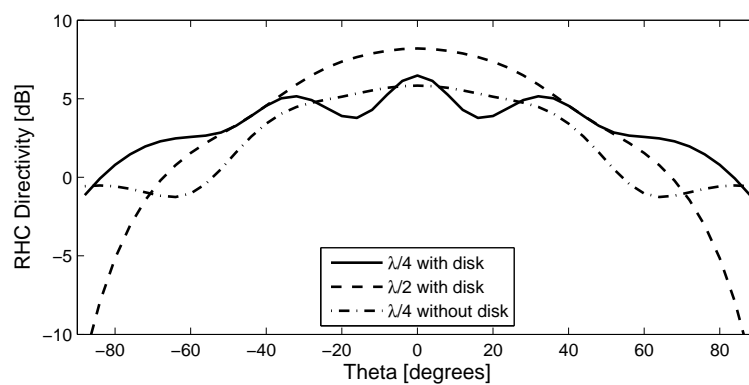
The co-polarized component of the radiation patterns of hexagonal arrays with varying number of elements, and only the center element fed, is plotted in Figure 4.18. The same three elements is used to assemble the arrays as for the previously examined linear and rectangular arrays. For all three array sizes, the $\lambda/4$ QHA with top disk has greater directivity towards low angles. The 61 element array composed of these elements has a conical radiation pattern which exhibits a sharp dip towards broadside. Not shown is the active single element pattern of the center element of a 19 elements array which also displays this behaviour.



(a) 37 Elements



(b) 61 Elements



(c) 91 Elements

Figure 4.18: Comparison of the middle element active element pattern of 37, 61 and 91 element hexagonal arrays comprised of different QHA elements. $\phi = 0^\circ$.

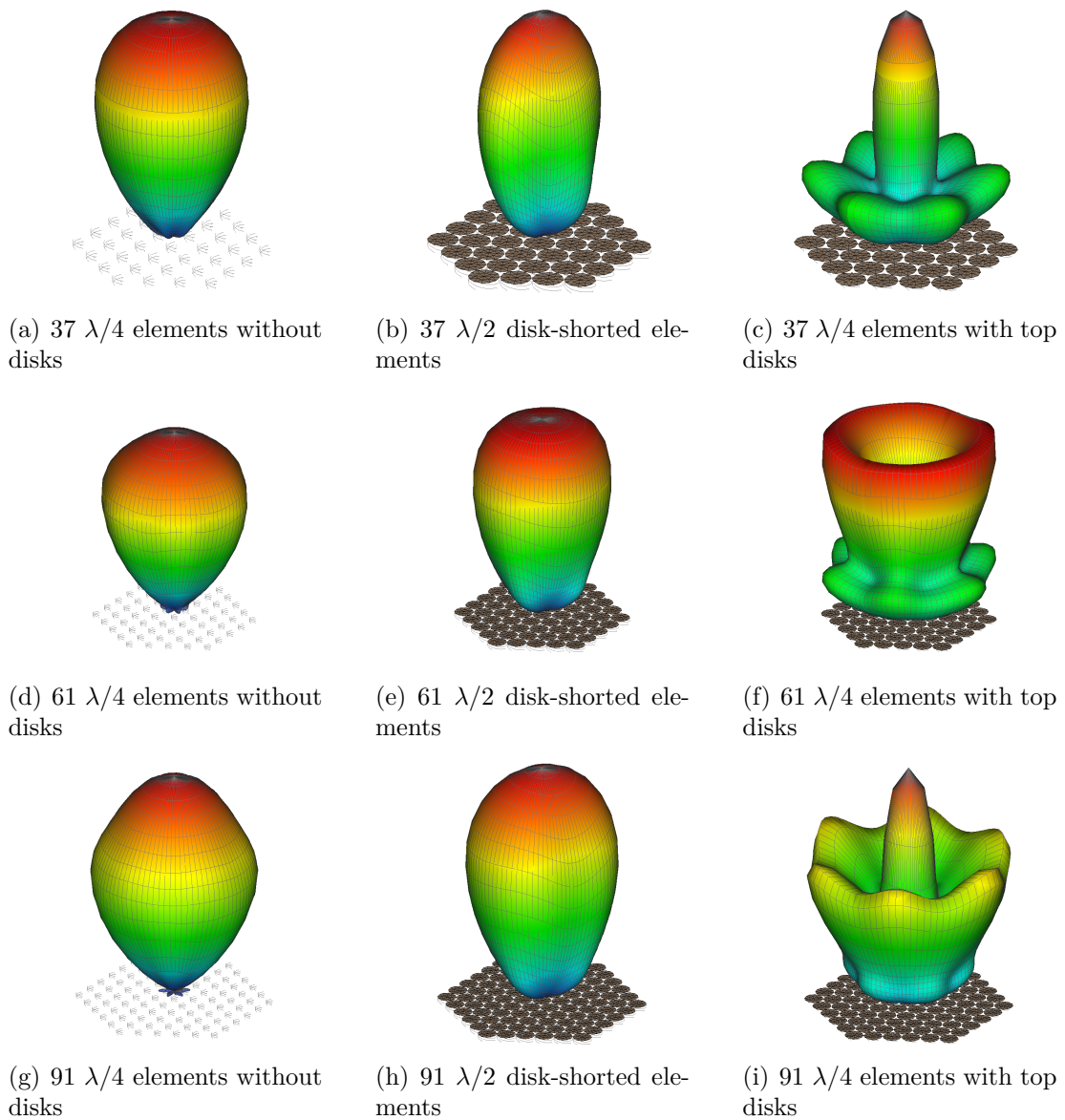


Figure 4.19: RHC polarized component of the far-field radiation pattern of the various hexagonal arrays with only the center element fed.

Coupling

As the various layers of the hexagonal array arrangement discussed in Section 4.3 has the same separation between the center element and the elements within the particular array, it is sensible to calculate the average coupling between them. This is shown in Figure 4.20. Again the coupling between normal $\lambda/4$ QHAs drops off rapidly as the separation between them increases. For layers 1 and 2, the disk-shortened $\lambda/2$ elements have the strongest coupling. From layer 3 outward, the $\lambda/4$ QHAs with parasitic disks again display the sustained coupling level which is greater than that of the other elements. Although this is only illustrated for a 91 element array, the same coupling properties is observed for hexagonal arrays with different numbers of elements.

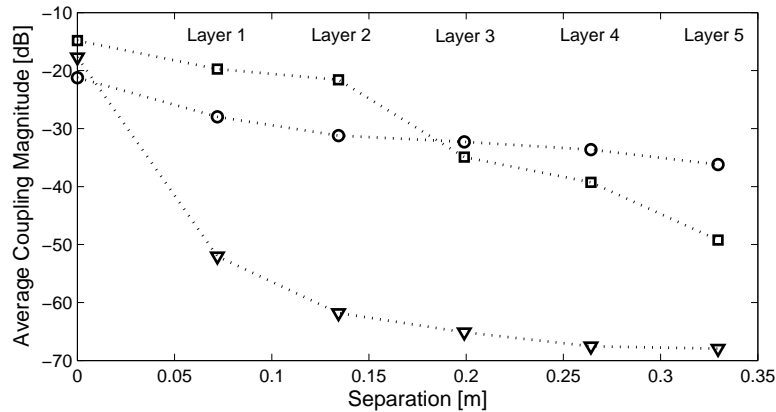


Figure 4.20: Average of the coupling coefficient magnitude between the center element and concentric layers of elements of 91 element hexagonal arrays.

Scanning

Again, the $\lambda/4$ elements with and without top disks, as well as the disk-shortened $\lambda/2$ elements are used in an array of which the main beam is steered. Both the 61 and 91 element arrays (5 and 6 concentric hexagonal rings respectively) are considered. With the attempted scan angles the same as for the linear and rectangular arrays of the previous sections ($\theta_0 = 0^\circ..80^\circ$; $\phi_0 = 0^\circ$), the resulting right hand circularly polarized directivity components sampled at those angles are plotted in Figure 4.21a. As is the case for the linear and rectangular arrays, the $\lambda/4$ elements with top disks has a slightly larger component towards lower elevation angles. At $\theta = 80^\circ$, the topless $\lambda/4$ elements seems to have the largest field component. Inspection of Figure 4.21b which plots the axial ratio sampled

at the scan angles, reveals that the main beam for that array is no longer circularly polarized but has a polarization which is very close to linear. Only the E_θ component remains, while the E_ϕ component which is tangential to the infinite ground plane at $z = 0$ vanishes. For the $\lambda/4$ components with parasitic disks a good axial ratio is achieved over the entire hemisphere, even though the infinite ground plane does inhibit a circularly polarized beam to steered close to the horizon. In Chapter 6, a finite ground plane is introduced to the structure.

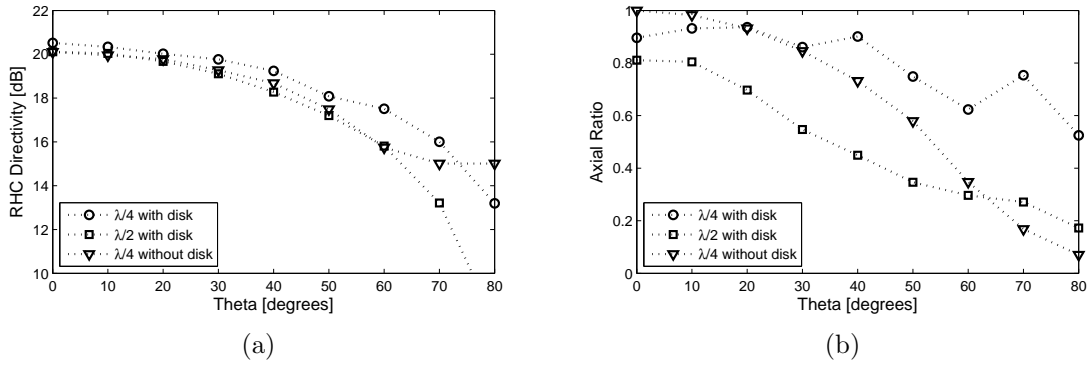


Figure 4.21: (a) Co-polarized component of the far-field radiation pattern, and (b) Axial ratio of the 61 element hexagonal at the specified angles to which beam steering is attempted.

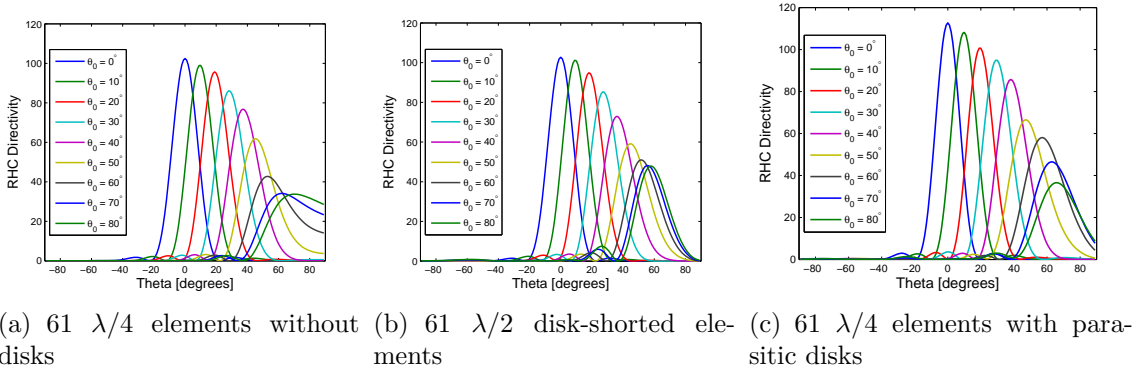


Figure 4.22: Resulting radiation pattern of the 61 element hexagonal arrays with the element phasing calculated to have an array factor maximum at θ_0 and ϕ_0 . The values of θ_0 are indicated in the figures, and $\phi_0 = 0^\circ$.

The results of steering the 91 element arrays are much the same as that of the 61 elements arrays, and is shown in Figure 4.23.

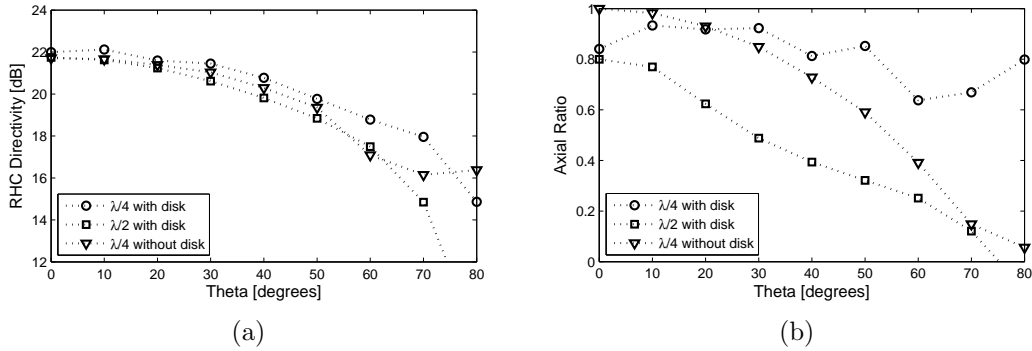


Figure 4.23: (a) Co-polarized component of the far-field radiation pattern, and (b) Axial ratio of the 91 element hexagonal at the specified angles to which beam steering is attempted.

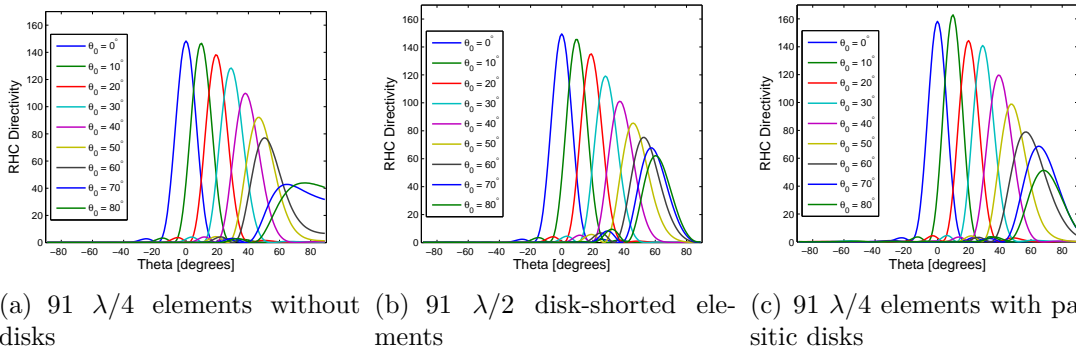


Figure 4.24: Resulting radiation pattern of the 91 element hexagonal arrays with the element phasing calculated to have an array factor maximum at θ_0 and ϕ_0 . The values of θ_0 are indicated in the figures, and $\phi_0 = 0^\circ$.

4.6 Summary

In order for an array to be able to radiate sufficiently to low elevation angles, the elements within the array must have a significant contribution to those angles. Mutual coupling between elements within the array environment has the effect of parasitically exciting the neighboring elements which contribute to giving a radiation pattern which differs from that of the same element in isolation. This is particularly noticeable for the parasitically topped $\lambda/4$ QHA elements positioned within a tightly packed array. Strong coupling between elements is exhibited, that does not weaken much for elements that is separated by a greater distance. When the center element of these arrays are excited, the element pattern is drawn towards the horizon and the neighboring elements and results in a pattern that is much wider than the isolated element pattern of Section 3.3.3. Consequently, it is possible to achieve better circularly polarized low elevation radiation with these

arrays, as the elements within the array has an effective wide angle radiation pattern.

The sustained coupling level away from the fed element, together with the conical active single element patterns with maxima away from broadside, hints at a type of traveling mode being supported by the parasitically topped $\lambda/4$ QHA arrays. In particular, fast waves (or leaky waves) exhibits much the same characteristics and is investigated further in the next chapter.

Chapter 5

Leaky Wave Antennas

5.1 Introduction

As is mentioned in the previous chapter, the sustained coupling and conical radiation pattern of disk-topped $\lambda/4$ QHA arrays suggests a traveling mode supported by the structure. In the design of an existing satellite-tracking phased array consisting of cavity-backed crossed slot antennas with parasitic top disks [1], similar behaviour was observed and traveling mode operation suspected. This chapter investigates leaky wave radiation and its relation to previous QHA array studies.

Section 5.2 outlines the properties and characteristics of leaky wave antennas. This includes the nature of the supported modes as well as the typical radiation properties. A comparative study between leaky (fast) wave and surface waves is also presented. To link the previous work done on parasitically loaded QHA antennas with leaky wave radiation, an antenna consisting of a single $\lambda/4$ QHA element beneath a 91 element hexagonal patch configuration was constructed and measured. Details of the antenna as well as simulated and measured results is given in Section 5.4.3.

5.2 Properties and Characteristics

Leaky-wave antennas (LWAs) belong to the traveling-wave antenna family where radiation occurs from a supported traveling mode. [15] gives an encapsulating definition as “an antenna that couples power in small increments per unit length, either continuously or discretely, from a traveling wave structure to free space”. In general, these antennas consist of some structure which is capable of guiding the leaky wave, and a source, usually simple in nature, which launches a wave that propagates transversely with a complex propagation constant $k_t = \beta + j\alpha$

[24]. A prime characteristic of a leaky wave is that $\beta < k_0$, where k_0 is the free space wavenumber. This means that the wave has a phase velocity greater than that of light, and may radiate at a specified angle into space, depending on β . For this reason it is also frequently termed a fast wave. The attenuation constant α is related to the rate of leakage as the wave propagates along the guiding structure. Smaller values of α result in larger effective radiating apertures, and hence narrower beams.

An additional property of leaky waves is that they are “improper” (or non-modal), having a field variation that increases exponentially away from the guiding surface. A detailed discussion of this characteristic is provided in Section 5.2.1.

Geometrically, LWAs can be grouped into two main categories: uniform and periodic. From the nature of the traveling wave, they can further be classified into one-dimensional (1-D) and two-dimensional (2-D) LWAs. A uniform LWA consists of a uniform guiding structure which supports a leaky wave propagating either in a fixed direction (1-D) or radially along a planar surface (2-D). Examples include a rectangular waveguide with a longitudinal slit in the wall (1-D) [25] and a single or multiple-layer dielectric structure excited by a dipole source (2-D) [24].

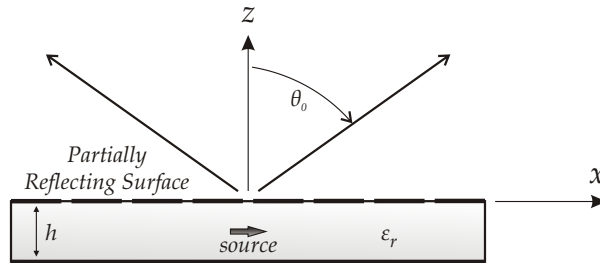
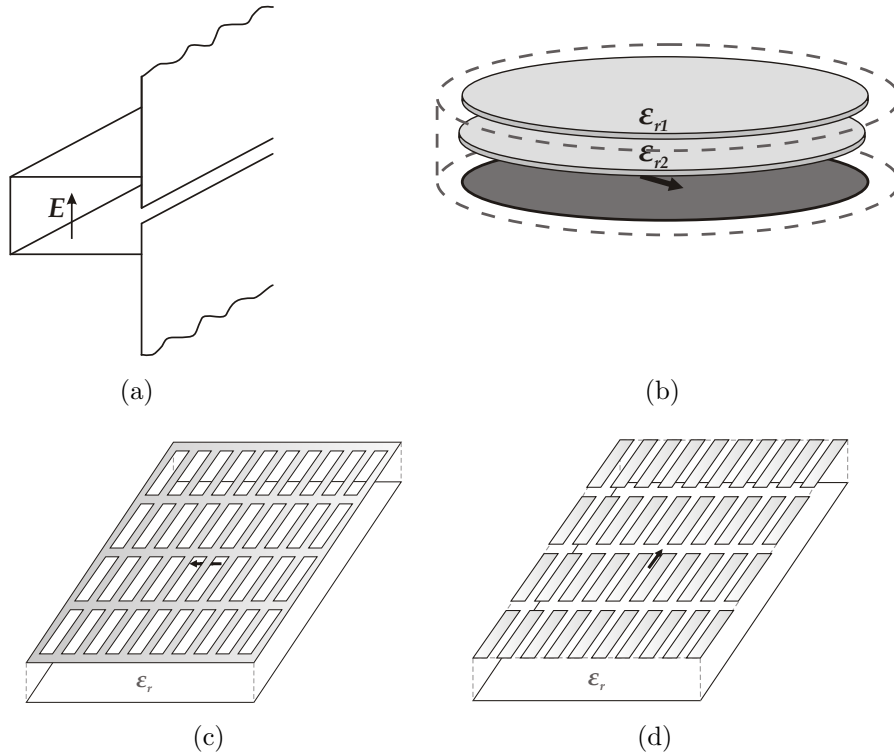


Figure 5.1: A general periodic LWA consisting of a PRS mounted on a grounded dielectric substrate.

Periodic LWAs generally consists of a partially reflecting surface (PRS) mounted on top of a grounded dielectric substrate, as shown in Figure 5.1. In previous studies of periodic LWAs, the PRS consisted of a 2-D periodic arrangement of metal patches or slots [26, 27]. The source shown in Figure 5.1 is a simple horizontal dipole located within the substrate but can be virtually any type of source, as the pattern mainly depends on the LWA structure and not the source. The leaky wave propagates outward radially along the guiding structure from the point of excitation, and radiates at an angle θ_0 .



Examples of previously studied leaky-wave structures. (a) Rectangular waveguide with longitudinal slit [25]. (b) Stacked arrangement of dielectric layers with absorbing material at the edge [28]. (c) Metal slot and (d) patch PRS mounted on a grounded dielectric substrate [27, 26].

5.2.1 The Non-Modal Nature of Leaky Waves.

Previously it was mentioned that leaky waves are not proper modes as they have a field variation which increases exponentially away from the guiding structure. In this section it will be shown that within certain restricted regions within which they remain finite, the leaky-wave solutions are valid field representations.

Figure 5.2 shows a semi-infinite uniform leaky waveguide, fed by a closed waveguide. The wave propagates along the structure in the positive x -direction with a phase velocity greater than the speed of light, and an attenuation constant which is indicative of continued leakage of energy along the length of the guide.

The free space wavenumber k is related to the wavenumbers in the x, y and z directions by

$$k^2 = k_x^2 + k_y^2 + k_z^2 = \left(\frac{2\pi}{\lambda}\right)^2 \quad (5.1)$$

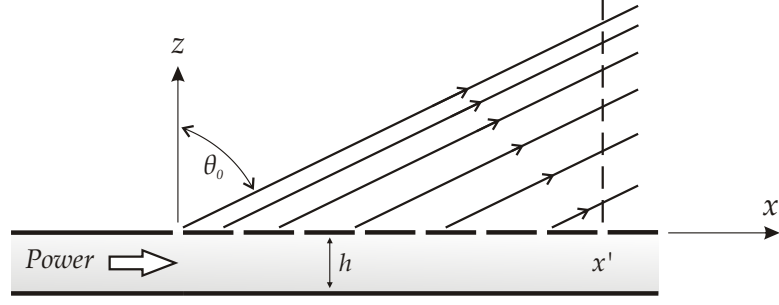


Figure 5.2: Radiation from a semi-infinite leaky waveguide [25].

If the leaky wave propagates in the x -direction with

$$k_x = -j\gamma_x = \beta_x - j\alpha_x \quad (5.2)$$

and if k_y is real and less than k , the wavenumber in the transverse x -direction is of the form

$$k_z = \beta_z + j\alpha_z \quad (5.3)$$

with $\beta_z > 0$ and $\alpha_z > 0$ [25]. As $z > 0$ in the radiation region, the variation of the leaky wave in the z -direction is given by

$$f(z) = e^{(\alpha_z - j\beta_z)z} \quad (5.4)$$

From 5.4 it is concluded that the wave propagates in the z -direction with increasing amplitude, becoming infinite at infinity.

In Figure 5.2 the radiating leaky surface starts at $x = 0$ and extends to infinity in the positive x -direction. The excited fast wave radiates into the space $z > 0$ as indicated in Figure 5.4 at the approximate angle

$$\theta_0 \approx \sin^{-1} \frac{\lambda}{\lambda_g} = \sin^{-1} \frac{\beta}{k} \quad (5.5)$$

where $\lambda = 2\pi/\beta_x$ is the guide wavelength of the leaky wave in the x -direction. As the wave is attenuated as it travels along the leaky guide, the amount of radiation per unit length decreases. This is indicated by the relative density of the radiation lines. At any point x' , the field intensity increases in the positive z -direction up to a point $z = x'/\tan \theta_0$ as given by the z -variation of (5.4). Beyond that the field intensity should decrease rapidly, as no radiation reaches that region if the source is located at $x = 0$. The radiation is essentially confined to the region $z < x'/\tan \theta_0$.

5.2.2 Leaky Waves vs. Surface Waves

Although leaky waves are frequently assigned to the same class as surface waves also encountered in flush-mounted antennas, there are distinct differences in both propagation characteristics and effect they have on antenna performance. These opposed properties are summarized in Table 5.1.

Table 5.1: Summarizing the differences between Leaky Waves and Surface Waves.

Leaky Waves	Surface Waves
Not a proper mode of the open waveguide region as it contains a singularity at infinity. Depending on the source location, it does have a finite, valid field representation within a restricted area.	A proper mode which is a valid field representation with finite intensity.
Phase velocity greater than the speed of light (fast wave).	Phase velocity less than that of light (slow wave).
Complex wavenumber in the direction of propagation, as the wave is attenuated by the continuous leakage of energy.	Real propagation wavenumber in the longitudinal direction.
Complex transverse wavenumber: the wave propagates away from the structure with increasing amplitude within a restricted region.	Imaginary wavenumber in the transverse direction: the wave decays rapidly away from the guiding structure.
Radiation occurs due to a continuous leakage of energy along the guiding structure.	The wave is completely bound to the guiding structure and does not radiate.

5.2.3 Radiation Characteristics

Whenever a weakly attenuated leaky wave is dominant on a guiding surface, the total radiation pattern will be determined primarily by the radiation from the leaky wave. The leaky-wave fields on the guiding surface act as an equivalent source distribution to determine the leaky-wave pattern. In general, multiple leaky waves can exist on the guiding structure, depending on the guiding structure itself as well as the method of excitation. The total radiated pattern is then obtained by the superposition of the individual patterns, and a knowledge of the individual wave amplitudes is thus required [24].

In [24], formulas are also derived for the fields radiated from an arbitrary planar surface which supports a cylindrical leaky wave that propagates radially outward. This is done for $n = 1$ leaky-waves for both TE_z and TM_z cases by first calculating the equivalent planar current distribution and from that, the radiated fields. Results indicate that the E_ϕ contribution of the TM_z mode is a constant while the E_θ component exhibits a sharp peak at the maximum of the radiated conical beam making it the dominant component. The reverse applies for the TE_z mode. This suggests that for good circular polarization the TE and TM modes should have similar propagation constants to ensure equal E_θ and E_ϕ components with the correct phasing.

In practical leaky wave antennas, secondary contributions to the radiated fields exist due to the finiteness of the guiding structure and the source which excites the fast wave [28]. These include radiation from rapidly attenuated higher order leaky modes that are not dominant, direct radiation from the feed source, and diffraction from the edges of the guiding structure due to the leaky waves as well as bounded surface waves which may exist on the structure. Previous studies have attempted to reduce or eliminate edge diffraction by placing absorbing material around the perimeter of the antenna.

As mentioned in Section 5.2, a leaky wave radiates into space at a specific angle determined by β . If the phase velocity of the wave is much faster than that of light, the radiated beam has a maximum close to broadside. As the phase velocity decreases and approaches that of light, the radiation maximum moves closer to end-fire and becomes completely bound (slow wave) when the phase velocity is smaller than that of light. For a leaky parallel plate waveguide mode, this corresponds to a lower angle of radiation for a greater separation between the ground plane and PRS as the phase velocity for the waveguide mode becomes

smaller. This can be seen from equation 5.6

$$\beta = \sqrt{k^2 - k_c^2} = \sqrt{k^2 - (n\pi/d)^2} \quad (5.6)$$

where k is the free space wavenumber, k_c is the cutoff wavenumber of the guide, n the order of the mode, and d the separation between the plates.

In [26] it is shown that for a leaky-parallel plate waveguide structure of which the PRS consists of metal patches (see Figure 5.1), it is impossible to create a single conical beam beyond some critical angle if the permittivity of the dielectric substrate is too small. This is because one encounters secondary beams due to radiation from higher order leaky parallel plate waveguide modes. As is the case with normal array theory, the patch periodicity needs to be smaller than $\lambda/2$ in order to avoid grating lobes for all scan angles.

5.3 Determination of the Complex Propagation Constant

To enable the detailed design of leaky-wave antennas with specific attributes, it is necessary to be able to calculate the complex propagation of the leaky wave structure accurately. This is beyond the scope of this study, and is recommended for further investigation. A summary of some of the techniques used to determine this propagation constant is presented.

5.3.1 Transverse Resonance Procedure

From (5.6) it is seen that if k_c is known, the propagation constant of the guide can be determined. The cutoff wavenumber can be found by solving the wave equation within the guide, subject to the appropriate boundary conditions. This becomes complicated for complex waveguides, and generally yields much more information than necessary if only the propagation constant of the guide is required. The transverse resonance procedure is based on the fact that at cutoff the fields form standing waves in the transverse plane of the guide. This can be modeled with an equivalent transmission line circuit operating at resonance for which

$$Z_{in}^+(z) + Z_{in}^-(z) = 0 \quad (5.7)$$

for all values of z , where $Z_{in}^+(z)$ and $Z_{in}^-(z)$ are the input impedances seen looking to either side of point z on the resonant line. An example of a leaky wave antenna

and its transverse equivalent network is shown in Figure 5.3. The PRS is represented by a constant shunt susceptance B_s , while Y_0 and Y_s are the characteristic admittances of the open region and the region within the guide respectively [29]. More detail on this procedure can be found in [30, 31, 29].

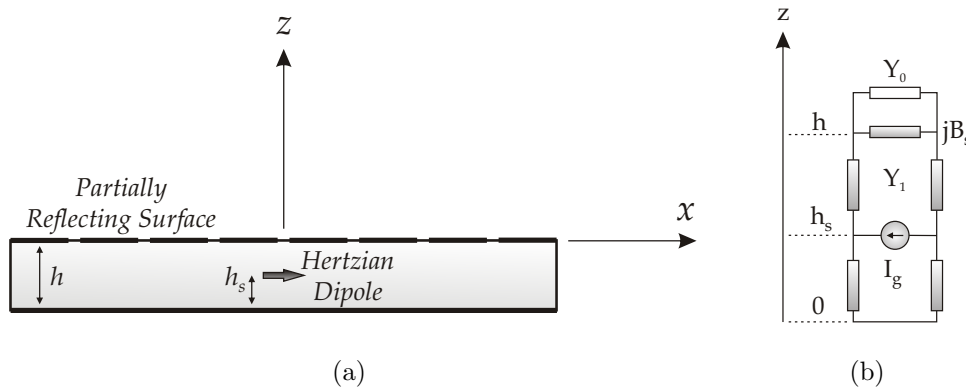


Figure 5.3: (a) Leaky wave antenna consisting of a PRS mounted on a grounded dielectric slab with a hertzian dipole excitation. (b) Transverse equivalent network representation of the structure [29].

5.3.2 FDTD

In literature, the determination of the complex propagation constants of leaky-wave structures by the finite-difference time-domain method has been pursued in different ways. Simulations have been done with a relatively large number of unit cells terminated in an absorbing material, with the number of unit cells chosen large enough so as to guarantee the convergence of the computed value.

Methods have also been demonstrated which enables the concurrent extraction of dispersion diagrams and attenuation constants via the simulation of a single unit cell terminated in periodic boundary conditions [32]. This is invariably done by fixing the phase difference at the boundaries of the unit cell to a real number, and determining the resonant frequencies of the resulting fields sampled within the cell. The dispersive properties of the structure can then be illustrated by graphs plotting the phase velocity or relative phase difference vs. frequency, in effect calculating the phase constant β of the complex propagation constant of the leaky-wave guide. In [33] this method was applied to the dispersion analysis of a negative refractive index medium of [34]. The resulting dispersion diagram included regions of both slow and fast wave operation, and inspection of the associated field resonances indicated important differences. When a phase difference

corresponding to slow wave propagation is enforced at the unit cell boundaries, the electric field inside the structure exhibits a non decaying wave form. However, moving to the fast wave region on the dispersion diagram, the pulse-excited field has a decaying response. In the absence of any ohmic or dielectric losses inside the unit cell this attenuation is interpreted as radiation which is successfully accounted for by the FDTD method even though no explicit attenuation constant is included in the periodic boundary conditions. Other techniques to calculate the attenuation constant are discussed in [32].

5.4 Single QHA Element Exciting a Leaky-Wave Structure

To validate the simulations done on the leaky-wave structures excited by quadrifilar helices, a prototype consisting of a single $\lambda/4$ QHA underneath a PRS was manufactured and measured. This section discusses the physical construction considerations and the design simulations leading to the final choice of parameter values. Different patch elements are compared for the use in the partially reflective surface. The measured results of the constructed leaky-wave antenna compares well to that of the simulated antenna model.

5.4.1 Physical Construction

A 3D CAD model of the constructed LWA is shown in Figure 5.4. The partially reflected surface is created by printing a 91 element patch array with a hexagonal arrangement on a dielectric substrate. For this purpose the thinnest available substrate (0.2 mm FR4) is chosen so that it will have a very small effect on the radiated fields. The patch array is supported on top of a circular ground plane by a layer of polystyrene foam which has approximately the same permittivity as air. Due to availability, the thickness of the foam layer is 48.5 mm . A single $\lambda/4$ QHA located in the center of the ground plane acts as the source which excites the circularly polarized leaky wave. As discussed in Section 3.3.2, the helical elements are constructed from Huber & Suhner *EZ* – 86 semi-rigid coaxial cable with the feed point shifted to a point of lower current to adjust the input impedance. The outer conductors of the helices are soldered to the ground plane at the junction, and extended through the back and terminated in SMA connectors to enable the connections of the measurement setup outlined in Section 5.4.3.

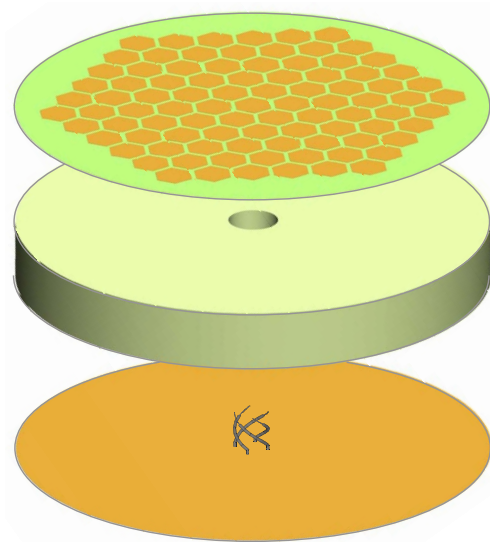


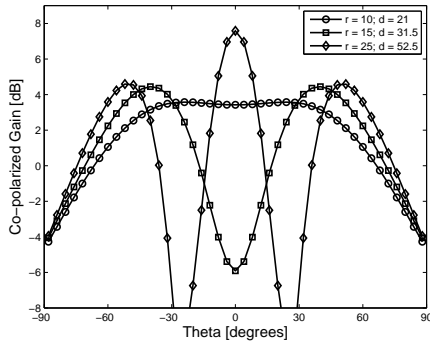
Figure 5.4: CAD construction model of the leaky-wave antenna.

5.4.2 Design Simulations

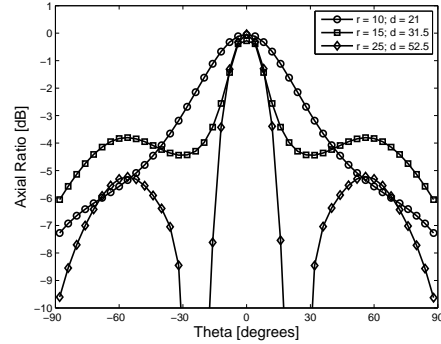
The geometry considered for the LWS structure is a 91 element patch array with the elements arranged hexagonally. The height of this partially reflective surface is fixed at 48.5 mm (see Section 5.4.1). Preliminary simulation indicated that making the ground plane circular as opposed to hexagonal, and extending it by about 20 mm from the edges of the patch array, produces the most uniform pattern in the azimuth plane.

A choice has to be made between circular and hexagonal patch elements, as well as the diameter and spacing of the elements. As the leaky-wave guiding structure and not the source has the largest influence on the radiation pattern, the parameters of the $\lambda/4$ QHA which excites the leaky wave is kept constant, and only the feed point is adjusted to produce the desired input impedance. A Matlab script file is employed to sweep both the element radius (r) and spacing (d) used when constructing the FEKO simulation model. The results of each ensuing run of the FEKO solver are saved and plotted for convenient comparison. Figures 5.5 and 5.6 show some of the far-field results used in the selection of the final parameter values.

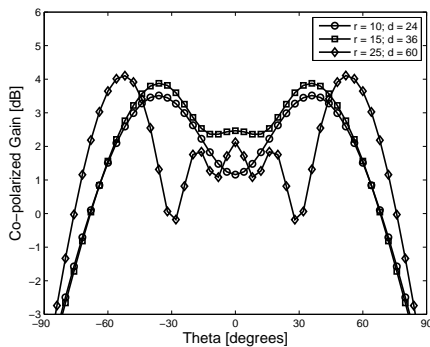
To minimize the computational resources necessary, these initial simulation models do not include the dielectric substrate on which the patches are printed. The same trends in radiation properties are observed for both circular and hexagonal patches. For small patch radii only a single beam at broadside is radiated. As the radius increases, this becomes a typical conical beam with a minimum at broadside. With radii that is larger still, an additional beam at broadside



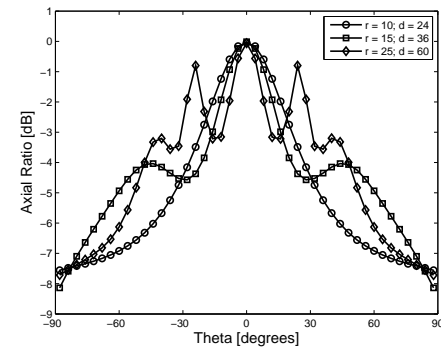
(a) RHC gain component ($d = 2.1r$)



(b) Axial Ratio ($d = 2.1r$)



(c) RHC gain component ($d = 2.4r$)



(d) Axial Ratio ($d = 2.4r$)

Figure 5.5: Selected simulation results with circular patch elements used. Parameters dimensions given are in mm , and $\phi = 0$.

emerges and the axial ratio starts to degrade. Closer element spacing generally results in improved axial ratio with a more pronounced minimum in the null at broadside. A slightly better axial ratio is also achieved with hexagonal elements which makes it the element of choice. Further simulations with refined modeling, carried out over a much narrower range of parameter values, established the final values of the dimensional parameters for the LWA that is constructed. These final values are summarized in Table 5.2 and the simulation results are compared to the measured results in Section 5.4.3.

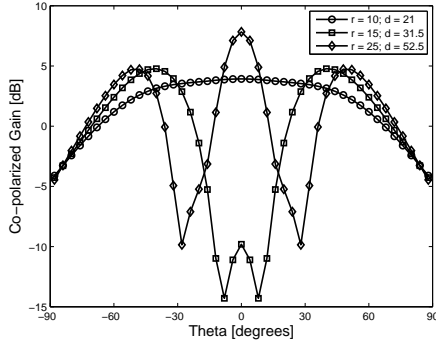
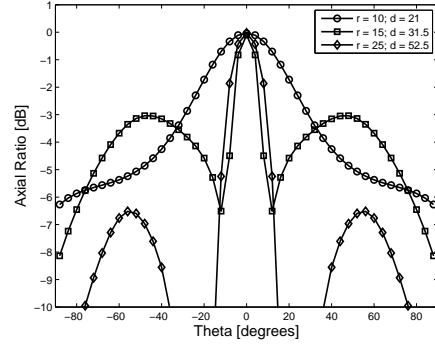
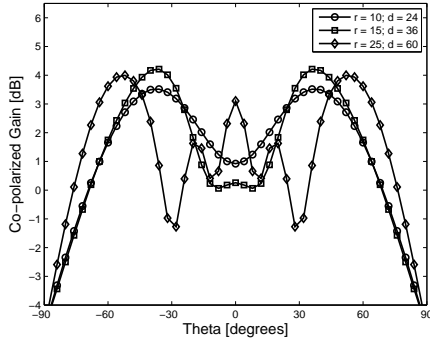
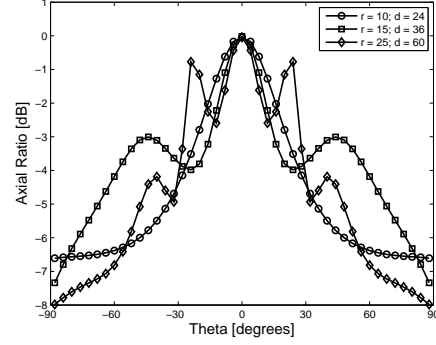
(a) RHC gain component ($d = 2.1r$)(b) Axial Ratio ($d = 2.1r$)(c) RHC gain component ($d = 2.4r$)(d) Axial Ratio ($d = 2.4r$)

Figure 5.6: Selected simulation results with hexagonal patch elements used. Parameters dimensions given are in mm , and $\phi = 0$.

Table 5.2: Chosen values of the parameters for the construction of the LWA prototype.

Parameter	Description	Value
Leaky Wave Guiding Structure		
h	Partially reflective surface height	$48.5 \text{ mm} = 0.259\lambda$
r_{gp}	Circular ground plane radius	$191.5 \text{ mm} = 1.021\lambda$
r_{hex}	Radius of circle inscribed in a hexagonal patch	$14 \text{ mm} = 0.075\lambda$
s	Spacing between patch centers	$31.5 \text{ mm} = 0.168\lambda$
N	Number of patches	91
QHA source element		
l	Axial length	$30 \text{ mm} = 0.160\lambda$
n	Number of turns	0.45
r_v	Volute radius	$13 \text{ mm} = 0.069\lambda$
fp	Feed position (fraction of helical element)	0.75
d_o	Outer conductor diameter	2.2 mm
d_i	Inner conductor diameter	0.51 mm

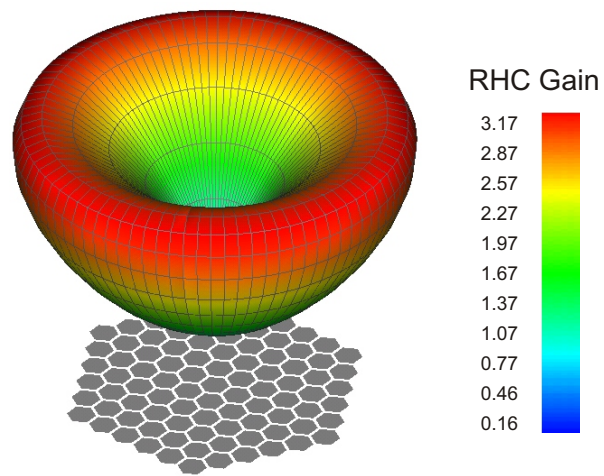


Figure 5.7: Co-polarized gain component of the final simulation model illustrating the characteristic conical radiation pattern from a two-dimensional leaky-wave antenna.

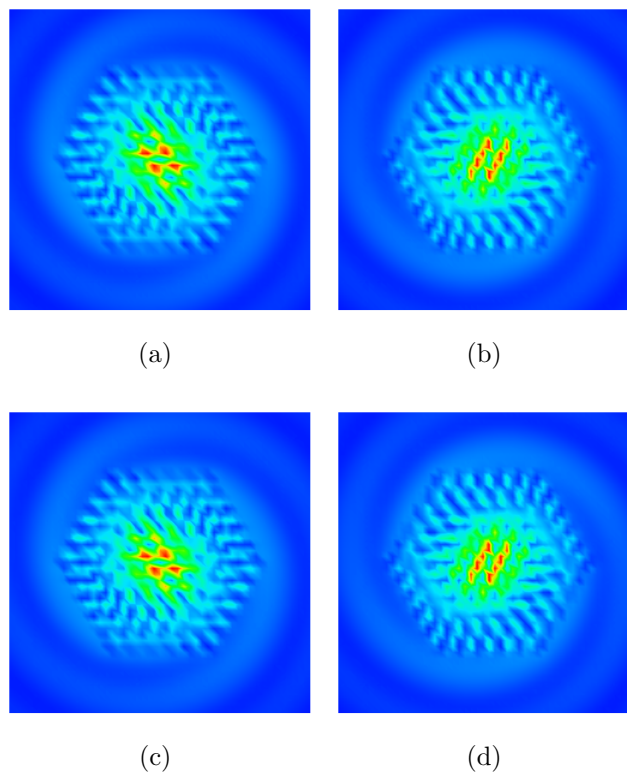


Figure 5.8: Simulated instantaneous E-field just above the patches at (a) 0° , (b) 90° , (c) 180° and (d) 270° . Linear Scale $[0 \text{ V/m} \dots 50 \text{ V/m}]$.

5.4.3 Measured Results

The four input ports of the QHA that are extended through the ground plane, need to be fed with equal amplitude and quadrature phasing. To eliminate any influence on the radiation performance by feed signal deficiencies caused by an imperfect feed network, measurements are taken with each helical element fed separately and the others passively terminated in matched loads. Post-processing is then done on the measured data to add the contributions of each helical element with the correct amplitude and phasing, and so calculate the radiation pattern with an ideal feed network in place.

If power loss due to polarization mismatch is ignored, the Friis transmission equation relating the received and transmitted power between two antennas can be written as

$$\frac{P_r}{P_t} = |S_{21}|^2 = \left(\frac{\lambda}{4\pi R} \right)^2 G_t G_r (1 - |\Gamma_t|^2) (1 - |\Gamma_r|^2) \quad (5.8)$$

In 5.8, G_t and G_r are the gain of the transmitting and receiving antennas respectively, R is the separation between the antennas, and λ is the wavelength. Γ_t and Γ_r are the reflection coefficients at the inputs of the receive and transmit antennas. To meet the far-field criteria, $R > 2D^2/\lambda$ is required, where D is the largest dimension of either antenna [15]. With $R = 5\text{ m}$ used in the measurements, this is met comfortably as the largest dimension of the LWA prototype is $D = 0.383\text{ m}$ for which the minimum separation is $R_{min} = 2D^2/\lambda = 1.56\text{ m}$.

Measurements are made by connecting the transmitting antenna to port 1, and the receiving antenna to port 2 of a network analyzer. As the measured S_{21} is a voltage parameter, it is related to received and transmitted power ratio by

$$|S_{21}|^2 = \frac{P_r}{P_t} \quad (5.9)$$

Since four individual transmission coefficient measurement are made with each helix fed, the amplitude should be adjusted so that when the measured transmission coefficients are added together it will be the same as when all four helices are connected simultaneously. For equal power division between the four ports $P_{tc} = 4P_{ti}$, where the subscripts tc and ti denotes the transmitted power for the combined and individually fed cases. The transmitted power for individually fed elements should therefore be reduced by a factor of 4. From 5.9, this corresponds to reducing each measured S_{21} by $\sqrt{4}$. Also, as the individual helices have different input impedances, the power loss due to impedance mismatch should be

compensated for in each term when the contribution of each helix is added. The calculated gain will thus be the true gain of the antenna without the loss associated with impedance mismatch. Including the necessary quadrature phasing, the combined transmission coefficient can be written as

$$S_{21(Combined)} = \frac{1}{\sqrt{4}} \left(\frac{S_{21(port1)}}{R_1} + \frac{jS_{21(port2)}}{R_2} - \frac{S_{21(port3)}}{R_3} - \frac{jS_{21(port4)}}{R_4} \right) \quad (5.10)$$

The term R_n in 5.10 is the reflected power loss term for each measurement, and is given by

$$R_n = (1 - |\Gamma_{Test\ Antenna}|^2) (1 - |\Gamma_{AUT\ Port\ n}|^2) \quad (5.11)$$

These combined results are used in the three-antenna method, in which three measurements are made using all combinations of the three antennas. With the two test antennas indicated as A and B , three equations can be written based on (5.8) but with the impedance mismatch terms already included:

$$G_A G_B = |S_{21(AB)}|^2 \left(\frac{4\pi R}{\lambda} \right)^2 \quad (5.12)$$

$$G_A G_{AUT} = |S_{21(A\ AUT)}|^2 \left(\frac{4\pi R}{\lambda} \right)^2 \quad (5.13)$$

$$G_B G_{AUT} = |S_{21(B\ AUT)}|^2 \left(\frac{4\pi R}{\lambda} \right)^2 \quad (5.14)$$

From these equations the gain of the antenna under test can be solved as

$$G_{AUT} = \sqrt{\frac{|S_{21(A\ AUT)}|^2 |S_{21(B\ AUT)}|^2}{|S_{21(AB)}|^2 \left(\frac{4\pi R}{\lambda} \right)^2}} \quad (5.15)$$

Figure 5.9 shows the results of the mathematically combined far-field gain and axial ratio. In both cases the simulations and measurements are in good agreement. A slight asymmetry is noticed in the elevation plane measured data which can largely be attributed to the tolerances associated with constructing the antenna by hand. The semi-rigid helical elements with protruding center conductors are particularly difficult to shape accurately with identical resonant lengths and adjusted feed points. In the FEKO simulation model, the substrate on which the patches are printed is modeled as a thin dielectric layer which is infinite in extent. This is done to make the simulation computationally efficient and still sufficiently accurate. It is also the most likely explanation for the improvement of the measured axial ratio over the simulated axial ratio.

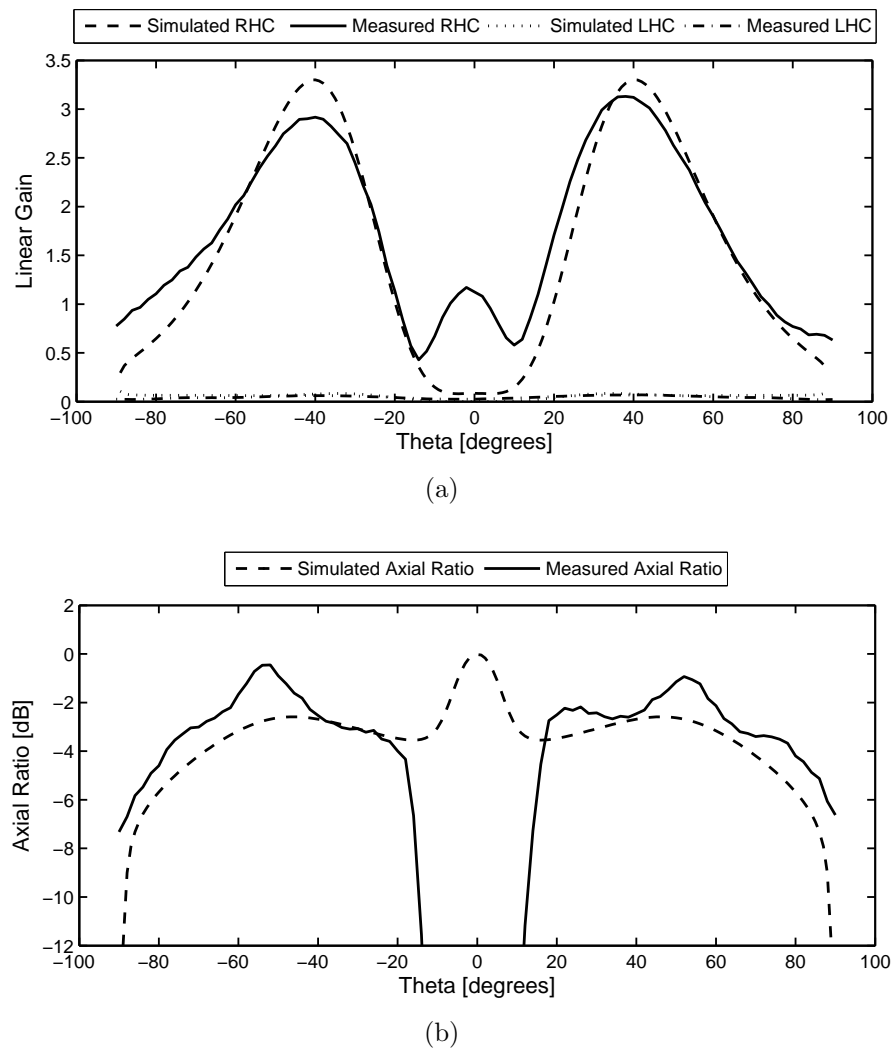
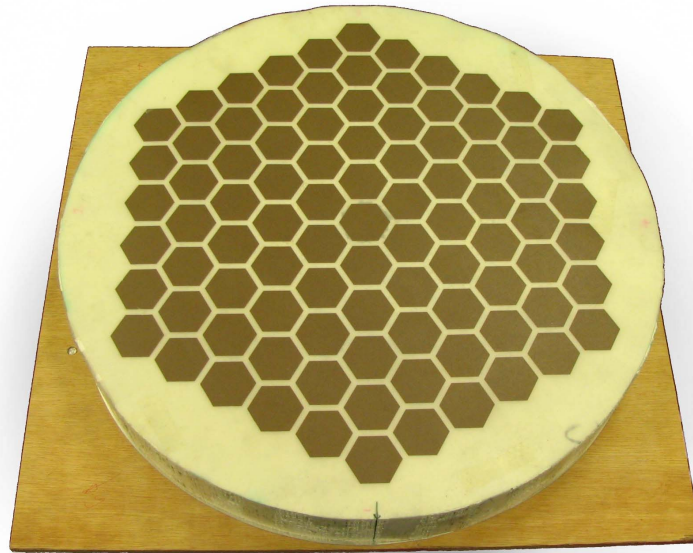
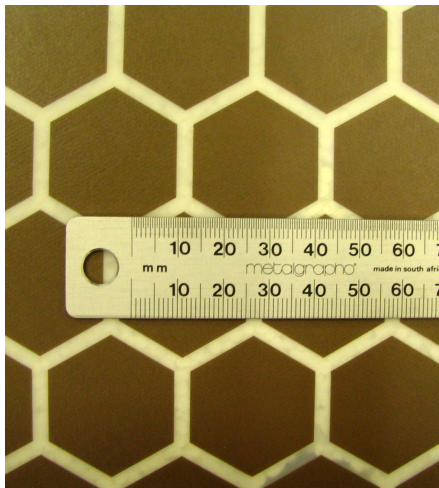


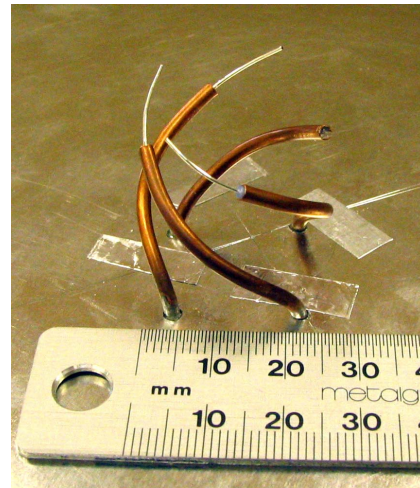
Figure 5.9: Simulated and measured (a) gain and (b) axial ratio in the elevation plane with $\phi = 0^\circ$.



(a)



(b)



(c)

Figure 5.10: (a) Assembled LWA. (b) Hexagonal patch PRS. (c) $\lambda/4$ QHA excitation element.

Chapter 6

Further Analysis of Steered Leaky Wave Arrays

6.1 Introduction

The CAP software of Appendix B was used to analyze a number of array structures with a range of varying parameter values. This was done to find a structure with superior radiation performance when scanned to low elevation angles. Hexagonal arrays consisting of 91 and 61 circular or hexagonal top-disked $\lambda/4$ QHA elements were considered. The dimensional parameters which were investigated include the size of the top disk, the spacing between neighboring disks, and the height of the partially reflective surface (patches) above the QHA elements.

A 91 element hexagonal patch LWS was selected of which the parameter values is given in Section 6.2. The results of the steering of the main beam of this array to various angles are presented. In Section 6.4, a finite ground plane is introduced to the structure and beam steering performance is compared to that of the array with an infinite ground plane.

6.2 Dimensional Parameters

Table 6.1 summarizes the parameter values of the array selected to have the best radiation performance. The results presented in this chapter pertain to array with these dimensions. Some trends were noticed in the simulation of arrays with different dimensions. As the patches move further away from the ground plane, smaller patch sizes are needed for optimum performance. Narrower gaps between patches also seem to produce the best results. This is perhaps the reason that the hexagonal patches performed better than the circular patches.

Table 6.1: Physical parameters array with preferred performance

Parameter	Description	Value
Leaky Wave Guiding Structure		
h	Partially reflective surface height	$23 \text{ mm} = 0.123\lambda$
r_{hex}	Radius of circle inscribed in a hexagonal patch	$30 \text{ mm} = 0.160\lambda$
s	Spacing between patch centers	$62 \text{ mm} = 0.331\lambda$
d_s	Spacing between adjacent patch edges	$2 \text{ mm} = 0.011\lambda$
N	Number of patches	91
QHA source elements		
l	Axial length	$18 \text{ mm} = 0.096\lambda$
n	Number of turns	0.5
r_v	Volute radius	$12 \text{ mm} = 0.064\lambda$
f_p	Feed position (fraction of helical element)	0.55
d_o	Outer conductor diameter	2.2 mm
d_i	Inner conductor diameter	0.51 mm

6.3 Beam Steering

Figure 6.1 shows the simulated RHC and LHC polarized gain components of the array with an infinite ground plane, of which the main beam is scanned to different angles. This illustrates the good axial ratio that is achieved over most of the hemisphere.

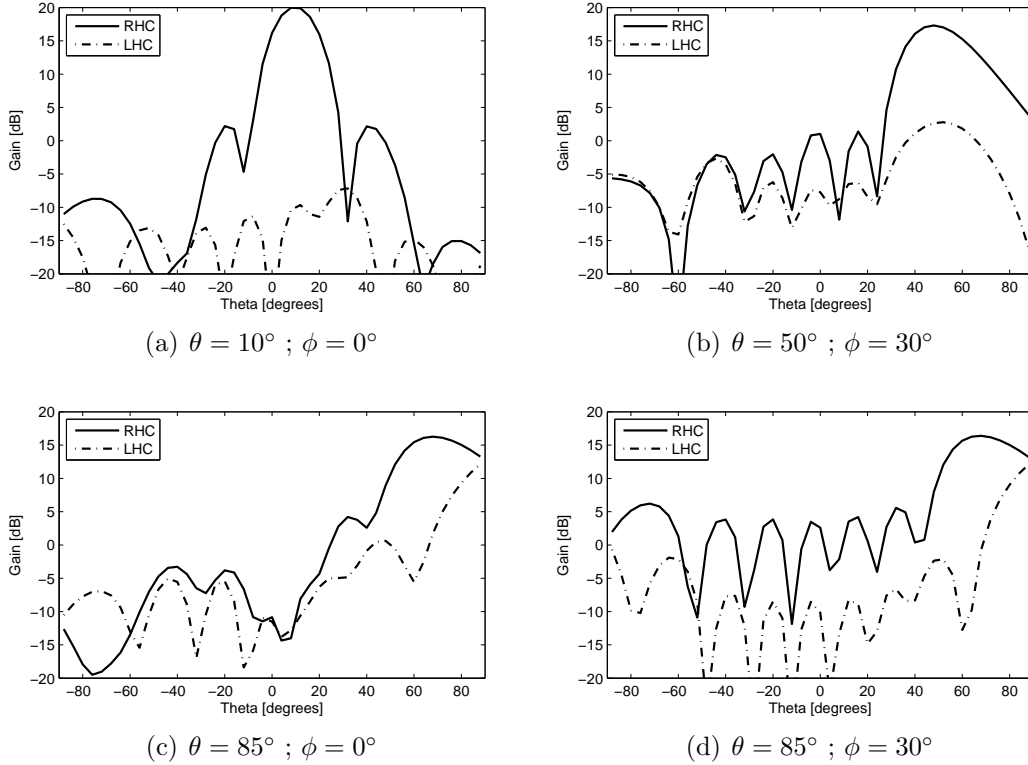


Figure 6.1: Co- and cross-polarized gain components of the steered beam with an infinite ground plane. The values for which the phasing was calculated are indicated.

6.4 Finite Ground Plane

To enable the automatic generation of array models with a finite ground plane using the CAP software of Appendix B, a unit element is created. This element includes the same $\lambda/4$ QHA element and hexagonal patch of which the dimensions are given in Table 6.1. An additional metallic hexagonal plate is attached to the bottom ends of the helices. The size of this hexagon corresponds to the interelement spacing of the array and enables these elements to be fitted together to form a homogeneous ground plane beneath the QHA elements. This unit element is illustrated in Figure 6.3a.

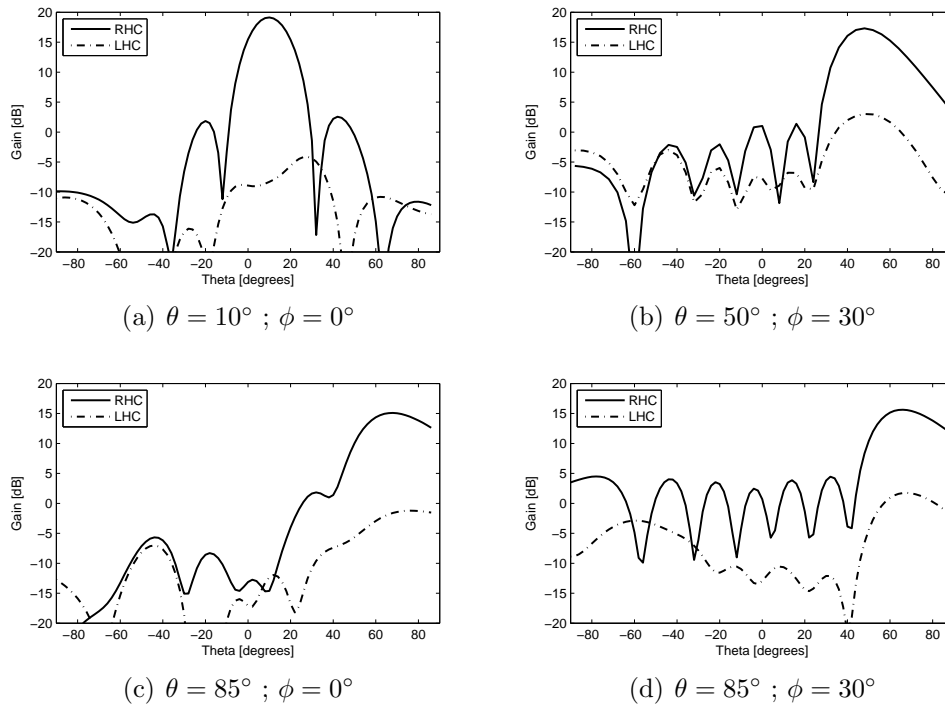


Figure 6.2: Co- and cross-polarized gain components of the steered beam with a finite ground plane. The values for which the phasing was calculated are indicated.

Far-field results of simulations in which the main beam is steered to the same angles as in the previous section is presented in Figure 6.2. The radiation patterns are similar to that of the infinite counterpart, with even better axial ratio at low elevation angles nearly down to the horizon.

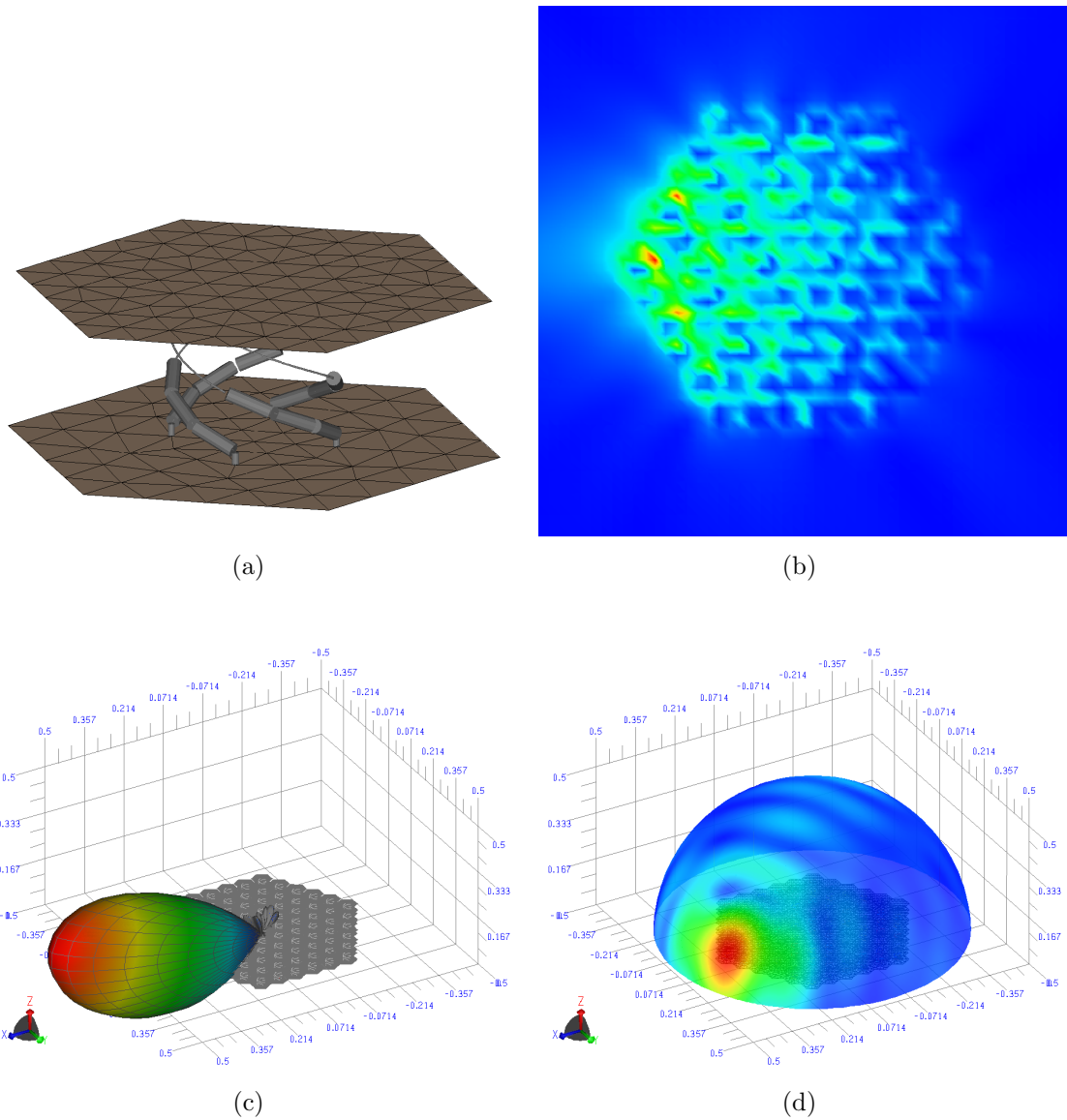


Figure 6.3: (a) Unit element for the creation of the finite ground plane array. (b) Electric field magnitude just above the PRS with the array scanned to $\theta = 85^\circ$. (c) Hemispherical plane E-field magnitude with the array scanned to $\theta = 85^\circ$. (d) RHCP gain component with the beam scanned to $\theta = 85^\circ$.

6.5 Summary

The automated array software is used to optimize the parameters of a hexagonal leaky-wave array antenna for good radiation performance at low elevation angles. The presented results shows that good circular polarization can be achieved close to the horizon even with an infinite ground plane present. With the introduction of a finite ground plane to the structure, the ability to steer a circularly polarized beam close to the horizon is further enhanced.

Chapter 7

Conclusions and Recommended Future Work

7.1 Conclusions

The growing demand of mobile satellite communications necessitates the development and improvement of radiating elements which can cover an entire hemisphere with good circularly polarized radiation. These can include stand-alone antennas for handheld or other applications where the tracking of individual satellites is not required. The aeronautical Inmarsat network is an example of an application that demands an array antenna with a circularly polarized beam that can be steered over most of the upper hemisphere with sufficient gain. Contributing to the difficulty of meeting these specifications, is the requirement that the antenna be light weight, and have a low profile.

An in depth study of the quadrifilar helix antenna has proved its viability as an isolated element for applications requiring the above mentioned wide-beam, circularly polarized radiation pattern with a compact configuration. The resonant quadrature-fed QHA offers superior radiation performance, but requires the design and inclusion of a feed network to provide signals with the correct amplitude and phasing to the individual helices. These individual resonant helices are inherently narrowband, but a considerable impedance bandwidth improvement is possible when fed with a power-dividing feed network. The self-phased QHA consists of two bifilar loops with different resonant lengths fed in parallel, forcing the current to divide with the quadrature phasing necessary. This simplifies the feeding of the antenna to a great extent, but acceptable radiation performance is only achieved over a very narrow frequency band. For most of the QHA varieties, results indicate tall and narrow elements radiate wider beams with better circu-

lar polarization at low elevation angles. This diminishes the prospect of using QHA element in wide angle scanning arrays where a low profile is essential. An exponentially tapered QHA is introduced as an antenna with a reduced height and relatively wide angle radiation.

Following the experimental design of an array consisting of cavity-backed crossed slot elements to which a parasitic patch was added, a similar top disk structure was incorporated in both the $\lambda/2$ and $\lambda/4$ QHA elements. This had the effect of making the isolated element pattern more directive. The size of the disk became the dominating factor in determining the radiation pattern and it was possible to design low profile elements with good axial ratio at low elevation angles. A microstrip feed network was designed for a constructed $\lambda/2$ QHA prototype. Good agreement between measured and simulated results was achieved.

The main initiative behind the inclusion of the top disk, was to investigate the effect that the increased level of coupling will have on the ability to scan to low elevation angles. This was most pronounced for the $\lambda/4$ QHA of which the top patch is not connected to helical elements, but floating parasitically above them. A sustained level of coupling at increased element separation was noticed - particularly within rectangular and hexagonal arrangements of tightly packed elements. With only a single element fed, the active single element pattern is drawn towards neighboring elements giving these antennas a much wider radiation pattern when operation within an array environment.

This altered radiation characteristics and sustained coupling level is attributed to a leaky-wave mode supported by the array structure. Having a phase velocity greater than that of light, the leaky fast wave radiates into the space above the partially reflected surface at an angle determined by β . The properties and characteristics of leaky-wave antennas are studied and presented. A leaky-wave antenna consisting of a single $\lambda/4$ QHA element beneath a hexagonal patch PRS was constructed and measurements compared well with simulated results. The open ended $\lambda/4$ QHA was constructed from semi-rigid coaxial cable, providing an effective technique to adjust the feed point to obtain the desired input impedance.

Further investigations were done into the radiation performance of large hexagonal arrays of $\lambda/4$ QHA elements with both circular and hexagonal parasitic patch leaky wave structures. The automated array simulating software was used to find an array with superior radiation performance, especially at low elevation angles. With the inclusion of a finite ground plane, it is shown to be possible to steer a beam with excellent circular polarization very close to the horizon. This array

also has the added advantage of being very low profile.

7.2 Future Work

The richness of the electromagnetic phenomena associated with leaky-wave antennas and its application to wide angle scanning arrays, provides many areas of research into which further study is required. In order to successfully synthesize antennas for exact specifications one needs to fully understand the principle of operation and the factors influencing performance. As a continuation of this thesis, the following topics need to be investigated further.

- The characterization of the different modes simultaneously supported by the structure, and their respective contribution to the radiated field should be investigated.
- The ability to accurately determine the complex propagation constant of the radiating leaky wave is of paramount importance when the design of specific attributes is required. The methods briefly mentioned here can be implemented and used to characterize the modes.
- The input impedance variations of the antenna elements when operating within a scanned array needs to be investigated. Methods to compensate for the degrading effects of mutual coupling can be implemented. This is of particular importance where tight coupling between elements is utilized for improved radiation performance.
- Amplitude tapers across the radiating aperture of the leaky wave array can be implemented for beam shaping and side lobe control. This can possibly be implemented by excitation control or non-uniform leakage at various locations.
- Although the hexagonal arrays have associated active single element patterns which is relatively uniform in the azimuth plane, it is noticed that the co-polarized pattern is more directive towards certain angles. Further study can aim at making the propagation and leakage of the supported modes more uniform.
- The possibility of using fewer excitation elements underneath the same partially reflective surface to achieve the similar radiation performance can be examined.

- Different edge terminations for the leaky-wave structures can be considered, including the possibility passively terminating the edge elements.

Bibliography

- [1] W. George, P. Steyn, and V. Basso, “Development of Phased Array Antennas for INMARSAT Aeronautical Applications,” *South African IEEE AP/MMT Conference*, March 2005. (Cited on pages 1, 2, 25, 29, 45, and 72.)
- [2] *FEKO User Manual Suite 5.2*, EM Software & Systems (Pty) Ltd, August 2006. (Cited on pages 2 and B–3.)
- [3] C. Kilgus, “Multielement, fractional turn helices,” *IEEE Transactions on Antennas and Propagation*, vol. 16, pp. 499–500, July 1968. (Cited on page 3.)
- [4] —, “Spacecraft and ground station applications of the resonant quadrifilar helix,” *Digest of the 1974 International IEEE Antennas and Propagation Symposium*, pp. 75–77, June 1974. (Cited on page 3.)
- [5] —, “The Resonant Quadrifilar Helix,” *IEEE Transactions on Antennas and Propagation*, pp. 349–351, May 1969. (Cited on page 5.)
- [6] M. Amin and R. Cahill, “Bandwidth limitations of two-port fed and self-phased quadrifilar helix antennas,” *Microwave and Optical Technical Letters*, vol. 46, pp. 11–15, July 2005. (Cited on page 5.)
- [7] C. Kilgus, “Resonant Quadrifilar Helix Design,” *The Microwave Journal*, pp. 49–54, December 1970. (Cited on page 6.)
- [8] —, “Shaped-conical radiation pattern performance of the backfire quadrifilar helix,” *IEEE Transactions on Antennas and Propagation*, pp. 392–397, May 1975. (Cited on pages 18 and 19.)
- [9] Y. Chen and K. Wong, “Low-profile Broadband Printed Quadrifilar Helical Antenna for Broadcasting Satellite Application,” *Microwave and Optical Technology Letters*, vol. 36, no. 2, pp. 134–136, January 2003. (Cited on page 20.)

- [10] B. Desplanches and J. Louvigne, "Analysis of the mutual coupling in finite arrays of printed quadrifilar helical antennas," *Microwave and Optical Technology Letters*, vol. 28, no. 1, pp. 34–40, January 2001. (Cited on page 20.)
- [11] J. Louvigne and A. Sharaiha, "Broadband tapered printed quadrifilar helical antenna," *Electronic Letters*, vol. 37, no. 15, pp. 932–933, July 2001. (Cited on page 20.)
- [12] Y. Letestu and A. Sharaiha, "Ku-Band Printed Quadrifilar Helical Antenna with Integrated Feed Network," *Microwave and Optical Technology Letters*, vol. 40, no. 3, pp. 219–221, February 2004. (Cited on page 21.)
- [13] D. Pozar, *Microwave Engineering*, 3rd ed. John Wiley & Sons, 2005. (Cited on page 38.)
- [14] Rogers Corporation, "RO4000 Series High Frequency Circuit Materials," *Datasheet*, 2005. (Cited on page 39.)
- [15] C. Balanis, *Antenna Theory, Analysis and Design*, 2nd ed. John Wiley & Sons, 1997. (Cited on pages 47, 48, 72, and 85.)
- [16] D. Pozar, "The Active Element Pattern," *IEEE Transactions on Antennas and Propagation*, vol. 42, no. 8, pp. 1176–1178, August 1994. (Cited on pages 51 and 52.)
- [17] P. Kildal, *Foundations of Antennas*. Studentlitteratur, 2000. (Cited on pages xii and 51.)
- [18] D. Pozar, "A Relation Between the Active Input Impedance and the Active Element Pattern of a Phased Array," *IEEE Transactions on Antennas and Propagation*, vol. 51, no. 9, pp. 2486–2489, September 2003. (Cited on page 53.)
- [19] A. Derneryd, "Compensation of Mutual Coupling Effects in Array Antennas," *IEEE Antennas and Propagation Society Symposium Digest*, pp. 1122–1125, 1996. (Cited on page 53.)
- [20] H. Steyskal and J. Herd, "Mutual Coupling Compensation in Small Array Antennas," *IEEE Transactions on Antennas and Propagation*, vol. 38, no. 12, pp. 1971–1975, December 1990. (Cited on page 53.)

- [21] R. Speciale, “Advanced Design of Phased Array Beam-Forming Networks,” *IEEE Antennas and Propagation Magazine*, vol. 38, no. 4, pp. 22–34, August 1996. (Cited on page 53.)
- [22] D. Kelley, “Array Antenna Pattern Modeling Methods that include Mutual Coupling Effects,” *IEEE Transactions on Antennas and Propagation*, vol. 41, no. 12, pp. 1625–1632, December 1993. (Cited on page 53.)
- [23] T. Su and H. Ling, “A Model for the Active Element Pattern of Array Elements Including both Mutual Coupling and Platform Effects,” 2000. (Cited on page 53.)
- [24] D. Jackson and A. Ip, “Radiation from Cylindrical Leaky-Waves,” *IEEE Transactions on Antennas and Propagation*, vol. 38, no. 4, pp. 482–488, April 1990. (Cited on pages 73 and 77.)
- [25] L. Goldstone and A. Oliner, “Leaky-Wave Antennas I: Rectangular Waveguides,” *IRE Transactions on Antennas and Propagation*, pp. 307–319, October 1959. (Cited on pages xiii, 73, 74, and 75.)
- [26] T. Zhao, D. Jackson, J. Williams, H. Yang, and A. Oliner, “2-D Periodic Leaky-Wave Antennas – Part I: Metal Patch Design,” *IEEE Transactions on Antennas and Propagation*, vol. 53, no. 11, pp. 3505–3514, November 2005. (Cited on pages 73, 74, and 78.)
- [27] T. Zhao, D. Jackson, and J. Williams, “2-D Periodic Leaky-Wave Antennas – Part II: Slot Design,” *IEEE Transaction on Antennas and Propagation*, vol. 53, no. 11, pp. 3515–3524, November 2005. (Cited on pages 73 and 74.)
- [28] D. Jackson, A. Ip, and A. Oliner, “An improved calculation procedure for the radiation pattern of Cylindrical Leaky-Wave Antennas of finite size,” *IEEE Transactions on Antennas and Propagation*, vol. 40, no. 1, pp. 19–24, January 1992. (Cited on pages 74 and 77.)
- [29] R. Collin, “Analytical solution for Leaky-Wave Antenna,” *IRE Transactions on Antennas and Propagation*, pp. 561–565, September 1962. (Cited on pages xiii and 79.)
- [30] G. Lovat, P. Burghignoli, and D. Jacksons, “Fundamental properties and optimization of broadside radiation from uniform Leaky Wave Antennas,” *IEEE Transactions on Antennas and Propagation*, vol. 54, no. 5, pp. 1442–1452, May 2006. (Cited on page 79.)

- [31] J. Sureau, "Propagation Constant of Leaky-Wave Antenna for Near End-Fire Radiation," *IEEE Transaction on Antennas and Propagation*, 1967. (Cited on page 79.)
- [32] T. Kokkinos, C. Sarris, and G. Eleftheriades, "Periodic FDTD Analysis of Leaky-Wave Structures And Applications to the Analysis of Negative-Refractive-Index Leaky-Wave Antennas," *IEEE Transactions on Microwave Theory and Techniques*, vol. 54, no. 4, pp. 1619–1630, April 2006. (Cited on pages 79 and 80.)
- [33] T. Kokkinos, C. D. Sarris, and G. V. Eleftheriades, "Periodic finite-difference time-domain analysis of loaded transmission-line negativerefractive-index metamaterials," *IEEE Transactions of Microwave Theory and Techniques*, vol. 53, no. 4, pp. 1488–1495, April 2005. (Cited on page 79.)
- [34] G. V. Eleftheriades, A. K. Iyer, and P. C. Kremer, "Planar negative refractive index media using periodically loaded transmission lines," *IEEE Transactions on Microwave Theory and Techniques*, vol. 50, no. 12, pp. 2702–2712, December 2002. (Cited on page 79.)

Appendix A

Parameter Study Automating Software

In order to facilitate the parametrical study of the antennas, in particular the various single element QHAs of Chapter 2, Matlab software was developed which enables the automated sweeping of simulation parameters and the convenient visualization of results. This is useful not only in parametrical studies, but also when optimizing a design where iterative parameter adjustments become cumbersome.

A.1 The GUI

Figure A.1 shows a screen shot of the graphical user interface which is used to specify the parameter ranges and interactively visualize results. The rest of the section provides an overview of the options available to the user.

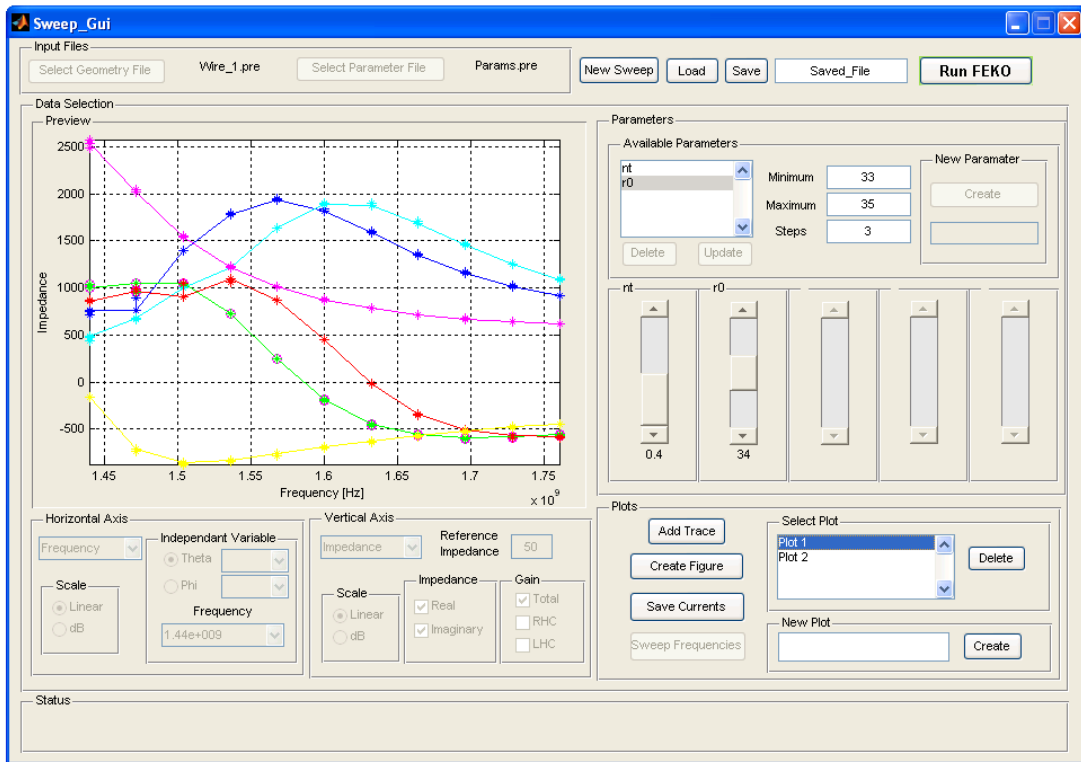
A.1.1 Simulation Setup

Model Selection

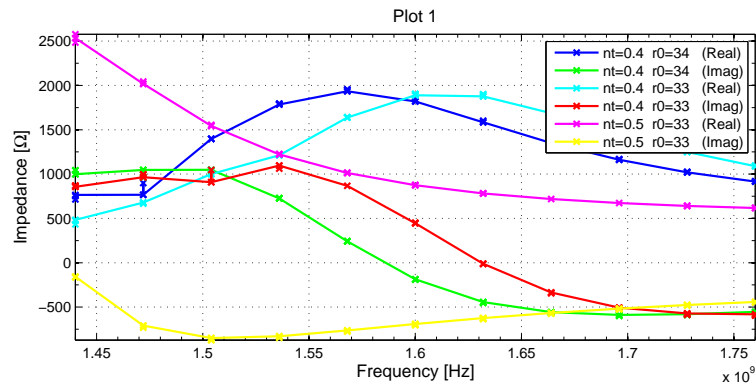
Any FEKO pre-file which defines the model geometry can be selected. The parameter file to which the modified parameters will be written needs to be imported into this file.

Parameter Definition

Up to a maximum of five different parameters can be analyzed simultaneously. Care must be taken that the specific parameters to be adjusted are not included in the geometry pre-file and only imported from the parameter file. A parameter



(a)



(b)

Figure A.1: (a) Screenshot of the graphical user interface. (b) Example of an automatically created plot of the results of a parametrical study.

is defined by specifying its minimum and maximum values as well as the number of steps in between. Once a parameter is created it can be updated or removed from the list of necessary.

A.1.2 Data Management

For each combination of parameter values, the parameters and their values are written to the parameter file and a FEKO run is executed. The resulting output

file is read by a Matlab script file and the required results stored as variables within a dynamic data-structure which is augmented after every run. This data structure can become quite large for many parameter values and large amounts of requested simulation data. The number of runs that needs to be completed also become time-consuming, especially for large models. This is not a problem for the parametrical study of the wire quadrifilar helices as the models are simple with only a small number of wire segments. When visualizing the results, this data-structure is used to create the plots of the requested parameters.

A.1.3 Result Visualization

A visualization window in the graphical user interface shows an updated view of data for currently selected parameter values. This is updated interactively as the user adjusts the slider positions to alter the combination of parameter values. New plots are created, and traces are added to the plot to compare the effect of parametrical changes.

When the user is content with the data presented in the visualization window, the current view can be saved to a separate Matlab figure.

Appendix B

Array Simulation Project Software

The large models associated with the simulation of array structures requires considerable computational resources and lengthy simulation times. Setting up different simulation models for small geometrical and excitation variation is redundant, and it is often desired to keep the results of simulations as well as detail of the model used before changes are made.

To facilitate the study of the arrays, a Matlab program (CAP - Comprehensive Array Program) was developed which uses FEKO to simulate array structures and stores results for convenient subsequent examination and analysis. A graphical user interface (GUI) allows the user to input geometrical parameters which define the array configuration for which a FEKO model will be created automatically. Simulation parameters to be used when running the FEKO solver are also specified.

The main motivation for the development of the software was to enable a set of simulation projects to be defined simultaneously and then run the FEKO solver to process the entire list of projects at a convenient time. Section B.1 explains how the GUI allows the user to create the project list and specify geometrical, simulation and data management parameters. Details of the different project options as well as data storage and control flow are discussed briefly.

B.1 The Graphical User Interface

Figure B.1 shows a screenshot of the CAP graphical user interface which allows the user to interactively set up a list of projects. This section provides some detail of the procedure to define a project and elaborates briefly on the different

options available.

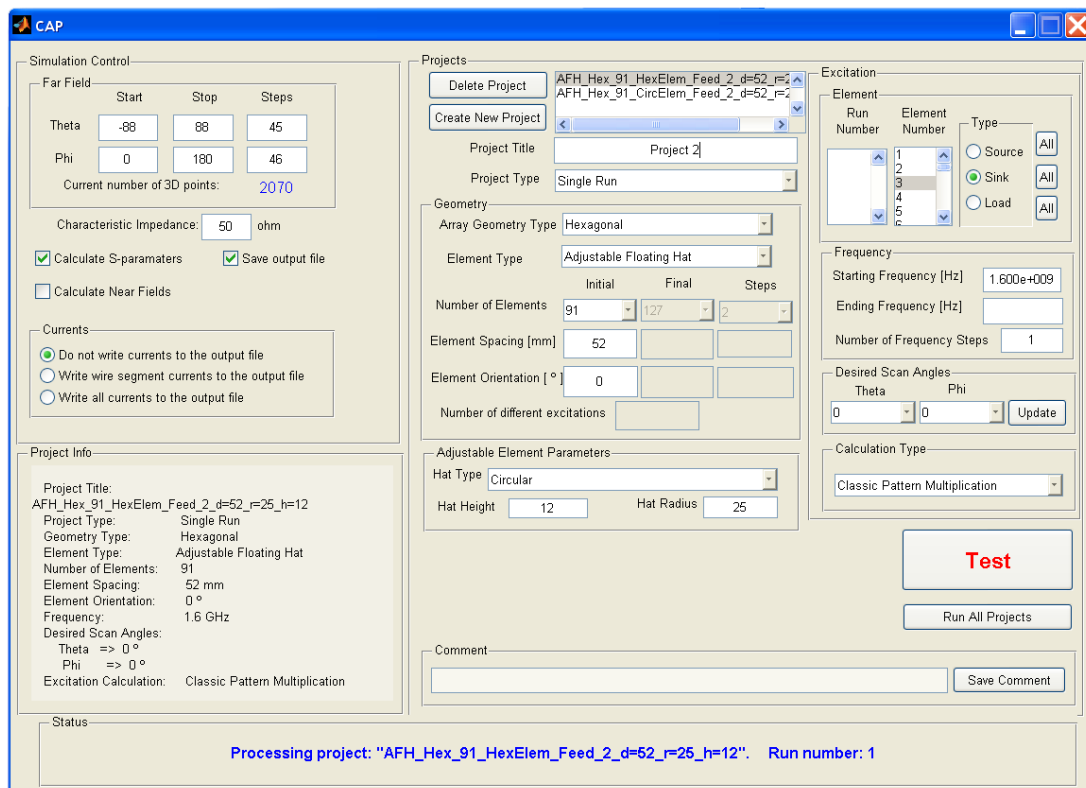


Figure B.1: Screenshot of the CAP user interface.

B.1.1 Project Options

A project can consist of one or more simulations, depending on whether some geometrical parameter is to be swept or whether different excitations need to be applied to the same structure. Available project types include the following:

Single Run A single simulation with a unique model and excitation.

Number of Elements A set of simulations with increasing number of elements within the same array arrangement. The number of elements and simulations are selected from drop-down menus to ensure a valid number of elements corresponding to the currently selected array arrangement is used.

Element Spacing Identical elements with increasing element spacing within the same array configuration.

Element Orientation Variation in the azimuthal rotation of each array element about its own axis.

Excitation For a particular array geometry, different sets of excitation can be specified (e.g. for steering the array to different angles). This project type utilizes the option in FEKO to save the LU-decomposition of the system of linear equations during the first run, and then read the saved file during subsequent runs. A considerable reduction in computation time is achieved.

For the project types in which a geometrical parameter is swept, the starting and ending values as well as the number of steps is selected from a drop-down menu, or specified manually. The different excitation options are discussed in Section B.1.3.

B.1.2 Geometry

Both the array arrangement and elements used within the array are selected. The different array topologies are discussed in Section 4.3. The following elements can be selected:

Half-wavelength QHA $\lambda/2$ QHA with helical wires connected to a shorting disk at the top (Section 3.2).

Quarter wavelength QHA $\lambda/4$ QHA with open-ended helices and a parasitic disk positioned above them (Section 3.3).

Adjustable Floating Top QHA Open-ended $\lambda/4$ QHA of which the height and diameter of the parasitic patch can be specified. Circular or hexagonal disks can be selected. An option to select no disk is also available to enable the use of traditional QHAs.

Hertzian Dipoles The FEKO *A5* source card is used to specify an electric Hertzian dipole as excitation [2]. The exact location and orientation of the dipoles are set manually in the PreFEKO files.

B.1.3 Excitation

Individual array elements can be specified to be either excited in a normal fashion by a source with the calculated excitation coefficient, used as a sink (source with zero applied signal) for S-parameter calculations or terminated resistively. This enables the array response to be simulated with only certain elements fed, as is the case when studying active single element patterns. For projects with more than one run, the state of individual elements within each run can be selected.

The list of frequencies is also created by specifying the starting and ending frequencies, and the number of frequency steps.

B.1.4 Far-field Solutions and Beam Steering

After the geometrical parameters for the creation of the array have been assigned, the far-field parameters can be updated. For each project run, the desired θ_0 and ϕ_0 angles to which the beam needs to be steered, can be selected. The method by which the excitation coefficients are then calculated can also be specified. The classic array multiplication method is currently employed, but provision is made to include other methods - like those discussed in Section 4.2.3 which compensates for mutual coupling effects. Using the defined array geometry and the scan angles, the excitation coefficients are then calculated and included in the setup of the FEKO simulation model.

The number and position of points in space at which the far-field is to be calculated are designated by entering the start, stop and number of steps values in both the elevation and azimuth planes.

B.1.5 Output Files and Data Storage

In the Simulation Control panel, different simulation and data storage options must be selected. These include the characteristic source and resistive termination impedances, whether or not the S-parameters or near-fields are calculated, and whether or not the FEKO text output file is stored. In the case where this file is stored, the currents (if any) which should be written to the output file must also be specified. As the array models can become very large with a huge number of metallic triangles and wire segments, the size of the resulting output file needs to be considered when saving the calculated currents.

B.1.6 Other Options and Information

When a previously created project is selected from the project list, some of the most important project information is shown in the Project Info text panel. This serves to remind the user of the existing project parameters, as well as to verify that the project has been set up correctly. A descriptive comment can be saved for each project, and will be used as a heading in the project's information file (Section B.2).

B.2 Data Management and Control Flow

The list of projects is defined with all the parameters and settings mentioned above specified. A data structure is created which contains the information necessary to successfully set up and run all the projects. When the user is confident that the project information is correct, the processing of the simulation is started. For every list of projects, a folder is created with the current time and date as folder name. This folder contains all the project directories, which in turn contains sequentially numbered folders for all the project runs. Within these folders, all the FEKO simulation model and result files as well as additional files created are stored. These additional files include an information text file detailing the parameter selections specified by the user. The output text file resulting from the FEKO run is processed by a Matlab script file and the data is stored as variables within a Mat-file for convenient visualization and comparison at a later stage. If the calculation of S-parameters was requested, an **.snp* Touchstone file is also exported from FEKO and stored. For a large number of ports, the format of this Touchstone file needs to be manipulated to ensure compatibility with Matlab, Microwave Office and other software tools. Mat-files containing the mathematically combined antenna and feed network coupling coefficients, element coordinates and theoretical radiation pattern are also included.

The list of projects is processed sequentially and the status of the current project and simulation run indicated in the information text box. Control is returned to Matlab after all the projects have been successfully executed and the data saved.

Appendix C

Hexagonal Array Coordinates

For the N element hexagonal array of Figure 4.9, the cylindrical coordinates (ρ, θ) of each element is given below. ρ and θ are measured from the origin and anti-clockwise from the x -axis respectively. d is the spacing between adjacent elements in mm , and the values of θ are given in degrees. The formulation is grouped into levels consisting of concentric hexagonal rings of elements (see Figure 4.9).

Level 0 :

$$\left. \begin{array}{l} \rho_m = 0 \\ \theta_m = 0 \end{array} \right\} m = 1$$

Level 1 :

$$\left. \begin{array}{l} \rho_m = d \\ \theta_m = 60(m-2) \end{array} \right\} m = 2, 3, 4, 5, 6, 7$$

Level 2 :

$$\left. \begin{array}{l} \rho_m = 2d \\ \theta_m = 60\left(\frac{m-8}{2}\right) \end{array} \right\} m = 8, 10, 12, 14, 16, 18$$
$$\left. \begin{array}{l} \rho_m = 2d \cos 30 \\ \theta_m = 60\left(\frac{m-9}{2}\right) + 30 \end{array} \right\} m = 9, 11, 13, 15, 17, 19$$

Level 3 :

$$\begin{aligned}
& \left. \begin{aligned} \rho_m &= 3d \\ \theta_m &= 60 \left(\frac{m-20}{3} \right) \end{aligned} \right\} m &= 20, 23, 26, 29, 32, 35 \\
& \left. \begin{aligned} \rho_m &= \sqrt{7}d \\ \theta_m &= 60 \left(\frac{m-21}{3} \right) + \left(30 - \arctan \left(\frac{1}{3\sqrt{3}} \right) \right) \end{aligned} \right\} m &= 21, 24, 27, 30, 33, 36 \\
& \left. \begin{aligned} \rho_m &= \sqrt{7}d \\ \theta_m &= 60 \left(\left(\frac{m-22}{3} \right) + 1 \right) - \left(30 - \arctan \left(\frac{1}{3\sqrt{3}} \right) \right) \end{aligned} \right\} m &= 22, 25, 28, 31, 34, 37
\end{aligned}$$

Level 4 :

$$\begin{aligned}
& \left. \begin{aligned} \rho_m &= 4d \\ \theta_m &= 60 \left(\frac{m-38}{4} \right) \end{aligned} \right\} m &= 38, 42, 46, 50, 54, 58 \\
& \left. \begin{aligned} \rho_m &= \sqrt{(d \cos 30)^2 + (3.5d)^2} \\ \theta_m &= 60 \left(\frac{m-39}{4} \right) + \arcsin \frac{d \cos 30}{\rho_m} \end{aligned} \right\} m &= 39, 42, 47, 51, 55, 59 \\
& \left. \begin{aligned} \rho_m &= \sqrt{(2d \cos 30)^2 + (3d)^2} \\ \theta_m &= 60 \left(\frac{m-40}{4} \right) + \arcsin \frac{2d \cos 30}{\rho_m} \end{aligned} \right\} m &= 40, 43, 48, 52, 56, 60 \\
& \left. \begin{aligned} \rho_m &= \sqrt{(d \cos 30)^2 + (3.5d)^2} \\ \theta_m &= 60 \left(\left(\frac{m-41}{4} \right) + 1 \right) - \arcsin \frac{d \cos 30}{\rho_m} \end{aligned} \right\} m &= 41, 44, 49, 53, 57, 61
\end{aligned}$$

Level 5 :

$$\begin{aligned}
& \left. \begin{aligned} \rho_m &= 5d \\ \theta_m &= 60 \left(\frac{m-62}{5} \right) \end{aligned} \right\} m &= 62, 67, 72, 77, 82, 88 \\
& \left. \begin{aligned} \rho_m &= \sqrt{(d \cos 30)^2 + (4.5d)^2} \\ \theta_m &= 60 \left(\frac{m-63}{5} \right) + \arcsin \frac{d \cos 30}{\rho_m} \end{aligned} \right\} m &= 63, 68, 73, 78, 83, 88 \\
& \left. \begin{aligned} \rho_m &= \sqrt{(2d \cos 30)^2 + (4d)^2} \\ \theta_m &= 60 \left(\frac{m-64}{5} \right) + \arcsin \frac{2d \cos 30}{\rho_m} \end{aligned} \right\} m &= 64, 69, 74, 79, 84, 89 \\
& \left. \begin{aligned} \rho_m &= \sqrt{(2d \cos 30)^2 + (4d)^2} \\ \theta_m &= 60 \left(\left(\frac{m-65}{5} \right) + 1 \right) + \arcsin \frac{2d \cos 30}{\rho_m} \end{aligned} \right\} m &= 65, 70, 75, 80, 85, 90
\end{aligned}$$

$$\left. \begin{aligned} \rho_m &= \sqrt{(d \cos 30)^2 + (4.5d)^2} \\ \theta_m &= 60 \left(\left(\frac{m-66}{5} \right) + 1 \right) + \arcsin \frac{d \cos 30}{\rho_m} \end{aligned} \right\} m = 66, 71, 76, 81, 86, 91$$

From these cylindrical coordinates, the rectangular coordinates can be determined as

$$x_m = \rho_m \cos \theta_m$$

$$y_m = \rho_m \sin \theta_m$$